Final Report

FDOT Contract No.: BDV31-977-122
UF Contract No.: AWD07133

In-service Assessment of Road Sinkholes with 2D Ambient Noise Tomography

Principal Investigator:
Khiem Tran, Ph.D.

Researchers:
Yao Wang
Mohammad Khorrami
Ruoyu Chen

Department of Civil and Coastal Engineering
Engineering School of Sustainable Infrastructure and Environment
University of Florida
P.O. Box 116580
Gainesville, Florida 32611-6580

Developed for the

David Horhota, Ph.D., P.E., Project Manager

November 2021

DISCLAIMER

The opinions, findings, and conclusions expressed in this publication are those of the authors and not necessarily those of the Florida Department of Transportation or the U.S. Department of Transportation.

Prepared in cooperation with the State of Florida Department of Transportation and the U.S. Department of Transportation.

SI (MODERN METRIC) CONVERSION FACTORS (from FHWA)

APPROXIMATE CONVERSIONS TO SI UNITS

SYMBOL	WHEN YOU KNOW	MULTIPLY BY	TO FIND	SYMBOL
LENGTH				
in	inches	25.4	millimeters	mm
ft	feet	0.305	meters	m
yd	yards	0.914	meters	m
mi	miles	1.61	kilometers	km

SYMBOL	WHEN YOU KNOW	MULTIPLY BY	TO FIND	SYMBOL
AREA				
in^2	square inches	645.2	square millimeters	mm^2
ft^2	square feet	0.093	square meters	m^2
yd^2	square yard	0.836	square meters	m^2
ac	acres	0.405	hectares	ha
mi^2	square miles	2.59	square kilometers	km^2

SYMBOL	WHEN YOU KNOW	MULTIPLY BY	TO FIND	SYMBOL
VOLUME				
fl oz	fluid ounces	29.57	milliliters	mL
gal	gallons	3.785	liters	L
ft^3	cubic feet	0.028	cubic meters	m^3
yd^3	cubic yards	0.765	cubic meters	m^3
NOTE: volumes greater than 1000 L shall be shown in m^3				

SYMBOL	WHEN YOU KNOW	MULTIPLY BY	TO FIND	SYMBOL
MASS				
oz	ounces	28.35	grams	g
lb	pounds	0.454	kilograms	kg
T	short tons (2000 lb)	0.907	megagrams (or "metric ton")	Mg (or "t")

SYMBOL	WHEN YOU KNOW	MULTIPLY BY	TO FIND	SYMBOL
TEMPERATURE (exact degrees)				
°F	Fahrenheit	5 (F-32)/9 or (F-32)/1.8	Celsius	°C

SYMBOL	WHEN YOU KNOW	MULTIPLY BY	TO FIND	SYMBOL
ILLUMINATION				
fc	foot-candles	10.76	lux	lx
fl	foot-Lamberts	3.426	candela/m^2	cd/m^2

SYMBOL	WHEN YOU KNOW	MULTIPLY BY	TO FIND	SYMBOL
FORCE and PRESSURE or STRESS				
Lbf*	poundforce	4.45	newtons	N
kip	kip force	1000	pounds	lbf
lbf/in^2	poundforce per square inch	6.89	kilopascals	kPa

APPROXIMATE CONVERSIONS TO SI UNITS

SYMBOL	WHEN YOU KNOW	MULTIPLY BY	TO FIND	SYMBOL
		LENGTH		
mm	millimeters	0.039	inches	in
m	meters	3.28	feet	ft
m	meters	1.09	yards	yd
km	kilometers	0.621	miles	mi

SYMBOL	WHEN YOU KNOW	MULTIPLY BY	TO FIND	SYMBOL
		AREA		
mm^2	square millimeters	0.0016	square inches	in^2
m^2	square meters	10.764	square feet	ft^2
m^2	square meters	1.195	square yards	yd^2
ha	hectares	2.47	acres	ac
km^2	square kilometers	0.386	square miles	mi^2

SYMBOL	WHEN YOU KNOW	MULTIPLY BY	TO FIND	SYMBOL
		VOLUME		
mL	milliliters	0.034	fluid ounces	fl oz
L	liters	0.264	gallons	gal
m^3	cubic meters	35.314	cubic feet	ft^3
m^3	cubic meters	1.307	cubic yards	yd^3

SYMBOL	WHEN YOU KNOW	MULTIPLY BY	TO FIND	SYMBOL
		MASS		
g	grams	0.035	ounces	oz
kg	kilograms	2.202	pounds	lb
Mg (or "t")	megagrams (or "metric ton")	1.103	short tons (2000 lb)	T

SYMBOL	WHEN YOU KNOW	MULTIPLY BY	TO FIND	SYMBOL
		TEMPERATURE (exact degrees)		
°C	Celsius	1.8C+32	Fahrenheit	°F

SYMBOL	WHEN YOU KNOW	MULTIPLY BY	TO FIND	SYMBOL
		ILLUMINATION		
lx	lux	0.0929	foot-candles	fc
cd/m^2	candela/m^2	0.2919	foot-Lamberts	fl

SYMBOL	WHEN YOU KNOW	MULTIPLY BY	TO FIND	SYMBOL
		FORCE and PRESSURE or STRESS		
N	newtons	0.225	poundforce	lbf
kPa	kilopascals	0.145	poundforce per square inch	lbf/in^2

*SI is the symbol for International System of Units. Appropriate rounding should be made to comply with Section 4 of ASTM E380. (Revised March 2003)

TECHNICAL REPORT DOCUMENTATION PAGE

1. Report No.	2. Government Accession No.	3. Recipient's Catalog No.
4. Title and Subtitle In-service Assessment of Road Sinkholes with 2D Ambient Noise Tomography		5. Report Date November 2021 6. Performing Organization Code
7. Authors Yao Wang, Khiem Tran, Mohammad Khorrami, and Ruoyu Chen		8. Performing Organization Report No.
9. Performing Organization Name and Address University of Florida – Dept. of Civil and Coastal Engineering Engineering School of Sustainable Infrastructure and Environment 365 Weil Hall – P.O. Box 116580 Gainesville, FL 32611-6580		10. Work Unit No. (TRAIS) 11. Contract or Grant No. BDV31-977-122
12. Sponsoring Agency Name and Address Florida Department of Transportation 605 Suwannee Street, MS 30 Tallahassee, FL 32399		13. Type of Report and Period Covered Final Report 9/1/2019 – 11/30/2021 14. Sponsoring Agency Code
15. Supplementary Notes		

16. Abstract

Seismic methods are often used for detection of pre-collapsed sinkholes (voids) under roadway for remediation to minimize the risk to the safety of the traveling public. While the active-source seismic methods can provide accurate subsurface profiles, they require closing the traffic flow for hours during testing and potentially cause sinkhole collapse due to ground perturbation by source excitation. To address these issues, this project developed a novel 2D ambient noise tomography (2D ANT) method for imaging voids under roadway. Instead of using the approximated Green's function, whose required assumption of energy balance at both sides of each receiver pair is rarely satisfied, the cross-correlation function of traffic noise recordings is inverted directly to obtain velocity structures. To adopt the concepts of seismic interferometry and derive the model structural kernel, passing-by vehicles are assumed as moving sources along the receiver array. The source power-spectrum density is determined via the reverse-time imaging approach to approximate the source distribution. The 2D ANT method was first demonstrated on realistic synthetic models with the accurate recovery of the model variable layers and buried voids. To demonstrate its effectiveness with the real-world problems, we successfully applied the method to field data at four test sites in Florida. The field experimental results show that the method is capable of resolving subsurface S-wave velocity (Vs) structures and detecting voids and anomalies at various sizes and depths. With typically available traffic noises (5-20 Hz) induced by passing vehicles, the method can characterize subsurface profiles at good resolutions (3-ft pixel to 60-ft depth and 5-ft pixel to 150-ft depth). The inverted Vs profiles generally agree with the invasive tests (SPT and CPT), including identification of voids, anomalies and depth of limestone layers. Based on the field results of noise recordings with the minimum disruption of the traffic flow, the developed ANT method is an effective approach for characterization of roadway substructure and detection of road sinkholes. A standalone GUI software of the 2D ANT analysis has also been developed and transferred to FDOT for future uses.

17. Key Words	18. Distribution Statement
Full Waveform Inversion, Ambient Noise Tomography, Road Sinkholes, Geophysical Testing, Graphical User Interface	No restrictions.

19. Security Classif. (of this report)	20. Security Classif. (of this page)	21. No. of Pages	22. Price
Unclassified	Unclassified	146	

Form DOT F 1700.7 (8-72) Reproduction of completed page authorized

ACKNOWLEDGMENTS

The researchers would like to thank the Florida Department of Transportation (FDOT) for the financial support to carry out this research, the State Materials Office in Gainesville and District 4 & 5 Geotechnical Materials Groups for providing access and assisting with many of the field tests, as well as the Universal Engineering for conducting SPT and borehole sonar at the Miami site.

EXECUTIVE SUMMARY

Road sinkholes pose significant risk to the health and safety of the traveling public. Successful detection of the pre-collapsed sinkholes (buried voids) is crucial to minimize the risk. Noninvasive geophysical methods are often used for sinkhole detection because they can investigate subsurface conditions over a larger volume of materials at lower costs than invasive tests. Electromagnetic wave-based approaches, such as electrical resistivity and ground penetrating radar, are often used for imaging of buried voids. However, identifying deep voids (> 20-30 ft deep) with these methods is difficult due to strong signal attenuation with depth. Thus, seismic methods are more favorable for detection of the deep voids, because of their good penetration with depth. For example, our 2D/3D full waveform inversion (FWI) methods (developed through FDOT-funded projects) using active wave-fields can be used to identify a buried void to a depth of three void diameters up to 60-ft depth. However, as they require multiple source impacts to generate the active wave-fields, the data acquisition time is considerable. This leads to negative impacts caused by closing the traffic flow during seismic testing. In addition, it is risky to collect active seismic wave-fields on top of large voids, as ground perturbation by an active source may trigger collapses while persons are in the test area. This project aimed to eliminate the requirement of closing traffic during data acquisition and reduce the field-testing risk and effort.

This research project developed a novel 2D ambient noise tomography (2D ANT) method, which can extract 2D seismic velocities of substructures at feet-scales to at least 100-ft depth from traffic noises for detection of road sinkholes. More specifically, traffic noises were acquired using land-streamer geophones located along lane dividers and/or road shoulders, and then cross-correlated to obtain the measured correlation functions (similar to Green's functions) between any

pair of geophones. Elastic wave equations were used to obtain simulated correlation functions to be matched with the measured ones for extraction of 2D S-wave velocity structures. Individual 2D velocity slices along the lane dividers and shoulders can be combined for a 3D subsurface image of the test road segment.

There are several advantages of the developed 2D ANT method. First, no wave excitation is needed, thus minimizing the risk of collapse due to ground perturbation as well as reducing testing efforts. Second, land-streamer geophones can be deployed quickly in a few minutes, and data are acquired without closing traffic. Third, traffic noises are rich in low frequency components at 5 to 10 Hz (from heavy trucks), which are important to resolve deep structures to 100-ft depth. They also consist of higher frequency components at 10 to 25 Hz (from cars at various speeds) needed for a high resolution characterized at feet-scales. Lastly, all wave propagation modes (body and surface waves) contained in measured correlation functions are used to extract detailed information of buried voids.

The 2D ANT method was tested at four test sites: US-441 highway (pre- and post-grouting), Miami highway bridge, Wekiva Parkway SR-46, and Wekiva Parkway Bridge No. 110110. For each site, traffic noises were recorded continuously for 5 to 20 minutes by a linear array of geophones at 120- to 300-ft spread length. The field experimental results show that the ANT method is capable of resolving the subsurface S-wave velocity (Vs) structure at good resolutions (3-ft pixel to 60-ft depth and at 5-ft pixel to 150-ft depth) and detecting voids and anomalies at various sizes and depths. The inverted Vs profiles from the 2D ANT generally agree with the ground truth from invasive tests (SPT and CPT), including identification of voids and depth of limestone layers. A standalone GUI software of the 2D ANT analysis has also been

developed and transferred to FDOT for future uses such as characterization of roadway substructure, as well as detection of buried voids, anomalies and others.

TABLE OF CONTENTS

Page

Table of Contents

LIST OF FIGURES

Figure page

LIST OF TABLES

"None"

Chapter 1 – INTRODUCTION

1.1 Background

Road sinkholes are mostly caused by natural voids (rock dissolution) or manmade voids (broken culverts, mine workings). Because they pose a significant risk to the safety of the traveling public, successful detection of buried voids is crucial for remediation to minimize the risk. Invasive testing methods such as the cone penetration test (CPT) and standard penetration test (SPT) could be used to obtain detailed information of voids, such as vertical sizes, depths, and filling materials (water, air, or raveled soils). However, the invasive methods such as penetration tests are too expensive or time-consuming to be performed densely along the roadway. Therefore, noninvasive geophysical methods are favorably used for void detection, as they can examine subsurface conditions over a larger volume of materials at lower costs and safer manners than invasive tests.

Among the noninvasive geophysical methods, seismic tomography methods are often used for detection of voids by using the refraction, reflection, and surface-wave components of wavefields. Applications of seismic tomography in engineering have been conducted to detect concrete and sandstone tunnels (Chen et al., 2016; Wang et al., 2018), abandoned mines (Sloan, 2017), and sinkholes (Tran et al., 2013; Tran and Sperry, 2018). These studies used active sources such as a sledgehammer or an accelerated weight drop to generate seismic waves. The active sources can produce high-frequency, short-duration (impulsive) source signatures with consistent energy at desired locations. Thus, high signal-to-noise ratio (SNR) data can be acquired, and high-resolution results can be achieved. However, the limitation of the active-source approach is that without specialized sources, the induced wavefields usually lack of low frequencies (<10 Hz),

which prohibit detection of deep voids (>10 m depth). In addition, the active sources could potentially trigger sinkhole collapses, particularly when enhancing the low frequencies by adding extra power or weight to the source. Thus, there is need for developing high-resolution passive-source tomography methods by taking the advantage of ambient noise rich in low-frequency components to characterize deep structures, while minimizing ground perturbation to avoid collapses.

Seismic interferometry has been widely used as a passive seismic method in seismology to determine the subsurface wave velocities at global or tectonic scale. This method uses the cross-correlation of ambient noise at different receivers to approximate the Green's function between these receivers, which is the impulsive (unit) dynamic response of the medium (the wavefield deconvolved of the applied source). The source of ambient noise includes, but not limited to, surface traffic, interior movements of earth, tides, and small earthquakes (microtremors). Conventional surface wave methods, such as the multi-channel analysis of surface waves (MASW, Park et al., 1999), have been combined with the seismic interferometry to estimate S-wave velocity distribution (Cheng et al., 2015; O'Connell and Turner, 2011) at the local scale (e.g., spread length less than 1 miles and depth less than 300 ft).

Because the wave-equation-based tomography methods have thrived in the past few decades, the seismic interferometry has been studied from a waveform inversion perspective. Like the full-waveform inversion (FWI. Mora, 1987; Tarantola, 1984), which iteratively refines the subsurface model of wave velocities by minimizing the misfit between the observed and simulated waveform records, the seismic interferometry inversion resolves the subsurface model by optimizing the misfit between the observed and simulated cross-correlation functions (used to approximate Green's functions). Toward the waveform inversion of seismic interferometry, cross-

correlation function simulation, structural and source kernels have been derived (Tromp et al., 2010). The field experimental applications have been conducted at global and local scales (de Ridder and Maddison, 2018; Sager et al., 2018). These successful endeavors motivated us to study the feasibility of detecting anomalies in the near surface (top 100 ft) by the waveform inversion of seismic interferometry.

1.2 Motivation and outline of the study

For assessment of roadway sinkholes, we have studied the waveform inversion of traffic noise interferometry. Traffic noise is generated by vehicles running over the road surface. A moving vehicle can be considered as a pressure load that pushes and then releases the elastic stratum. On a road segment, the traffic is a relatively consistent source of ambient noise because vehicles are restricted within a certain speed range. Relevant research has demonstrated that the Green's function of the surface waves could be approximated from the urban traffic noise, and the approximated Green's function can be used to determine the physical properties of the soil and bedrock beneath the roadway (Zhang et al., 2019; Li et al., 2020). However, the required assumption of energy balance at both sides of each receiver pair to retrieve the true Green's function is not satisfied for cases of individual vehicles passing by the receiver array in only one direction, without vehicles passing in opposing directions. Therefore, instead of using the approximated Green's function, we directly invert the cross-correlation function to extract the subsurface structures. Our approach estimates the source signatures and distribution from the field data and uses them for the forward simulation during the inversion, thus accounting for the source effects in analysis. Finally, the cross-correlation function is a measure of similarity of wavefields and is not a solution of wave equations, thus the existing 2D active-source FWI algorithm (Tran et al., 2013) cannot be used to invert it. In this project, we have developed a new 2D ANT method

to invert the noise cross-correlation for assessment of roadway subsidence/sinkholes and verified it with synthetic and field experimental data.

The 2D ANT method and algorithm was first developed and tested on synthetic data (chapter 2). The test configurations and optimal frequency content of noise fields required for analyses were also investigated to optimize field testing and data analysis efforts (chapter 3). The method was then applied to field experimental data at four Florida sites and verified by invasive tests (CPT and SPT) (chapter 4). Finally, the GUI software of the 2D ANT were developed, together with its user manual, for FDOT future uses (chapter 5).

Chapter 2 – DEVELOPMENT OF 2D ANT COMPUTATIONAL ALGORITHM (TASK 1)

2.1 Introduction

Task 1 is to develop a computational algorithm of the 2D ANT method for void detection, using synthetic (computational) traffic noise data. The work is done through computer simulations using synthetic models, consisting of cells with individual Vs, Vp values. Synthetic models including layering with buried voids are considered. Synthetic traffic noise data are simulated at a large range of frequencies from 5 Hz to 30 Hz, using a set of receivers and a moving source (similar to a vehicle). The data are then analyzed as if they were collected on a roadway, and velocity structures are determined from the data. Comparison of the interpreted models against the true (physical) models provide basis for the development, implementation and revision of the computational 2D ANT algorithm.

2.2 2D ANT algorithm

We have successfully developed the 2D ANT method and algorithm for void detection. The method includes a forward simulation of cross-correlation function, and an adjoint-state inversion for extraction of subsurface material property. Wave propagation is modeled by 2D P-SV elastic wave equations (Virieux, 1986; Levander, 1988). The numerical solution of the P-SV elastic wave equations (Tran and Hiltunen, 2012) is used for simulation of noise fields and Green's functions required for computing the cross-correlation function during inversion, as discussed below.

2.2.1 Forward simulation of cross-correlation function

Using the representation theorem (Aki and Richards, 2002), at location $\mathbf{x}^{\alpha}$, the relationship between the record signal $s(\mathbf{x}^{\alpha}, t)$ and the Green's function $G(\mathbf{x}^{\alpha}, \mathbf{x}, t)$ with a given source $f(\mathbf{x}, t)$ inside of domain Ω is

$$s^{\alpha}(t) = s(\mathbf{x}^{\alpha}, t) = \int_{-\infty}^{t} \int_{\Omega} G(\mathbf{x}^{\alpha}, \mathbf{x}, t-\tau) f(\mathbf{x}, \tau) d\Omega d\tau, \quad (1)$$

where t is time, $\boldsymbol{x}$ is a dummy variable representing an arbitrary location in domain Ω, and τ is a dummy variable such that $t - \tau$ is a measure of signal delay.

The outer integral of eq. 1 is a convolution in time, and equivalently it can be written as a multiplication in the frequency domain ω:

$$s^{\alpha}(\omega) = s(\mathbf{x}^{\alpha}, \omega) = \int_{\Omega} G(\mathbf{x}^{\alpha}, x, \omega) f(\mathbf{x}, \omega) d\Omega. \quad (2)$$

Depending on the problem of interest, $d\Omega$ can be a small area dxdy in 2D or a small volume dxdydz in 3D space. The cross-correlation function $C^{\alpha\beta}$ between the two signals s^{α} and s^{β} is explicitly given by:

$$C^{\alpha\beta}(t) = \int_{0}^{T} s^{\alpha}(\tau) s^{\beta}(t+\tau) d\tau, \quad (3)$$

where T is the maximum sampled time. This explicit formula of cross-correlation function requires that time series s^{α} and s^{β} are given. One needs first to perform the forward simulation for each source location individually to obtain seismograms s^{α} and s^{β}, and then use these two sequences to calculate $C^{\alpha\beta}$. However, using the explicit method alone is inadequate for inversion of the cross-correlation function. The inversion theorem of cross-correlation function (Tromp et al., 2010) requires that noise sources are spatially uncorrelated, which means each source needs to be excited individually during forward simulation to ensure that the wavefields with different sources do not interfere each other. Therefore, the explicit formula is not practical for the forward simulation because its computation is intensive when the number of sources in the domain Ω is large. To overcome this obstacle, we adopt the implicit simulation method (Sager et al., 2018), which

calculates $\mathrm{C}^{\alpha\beta}$ with a given source distribution function $\mathrm{S}(\mathbf{x},\omega)$ using reciprocity of Green's functions at receiver and source locations. Using the Fourier transform, an equivalent form of equation (3) is obtained as:

$$\mathrm{C}^{\alpha\beta}(\mathrm{t}) = \frac{1}{2\pi}\int \mathrm{s}^{\alpha}(\omega)\mathrm{s}^{\beta*}(\omega)\exp\,(\mathrm{i}\omega\mathrm{t})\mathrm{d}\omega, \tag{4}$$

with the asterisk denotes conjugation. In terms of the Green's function,

$$C^{\alpha\beta}(t) = \frac{1}{2\pi}\int\int_{\Omega''}\int_{\Omega'} \mathrm{G}(\boldsymbol{x}^{\alpha},\boldsymbol{x}',\omega)\,\mathrm{f}(\boldsymbol{x}',\omega)\,\mathrm{G}^{*}\left(\boldsymbol{x}^{\beta},\boldsymbol{x}'',\omega\right)\mathrm{f}^{*}(\boldsymbol{x}'',\omega)\exp(i\omega t)\,d\Omega'\mathrm{d}\Omega''\,d\omega. \tag{5}$$

In the above equation, $\boldsymbol{x}'$ and $\boldsymbol{x}''$ are two arbitrary locations in domain Ω. Integrals $\int_{\Omega'} d\Omega'$ and $\int_{\Omega''} d\Omega''$ denote the integration over domain Ω twice, distinctively.

Next, the cross-correlation function $\overline{C^{\alpha\beta}(t)}$ is averaged over many realizations:

$$\overline{C^{\alpha\beta}(t)} = \frac{1}{2\pi}\int\int_{\Omega''}\int_{\Omega'} \mathrm{G}(\boldsymbol{x}^{\alpha},\boldsymbol{x}',\omega)\,\mathrm{G}^{*}\left(\boldsymbol{x}^{\beta},\boldsymbol{x}'',\omega\right)\overline{\mathrm{f}(\boldsymbol{x}',\omega)\,\mathrm{f}^{*}(\boldsymbol{x}'',\omega)}\exp(i\omega t)\,d\Omega'\mathrm{d}\Omega''\,d\omega, \tag{6}$$

by stacking calculated cross-correlation functions over many time intervals (Bensen et al., 2007). By assuming that the noise is spatially uncorrelated, we therefore approximate $\overline{\mathrm{f}(\boldsymbol{x}',\omega)\,\mathrm{f}^{*}(\boldsymbol{x}'',\omega)}$ with a delta function in space as:

$$\overline{\mathrm{f}(\boldsymbol{x}',\omega)\,\mathrm{f}^{*}(\boldsymbol{x}'',\omega)} = S(\boldsymbol{x}',\omega)\delta(\boldsymbol{x}'-\boldsymbol{x}''), \tag{7}$$

with the source power-spectrum density (PSD) $S(\boldsymbol{x},\omega)$. For uncorrelated noise sources, eq. 6 becomes

$$\overline{\mathrm{C}^{\alpha\beta}(\mathrm{t})} = \tfrac{1}{2\pi}\int\int_{\Omega}\mathrm{G}(\mathbf{x}^{\alpha},\mathbf{x},\omega)\,\mathrm{G}^{*}\left(\mathbf{x}^{\beta},\mathbf{x},\omega\right)S(\mathbf{x},\omega)\exp(\mathrm{i}\omega\mathrm{t})\,\mathrm{d}\mathbf{x}\mathrm{d}\omega, \tag{8}$$

or in the frequency domain,

$$\overline{\mathrm{C}^{\alpha\beta}(\omega)} = \int_{\Omega}\mathrm{G}(\mathbf{x}^{\alpha},\mathbf{x},\omega)\,\mathrm{G}^{*}\left(\mathbf{x}^{\beta},\mathbf{x},\omega\right)S(\mathbf{x},\omega)\mathrm{d}\mathbf{x}. \tag{9}$$

Using eq. 9, we can simulate the cross-correlation function implicitly with a given distribution function of noise source, instead of dealing with noise events individually. The calculation of the

cross-correlation function (CCF) between $\mathbf{x}^{\alpha}$ and $\mathbf{x}^{\beta}$ starts with the two forward simulations to obtain Green's functions $G(\mathbf{x}^{\alpha}, \mathbf{x}, \omega)$ and $G(\mathbf{x}^{\beta}, \mathbf{x}, \omega)$ with sources at $\mathbf{x}^{\alpha}$ and $\mathbf{x}^{\beta}$, respectively. Then, multiply $G(\mathbf{x}^{\alpha}, \mathbf{x}, \omega)$ with the complex conjugate $G^{*}(\mathbf{x}^{\beta}, \mathbf{x}, \omega)$ and the noise source PSD $S(\mathbf{x}, \omega)$, and sum over all grid points (integration over space $\mathbf{x}$). Finally, the frequency-domain cross-correlation function is transformed to the time domain. In this study, the PSD is determined from the reverse-time beamforming of filtered CCF, and S(x,ω) is the same (average value) for all frequencies within the filtering frequency band.

We use the implicit method for the forward simulation of cross-correlation function during inversion to reduce the computing time. For simulation of traffic noise fields, as the distance between vehicle wheels (5-10 ft) is much smaller than the typical wavelength of vehicle-induced surface waves (30 to 50 ft), generated waves from individual wheels are not separated in time. Therefore, we use an equivalent point load and an estimated source-time function to represent a vehicle. In addition, the source uncorrelation may not be satisfied in the field, as vehicles may travel in a close group (multiple vehicles within the receiver spread). To alleviate this issue, noise data can be recorded over a long period (minutes) and the cross-correlation function is stacked over many time intervals. As the vehicle speeds are much less than the wave velocity [for example, vehicle speed of 80 mph (117 ft/s) and the typical S-wave velocity in soil of 400 - 1000 ft/s], most of passing vehicles can be considered as insolated sources (uncorrelated). The stacking over many time intervals would enhance the contribution of uncorrelated-source noise and diminish the effects of correlated-source noise from vehicles passing in a close group.

To verify the implicit approach (eq. 9), we compare explicit and implicit cross-correlation functions. In this study, wave propagation is modelled by 2D elastic wave equations as:

$$\begin{cases} \dfrac{\partial v_x}{\partial t} = \dfrac{1}{\rho}\left(\dfrac{\partial \sigma_{xx}}{\partial x} + \dfrac{\partial \sigma_{xz}}{\partial z}\right) \\ \dfrac{\partial v_z}{\partial t} = \dfrac{1}{\rho}\left(\dfrac{\partial \sigma_{xz}}{\partial x} + \dfrac{\partial \sigma_{zz}}{\partial z}\right) \\ \dfrac{\partial \sigma_{xx}}{\partial t} = (\lambda + 2\mu)\dfrac{\partial v_x}{\partial x} + \lambda \dfrac{\partial v_z}{\partial z} \\ \dfrac{\partial \sigma_{zz}}{\partial t} = (\lambda + 2\mu)\dfrac{\partial v_z}{\partial z} + \lambda \dfrac{\partial v_x}{\partial x} \\ \dfrac{\partial \sigma_{xz}}{\partial t} = \mu\left(\dfrac{\partial v_x}{\partial z} + \dfrac{\partial v_z}{\partial x}\right) \end{cases} \tag{10}$$

Where (v_x, v_z) is the particle velocity vector, (σ_{xx}, σ_{zz}, σ_{xz}) is the stress tensor, ρ is the mass density, μ, λ are Lamé's coefficients of material in the modelled domain. A three-layer model shown in Figure 2.1 is used. The model is discretized into a 100 × 60 grid (distance × depth) of 0.75 m (2.5 ft) spacing in both directions. There are eight point-load sources and each wavefield is recorded by twenty-four vertical geophones. The source moves from $x = 6$ m (20 ft) to $x = 69$ m (230 ft) with a 9-m (30-ft) interval. Only eight shot impacts are recorded for demonstration. For the receivers, locations range from 3 m (10 ft) to 72 m (240 ft) with a 3-m (10-ft) interval. Receiver #12 is selected as the reference station for cross correlating, which is located at 36 m (120 ft). It is noted that, for simulation of wavefield induced by a moving vehicle, there are several source impacts along the receiver line (see section 2.2.1 for detail).

For the explicit method, wavefield is generated by elastic wave equations for each source individually for 0.6-s recording time. Then eight shot-records are concatenated to generate a 4.8-s record (Figure 2.2) of simulated traffic noise. The spatial uncorrelation condition is satisfied because at any moment of the recording time there is at most one source impacting. To calculate the cross-correlation function, the entire record is divided into eight segments with 0.6-s length for each segment. Then eq. (3) is used to calculate the cross-correlation function for every receiver

pair. Stacking the calculated cross-correlation functions over time intervals, the result as the red curves in Figure 2.3 can be obtained.

For the implicit method, the source power spectral distribution function for point-load sources is defined as:

$$S(x,t) = \begin{cases} 1 & if\ source\ at\ x, \\ 0 & if\ no\ source\ at\ x. \end{cases} \tag{11}$$

We use eq. (10) to compute Green's function $G(x^{\alpha}, x, \omega)$ with the source at each receiver location, x^{α}. Following the mentioned calculation procedure, the implicitly simulated cross-correlation function as the black curves is obtained in Figure 2.3. The matched waveforms between red and black curves in Figure 2.3 demonstrate the identity of the explicit and the implicit method.

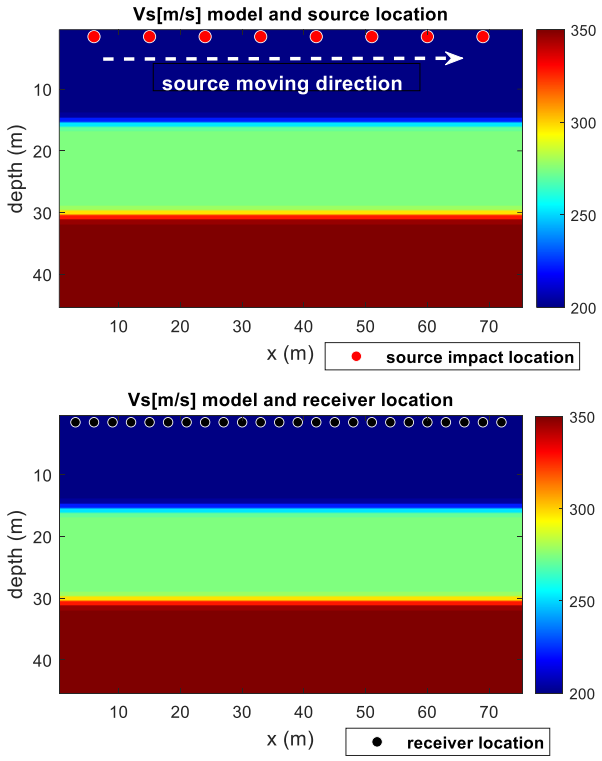

Figure 2.1. A three-layer shear velocity (Vs) model. (Top) Vs model and with moving sources. (Bottom) Vs model and receiver locations.

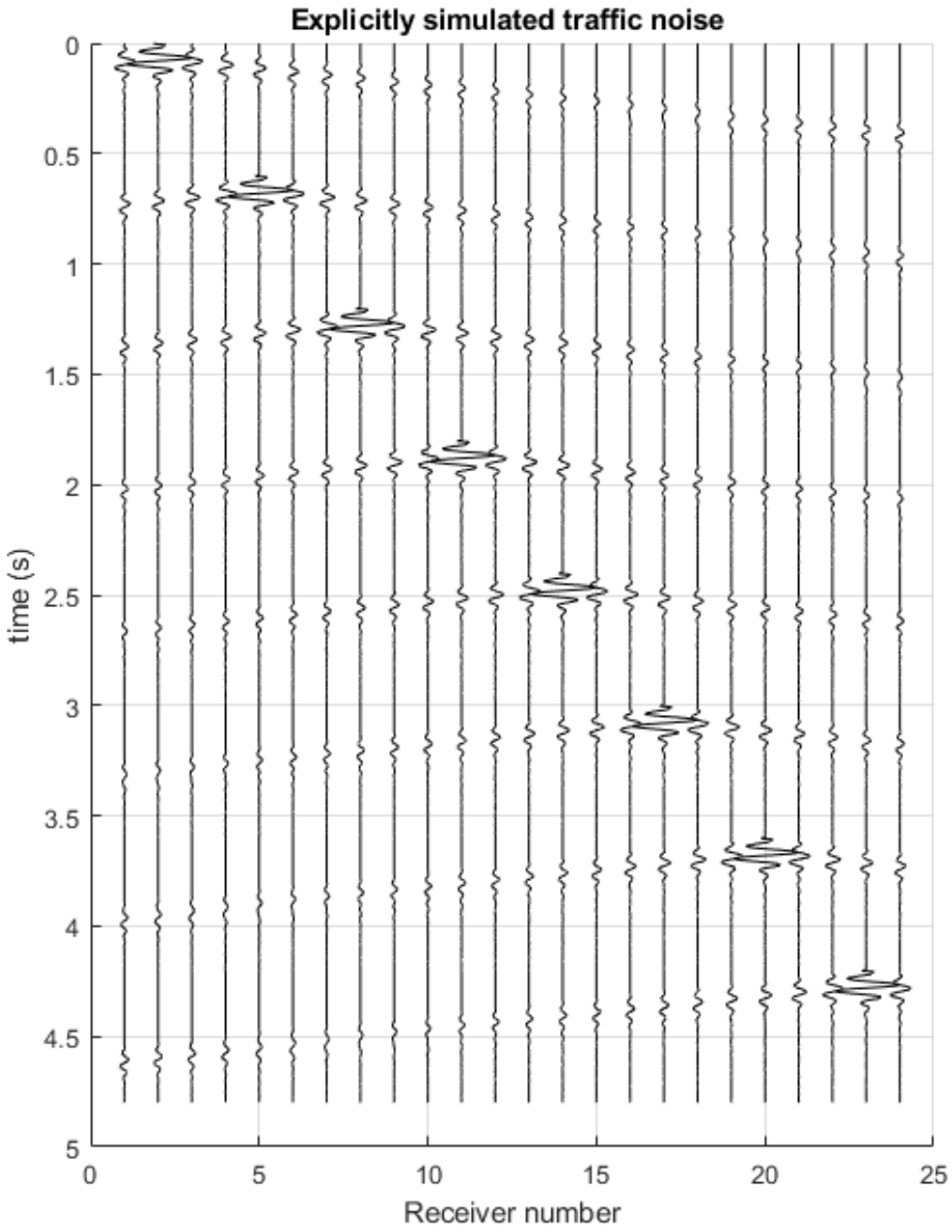

Figure 2.2. Simulated traffic noise using eight spatially uncorrelated sources. This 4.8-s dataset was generated by concatenating eight shot records of which lasts for 0.6 s each. For simulation of wavefield induced by a moving vehicle, there are several source impacts along the receiver line (section 2.2.1).

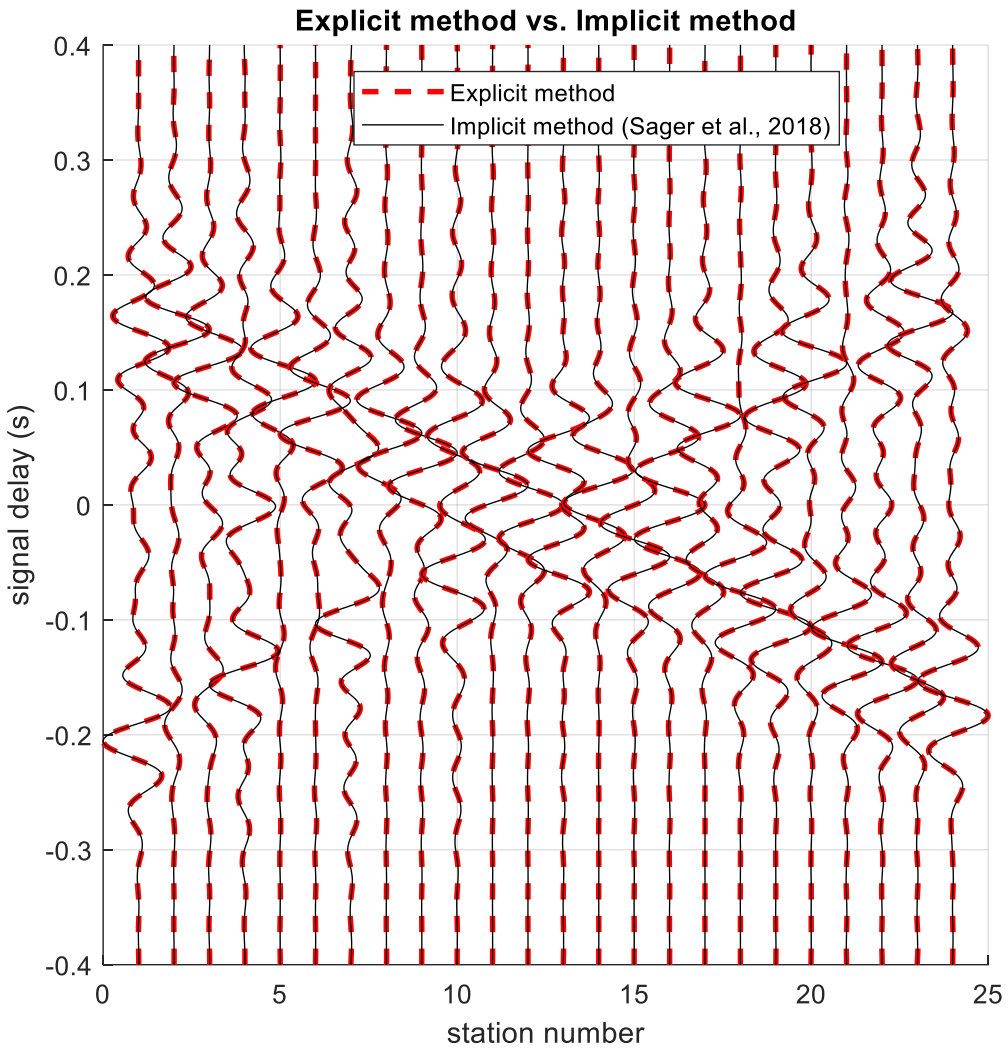

Figure 2.3. A comparison of synthetic cross-correlation functions from the explicit and implicit methods. Red curves: Cross-correlation functions simulated by using the explicit method. Black curves: Cross-correlation functions simulated by using the implicit method.

2.2.2 Inversion of traffic noise cross-correlation function

Since the cross-correlation function $C^{\alpha\beta}$ reveals the relationship between Green's functions with the source at x^{α} and x^{β}, respectively, inverting the cross-correlation function can retrieve subsurface material properties, such as Vs and Vp. Considering the misfit between the observed and the synthetic cross-correlation functions,

$$\delta C^{\alpha\beta} = C_{syn}^{\alpha\beta} - C_{obs}^{\alpha\beta}, \tag{12}$$

we use the L2-norm of misfit $\delta C^{\alpha\beta}$ as the objective function,

$$E = \frac{1}{2}\delta C^T \delta C = \frac{1}{2}\sum_{\alpha}\int dt \sum_{\beta} \delta C^2. \tag{13}$$

The gradients of E with respect to Lamé's parameters λ and μ are:

$$\begin{aligned}
\delta\lambda &= -\sum_{rec}\int dt \left[\frac{(\sigma_{xx}+\sigma_{zz})[(\varphi_{xx}^{+}+\varphi_{zz}^{+})-(\varphi_{xx}^{-}+\varphi_{zz}^{-})]}{4(\lambda+\mu)^2}\right], \\
\delta\mu &= -\sum_{rec}\int dt \{\frac{\sigma_{xz}(\varphi_{xz}^{+}-\varphi_{xz}^{-})}{\mu^2} \\
&\quad + \frac{1}{4}[\frac{(\sigma_{xx}+\sigma_{zz})[(\varphi_{xx}^{+}+\varphi_{zz}^{+})-(\varphi_{xx}^{-}+\varphi_{zz}^{-})]}{(\lambda+\mu)^2} \\
&\quad + \frac{(\sigma_{xx}-\sigma_{zz})[(\varphi_{xx}^{+}-\varphi_{zz}^{+})-(\varphi_{xx}^{-}-\varphi_{zz}^{-})]}{\mu^2}\},
\end{aligned} \tag{14}$$

Where σ is the stresses of forward-propagated wavefield and φ is the stresses of backward-propagated cross-correlation wavefield. φ is calculated by simultaneously backward propagating the differences between observed and simulated cross-correlation functions from all other locations x^{β} (Tromp et al., 2010). Note that the cross-correlation function $C^{\alpha\beta}(t)$ has a positive lag ($t > 0$) and a negative lag ($t < 0$), and they need to be calculated separately. $\varphi^{+}$and φ^{-} are used to represent the stress of back-propagated cross-correlation wavefield for the positive lag and the negative lag, respectively.

Using the relationships between P-wave velocity (Vp), S-wave velocity (Vs), Lamé's parameters λ, μ, and density ρ:

$$Vp = \sqrt{(\lambda + 2\mu)/\rho}\,, Vs = \sqrt{\mu/\rho},$$
$$\lambda = \rho \mathrm{Vp}^2 - 2\rho Vs^2, \mu = \rho Vs^2, \tag{15}$$

the gradients in terms of Vp and Vs can be written as:

$$\begin{cases} \delta Vp = 2\rho Vp \delta\lambda, \\ \delta Vs = -4\rho Vs \delta\lambda + 2\rho Vs \delta\mu, \end{cases} \tag{16}$$

The steepest descent direction of L2 misfit in terms of elastic velocities is obtained by eq. 16, and the material properties can be updated by:

$$\begin{cases} \mathrm{V_p^{n+1}} = \mathrm{V_p^n} + \theta_p^n \delta V_p^n, \\ \mathrm{V_s^{n+1}} = \mathrm{V_s^n} + \theta_s^n \delta V_s^n, \end{cases} \tag{17}$$

In eq. 17, step lengths θ_p and θ_s are calculated by a parabolic line search method (Nocedal & Wright, 1999; Sourbier et al., 2009b, 2009a). During the first iteration, the model $\boldsymbol{m}$ (Vs orVp) is updated along the steepest descent direction $\delta\boldsymbol{m}$.

$$\boldsymbol{m}_2 = \boldsymbol{m}_1 + \theta^1 \delta \boldsymbol{m}_1. \tag{18}$$

To accelerate the convergence rate, the model is updated along the conjugate direction $\delta\mathbf{c}$ for all successive iterations after the first iteration. Assigning $\delta\mathbf{c}_1 = \delta\boldsymbol{m}_1$, the conjugate direction at the n-th (n>1) iteration $\delta\mathbf{c}_n$ is calculated recursively by

$$\begin{cases} \delta \boldsymbol{c}_n = \delta \boldsymbol{m}_n + \beta^n \delta \boldsymbol{c}_{n-1}, \\ \boldsymbol{m}_{n+1} = \boldsymbol{m}_n + \theta^n \delta \boldsymbol{c}_n. \end{cases} \tag{19}$$

The conjugate gradient step length θ is estimated by the parabolic line search method. The weighting factor β^n is calculated by Polak-Ribière method (Klessig & Polak, 1972)

$$\beta_{PR}^{\mathrm{n}} = \frac{\delta \boldsymbol{m}_n^T (\delta \boldsymbol{m}_n - \delta \boldsymbol{m}_{n-1})}{\delta \boldsymbol{m}_{n-1}^T \delta \boldsymbol{m}_{n-1})}. \quad (20)$$

Any negative weighting factor is set to zero, or $\beta^{\mathrm{n}} = \max(0, \beta_{PR}^n)$, to reset the search direction to be the steepest descent direction when subsequent search direction loses conjugacy.

In summary, the 2D ANT inversion steps are as follows:

1) Process field data to obtain C^{obs}. Data processing includes removing mean, removing trend, normalizing traces, stacking cross-correlation functions over time intervals.
2) Use the solution of 2D elastic wave equations to calculate the forward propagating wavefield associated with model $\boldsymbol{m}$. Then, calculate synthetic cross-correlation function C^{syn} and residual $\delta C = C^{obs} - C^{syn}$.
3) Calculate objective function E($\boldsymbol{m}$) with L-2 norm.
4) Compute the steepest descent direction $\delta \boldsymbol{m}$ of the objective function by the adjoint-state method. For the first iteration, use $\delta \mathbf{c}_1 = \delta \boldsymbol{m}_1$. Starting from the second iteration, calculate the conjugate gradient direction $\delta \mathbf{c}_{\mathrm{n}}$.
5) Estimate the step length θ^{n} for model updating with the parabolic line search method.
6) Update the model as $\boldsymbol{m}_{n+1} = \boldsymbol{m}_n + \theta^n \delta \boldsymbol{c}_{\boldsymbol{n}}$.

2.3 Results

The 2D ANT algorithm must be tested on synthetic experiments with known Vs and Vp profiles to evaluate its accuracy, before applying to field experiments (Task 3). The synthetic experiment includes simulation of traffic noise and inversion of noise correlation function to extract Vs and Vp for comparison to their true values.

2.3.1 Simulation of traffic noise

The first numerical investigation is to compare synthetic data with field traffic noise data to show their similarity. This helps validate the required assumption for ambient noise analyses that field traffic noises are vehicle-induced seismic waves.

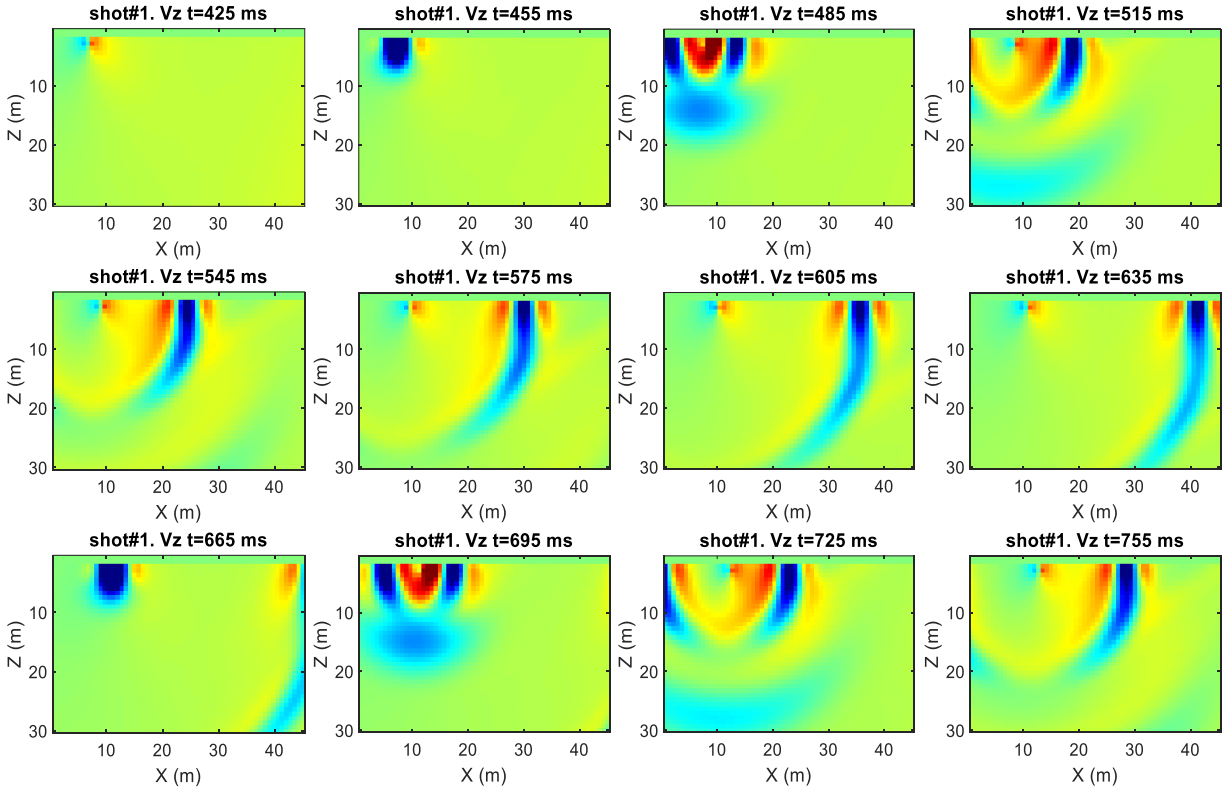

Figure 2.4. Snapshots of wavefield simulation.

The synthetic traffic noise is computed directly using eq. (10). We use a non-negative bell-shaped function in time to approximate the pressure induced by a vehicle running along the surface. Such perturbed bell-shaped functions are injected into the 2D medium along the surface from both directions to simulate passing vehicles. Figure 2.4 shows snapshots for the simulated wavefield. In this example, the vehicle moves across the modeled area from the left to the right. During the first 425 ms (Figure 2.4, top left), the vehicle moves about 6 m, so the vehicle speed is about 40 mph (64 km/h). The snapshots show that the perturbations by the bell-shaped load produce surface

waves. For example, at time $t = 455\ ms$, the vehicle triggers a source at $x = 8\ m$ (26 ft) and the induced surface waves start to propagate. And at time $t = 665\ ms$, the vehicle triggers another source at $x = 12\ m$ (40 ft) and surface waves start to propagate again.

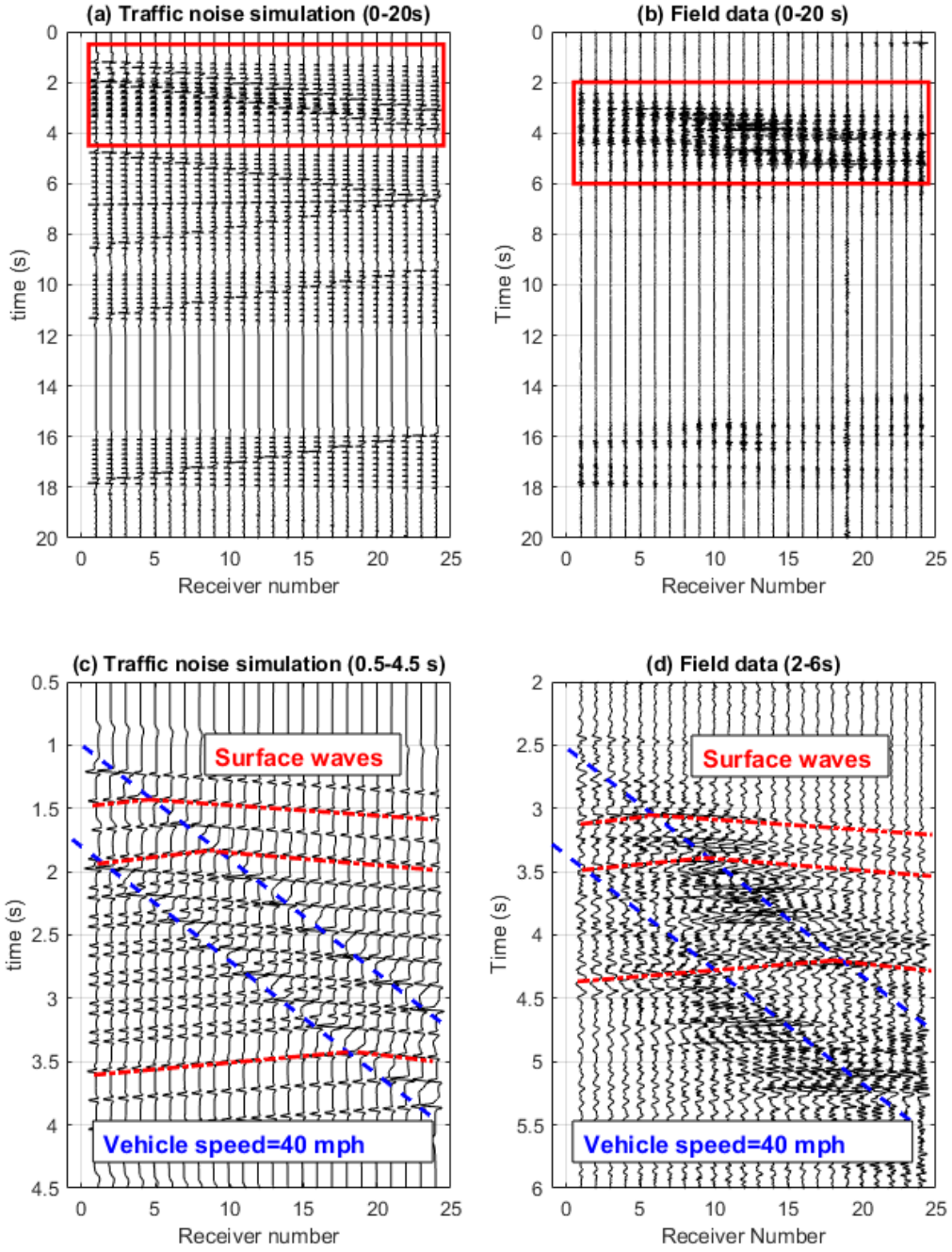

Figure 2.5. Data comparison: (a) synthetic 20-s-length simulated traffic noise data; (b) 20-s-length field data recorded on US-441 highway; (c) blow-up of data highlighted with red rectangle in (a); and (d) blow-up of data highlighted with red rectangle in (b).

Next, the simulated traffic noise is compared with field data to confirm that traffic noise is seismic waves. Synthetic traffic noise data (Figure 2.5a) are simulated by the finite difference solution of wave equations (eq. 10) with multiple vehicles passing by randomly in time and space in both directions (left to right and right to left). Figure 2.5c is a blow-up of the synthetic data from 0.5-4.5s, which is highlighted with a red rectangle in Figure 2.5a. The field data recorded at US-441 highway are shown Figure 2.5b, with a blow-up in Figure 2.5d. Interestingly, albeit that the field data are noisy, similarity can be observed from the comparison of the synthetic data with the field data. Both datasets show the direction of the moving source (vehicle) and surface wave propagation. It validates the assumption that traffic noises are indeed vehicle-induced seismic waves.

2.3.2 Analysis of a deep void at 30-m (100-ft) depth

The 2D ANT algorithm is first tested on a hypothetical soil profile with variable layers and a void embedded in the third layer at 30 m (100 ft) depth. The true model used for data generating is displayed as the top row of Figure 2.6. In the true Vs model (top left of Figure 2.6), the background Vs of the three layers from top to bottom is 350 m/s (1150 ft/s), 300 m/s (1000 ft/s), 400 m/s (1300 ft/s), respectively. The true Vp model is created from the true Vs model with a Poisson's ratio of 0.33. A 6-m (20-ft) diameter air-filled void is buried at 30 m (100 ft) depth (5-void diameters) at distance of 40 m (133 ft). The void Vs is zero and Vp is 340 m/s (1115 ft/s). For the initial model, the medium is set to be laterally homogeneous. From top to bottom, velocity increases linearly from 350 m/s to 400 m/s and from 700 m/s to 800 m/s, for the Vs and the Vp model, respectively.

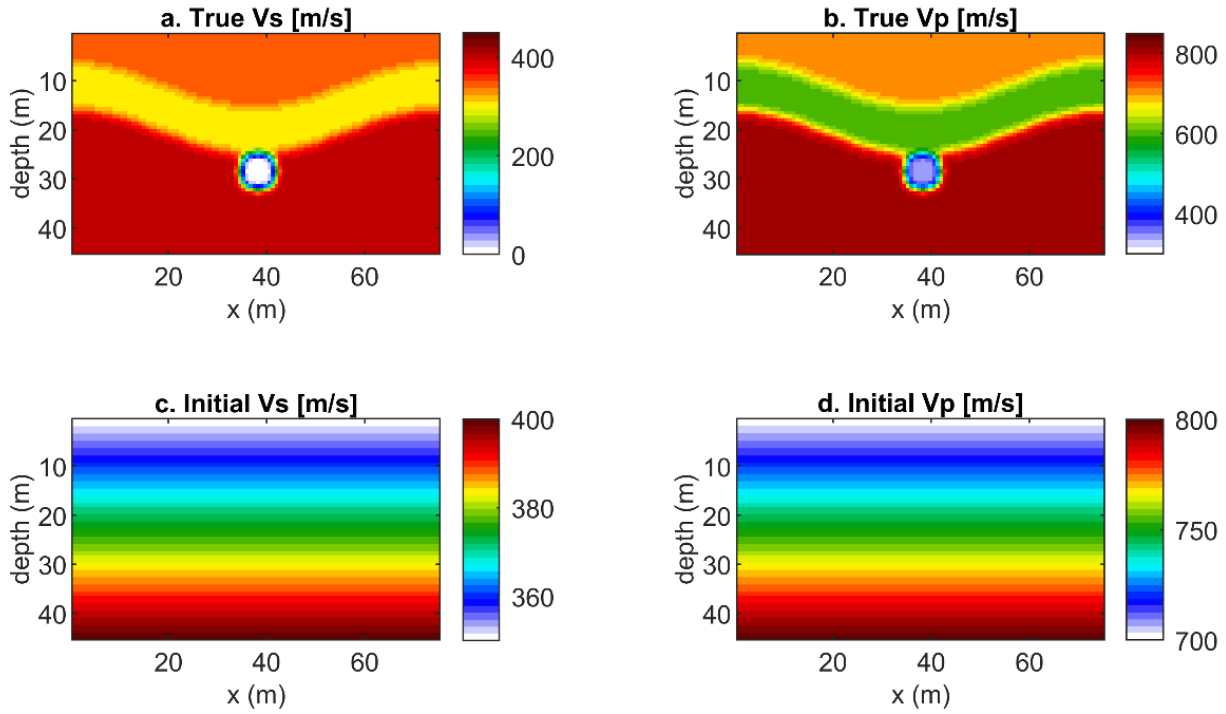

Figure 2.6. True and initial models of the one-void example: (a) True Vs; (b) True Vp; (c) Initial Vs; and (d) Initial Vp.

A power spectral distribution function $S(z) = \delta(z - 0)$ is used for generating observed data. This source function allows for the source to be evenly distributed along the surface, similar to a single vehicle passing by. Twenty-four vertical geophones are placed on the surface with a spacing of 3 m (10 ft) from 3 m (10 ft) to 72 m (236 ft).

The inversion analysis follows the methodology derived in the previous section. The inverted results are obtained after seventy (70) iterations. The inversion begins with low-frequency components (0~10 Hz) and increases the high-pass corner frequency by 5 Hz every fifteen iterations. The entire seventy iterations consist of five runs with frequency passing bands 0~10 Hz, 0~15 Hz, 0~20 Hz, 0~25 Hz, and 0~30 Hz, respectively. This multi-scale strategy (Bunks et al.,

1995; Ravaut et al., 2004), which increases higher frequencies gradually, helps to maintain inversion stability and robustness.

Figure 2.7 shows the final inverted velocity profile. In the inverted Vs profile (Figure 2.7a), the void is detected, and the interfaces of the variable layers are accurately located. The inverted Vs of the void is approximately 50 m/s (164 ft/s), which is close to the true value (0 m/s). In the inverted Vp profile (Figure 2.7b), the void is not detected. It is because the P-wave has much longer wavelength than that of the S-wave and thus not as sensitive to a deep anomaly (buried at depth of five diameters). Identifying the void in Vp profile requires P-wave components at high frequencies (up to 40 Hz), which are not typically available in field traffic noises. Thus, only Vs profiles will be charactered from the field data.

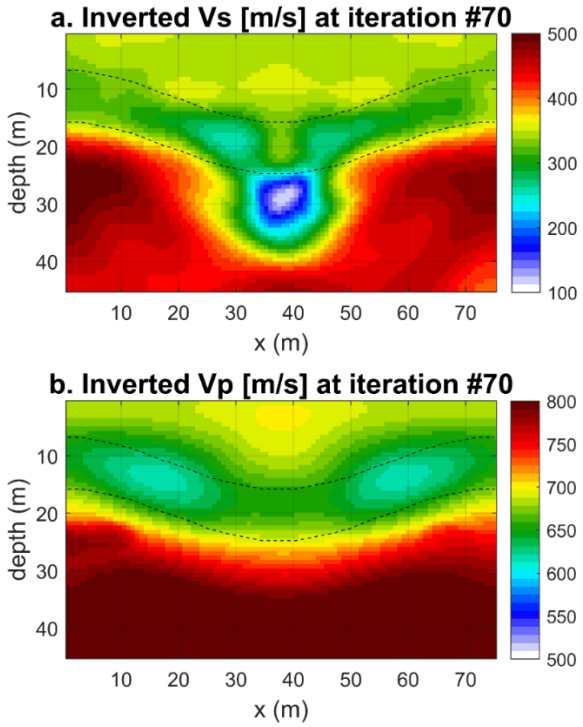

Figure 2.7. Inverted velocity profiles after seventy iterations: (a) Inverted Vs profile. All the three layers and the void are correctly located; and (b) Inverted Vp profile. The void is not detected in the inverted Vp.

To evaluate the performance of inversion, observed and simulated cross-correlation functions are compared in Figure 2.8a for reference station #1, which is located at x=3 m (10 ft). The initial simulated cross-correlation functions (blue dashed curves) are obviously off the observation (red curves), which is generated by using the true model. Misfit in the waveform can be observed between signal lag -0.2 s and 0.2 s. After seventy iterations, the inversion reduces the misfit between the simulation (black curves) and the observation.

Alternatively, analyzing the observation-simulation residual also helps to determine the performance of inversion. For reference station #1, we compare the normalized residual of cross-correlation function for the first iteration (red curves) and the last iteration (blue curves) in Figure 2.8b. Each set of residuals is computed by subtracting the simulated cross-correlation function from the observation. Both residual sets are normalized by dividing the maximum absolute value of the initial residual. The comparison indicates that the inverted model generates much smaller residuals. However, residuals are still nontrivial after seventy iterations, especially at stations that are close to the reference station. They could be minimized further by using a gradient formula with higher-order derivatives of the objective function, but this would require more computer time.

The comparison is carried out on a cross-correlation function obtained at a station-pair with the largest offset (69 m; 230 ft) in Figure 2.8c. The improvement in waveform fitting is evident in this comparison. The peaks around ± 0.2 s of the initial simulation have earlier arrival times, because of the absence of the low-velocity layer in the initial model. On the contrary, the simulation at the seventieth iteration has approximately the same peak arrival time with the observation. Between the time delay ± 0.1 s, the misfit of the waveform is significantly reduced after inversion. Overall, the inversion has drastically minimized the misfit between simulation and observation.

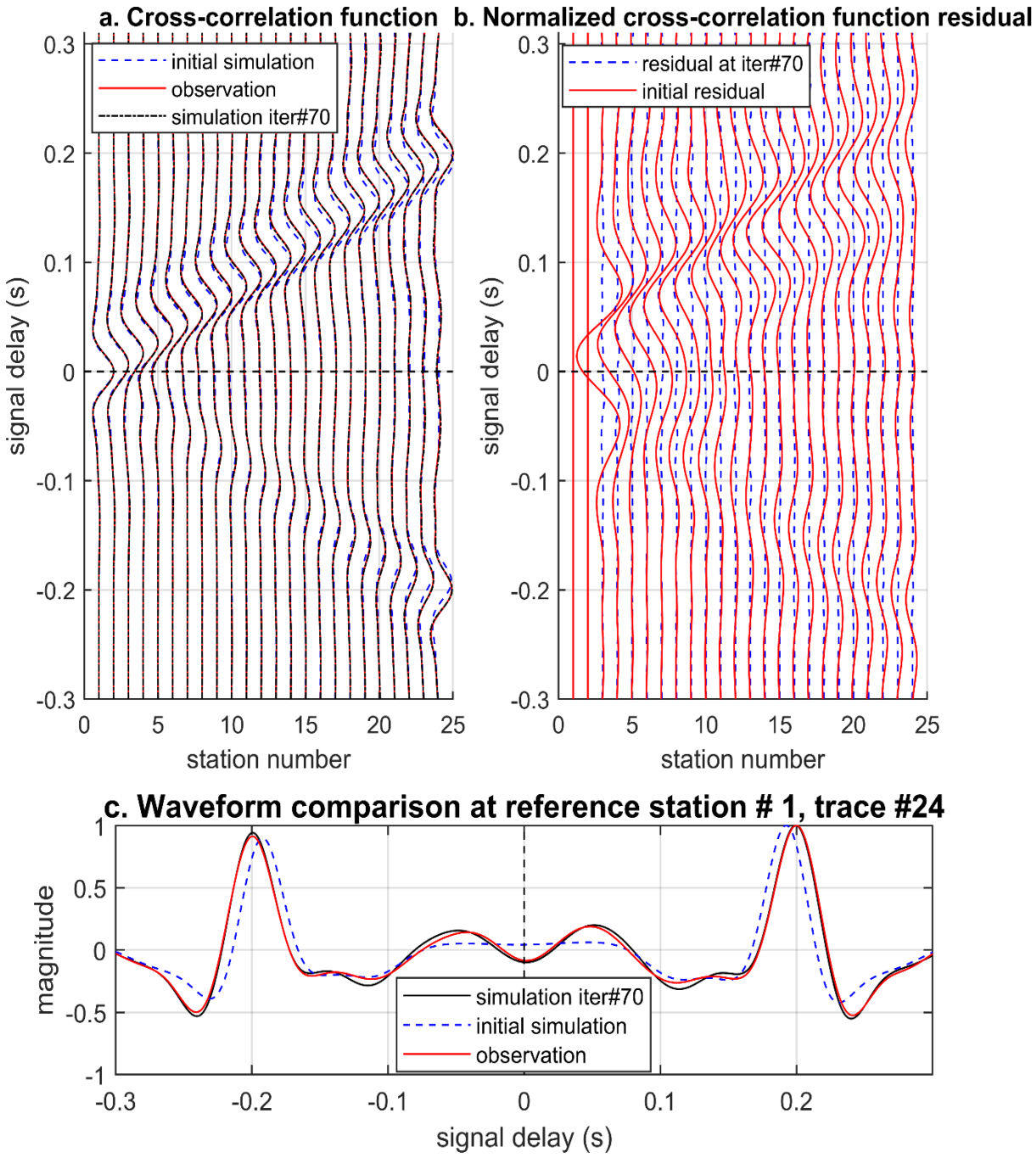

Figure 2.8. Cross-correlation function waveform comparison: (a) Cross-correlation function comparison for reference station #1; (b) Normalized cross-correlation function residual comparison for reference station #1; and (c) Cross-correlation function comparison at reference station #1, trace #24.

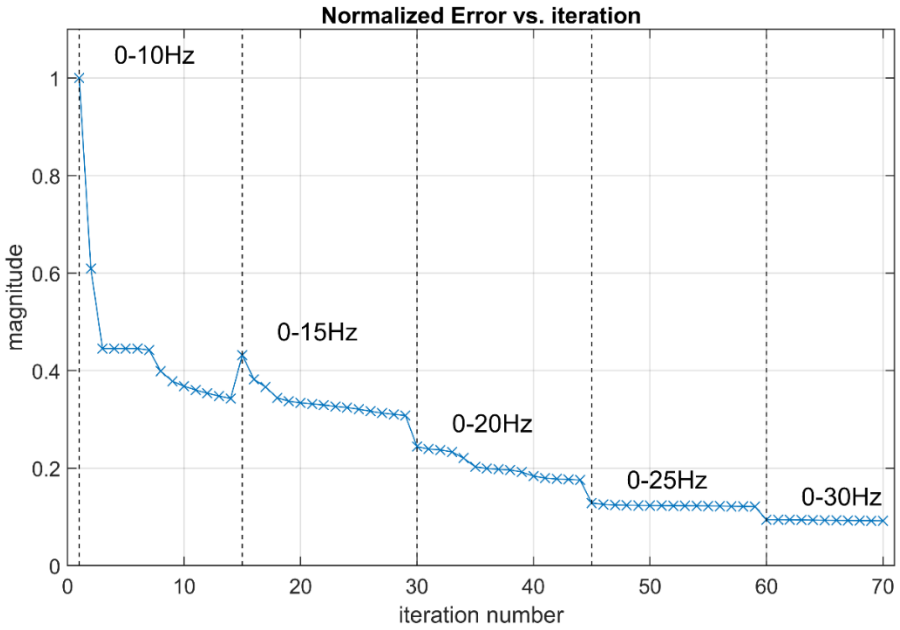

Figure 2.9. Normalized error versus iteration number for all five runs. Error of each iteration is normalized by dividing to the initial error.

Change of the normalized error for each iteration against iteration number is shown in Figure 2.9. Each error value is normalized by dividing by the initial error at iteration 1. Therefore, the error curve starts with magnitude 1 and decreases gradually. As the frequency band gets wider, more high-frequency components are used by the inversion. It takes more effort to optimize the high-frequency misfit, which is caused by smaller sized structures. Therefore, the convergence rate (slope of the curve) is getting lower as the iteration number increases.

Inverted results for each of the five runs are shown in Figure 2.10. It is observed that the background model and the characteristics of the three layers are retrieved after the first two runs. The later three runs resolve the void and refine the model gradually. If only detecting the void and depth of interfaces of the three layers, only thirty iterations (data up to 15 Hz) are needed.

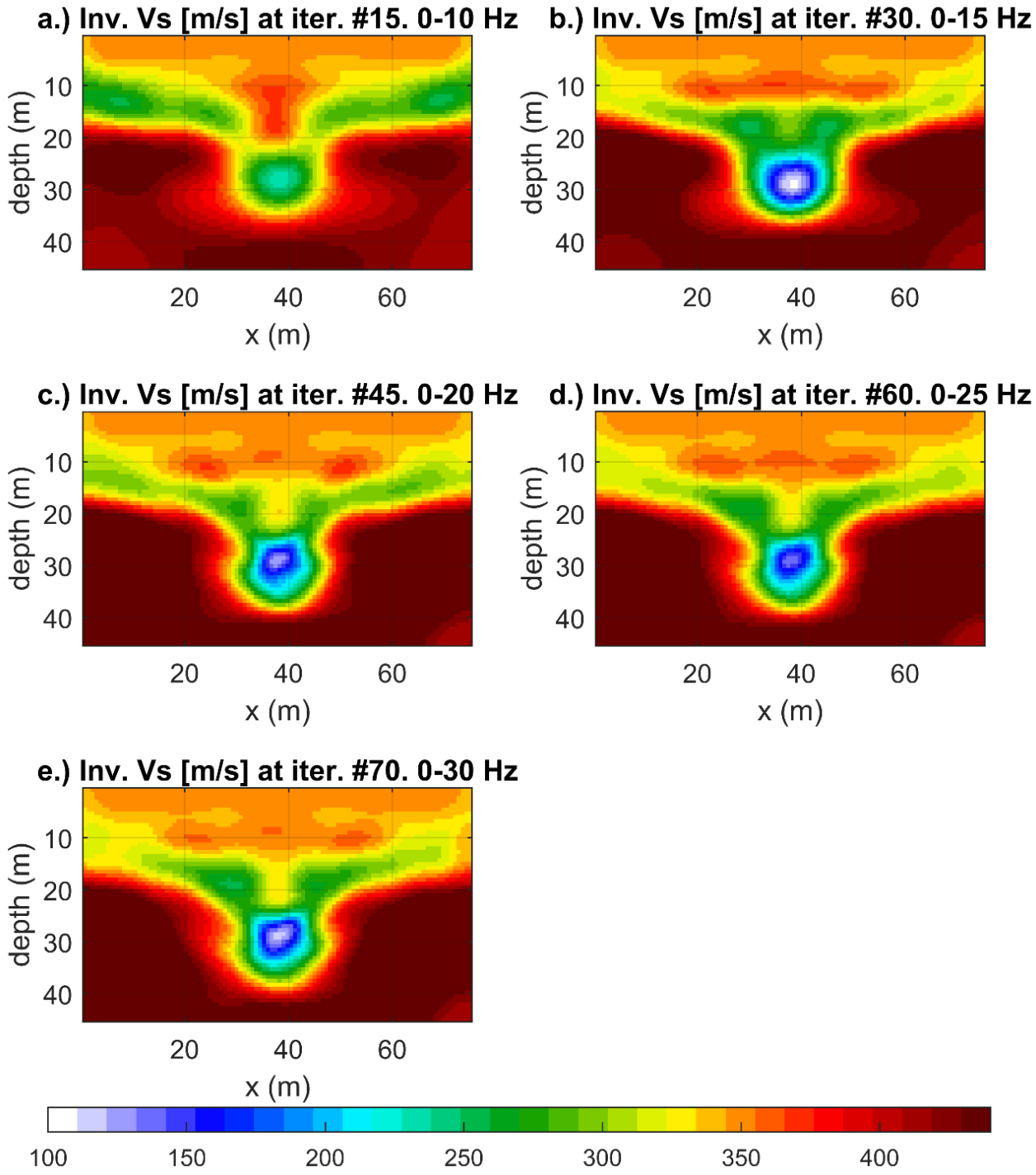

Figure 2.10. Results for the five inversion runs. The corresponding iteration number and frequency-passing band are displayed in the title of each panel.

2.3.3 Analysis of two voids at different depths

The feasibility of the proposed ANT method has been demonstrated by the one-void numerical example, of which the true velocity model is axisymmetric. To further examine the method's capacity of imaging deep structures, it is tested on a complex two-void model (Figure 2.11). This model has two 8-m (26-ft) diameter voids embedded in deeper layers at 20 m (66 ft) and 30 m (100 ft) depths. It is more complex than the above one-void model because the two voids are close and at different depths, which create interactions between wavefields scattered from the different voids. Since the background model – the three variable layers – remains the same as in the one-void example, we directly adopt the same initial model. All other settings, such as the station locations and inversion parameters, remain the same with what were used in the one-void example.

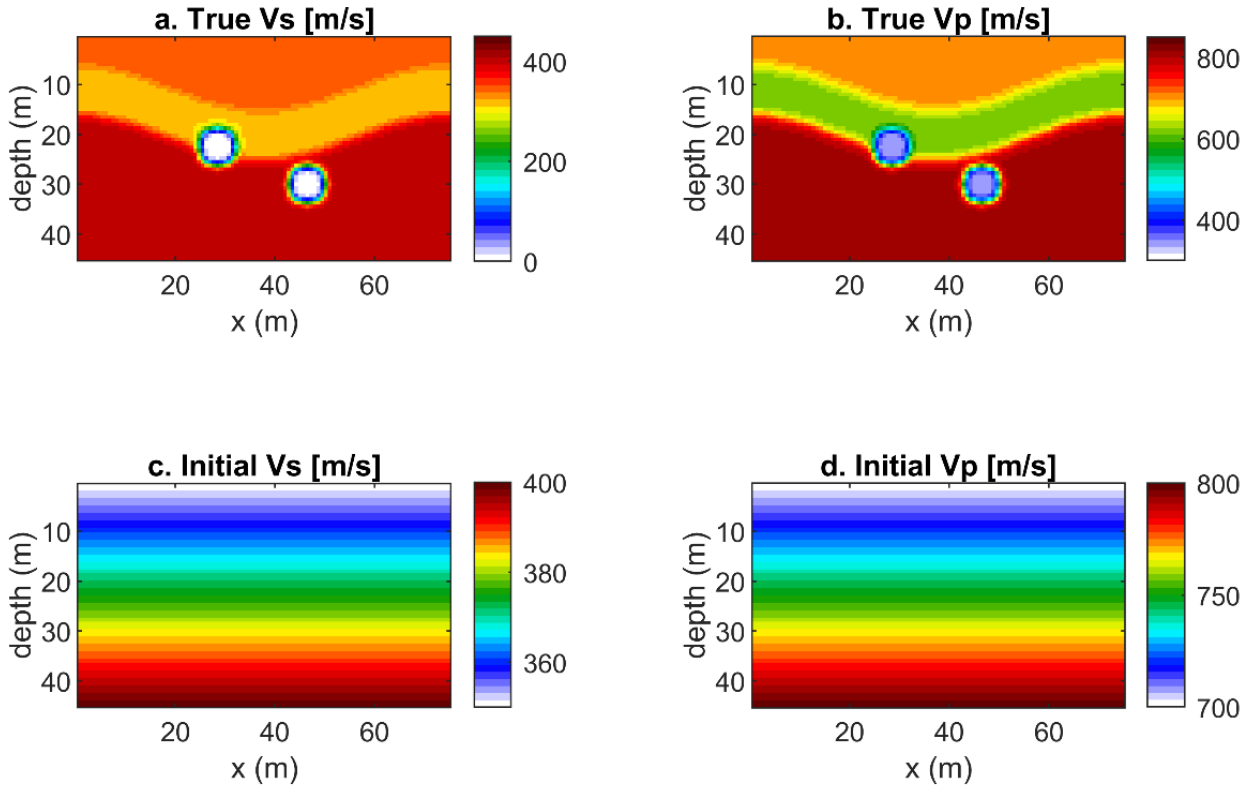

Figure 2.11. True and initial models of the two-void example: (a) True Vs; (b) True Vp; (c) Initial Vs; and (d) Initial Vp.

After seventy iterations, the inverted Vs and Vp profiles are obtained as presented in Figure 2.12. In the inverted Vs profile (Figure 2.12a), the two voids are detected at the correct locations and depths. The layer interfaces are accurately located, except at the region close to the two voids. This is caused by the model complexity from the scattered wavefield bouncing between the two voids. For the inverted Vp profile (Figure 2.12b), like what was observed in the previous example, the layer boundaries are accurately located regardless of the increased model complexity, which suggests that the compressional wavefield is less sensitive to the near-surface fine structures.

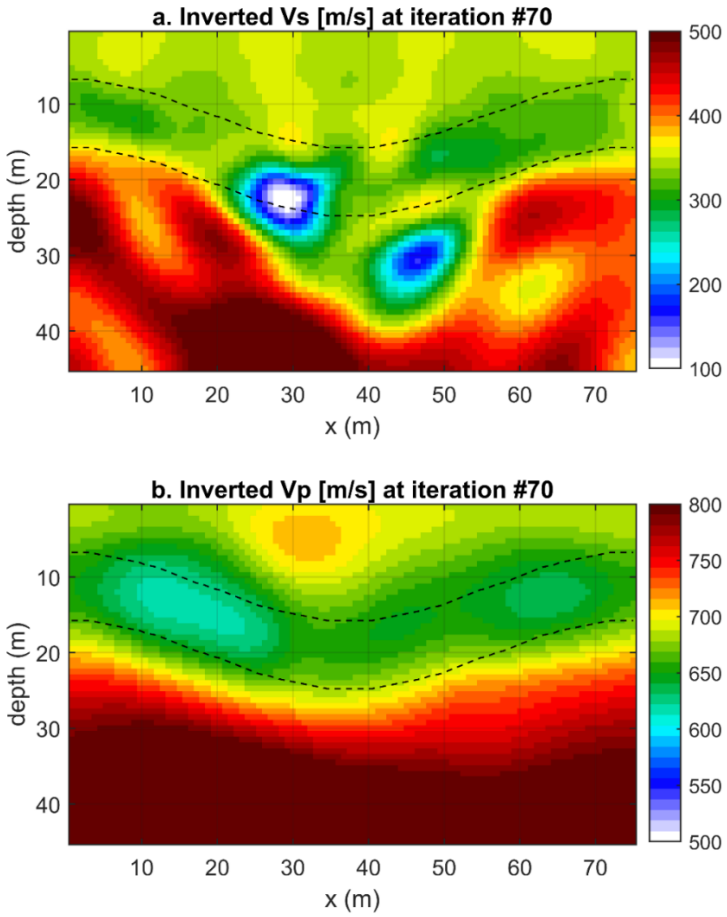

Figure 2.12. Inverted velocity profiles after seventy iterations: (a) Inverted Vs profile. All the three layers and the void are correctly located; and (b) Inverted Vp profile. The void is not detected in the inverted Vp.

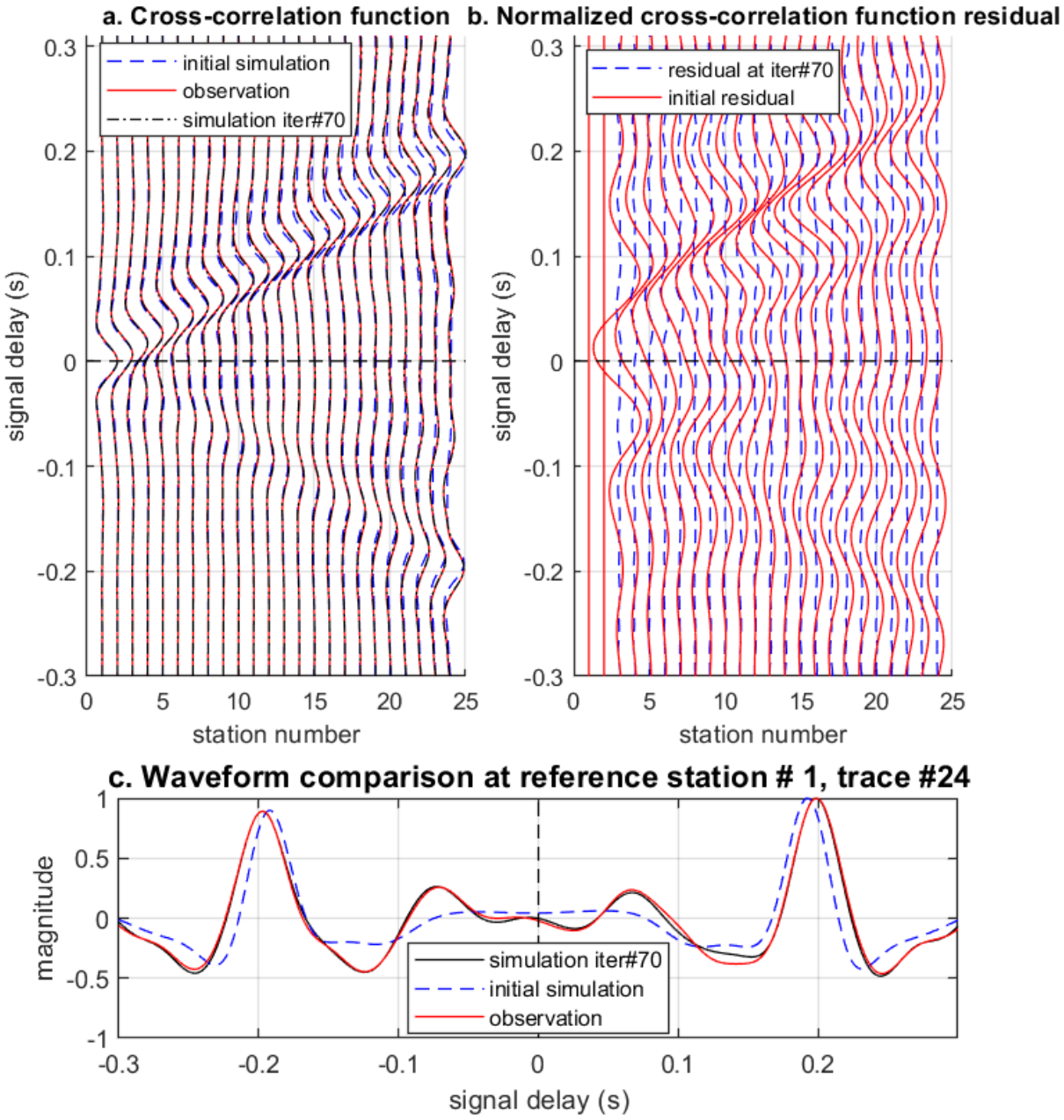

Figure 2.13. (a) Cross-correlation function comparison for reference station #1; (b) Normalized cross-correlation function residual comparison for reference station #1. Both residual sets are normalized by dividing the maximum absolute value of the initial residual; and (c) Cross-correlation function comparison at reference station #1, trace #24.

Waveform comparisons are carried out to evaluate the performance of the inversion in the two-void example. The cross-correlation function waveforms and the normalized cross-correlation function residual are compared in Figure 2.13a and 2.13b, respectively. The misfit in the waveforms has been optimized and the residual is trivial after seventy iterations. A detailed waveform comparison of a single trace is shown by Figure 2.13c, in which the observation and simulation are compared at the reference station #1, trace #24. For this station pair, the two receivers are 69 m (230 ft) apart. The comparison evidently shows the improvement of the waveform misfit during inversion. The observed and simulated data have approximately the same waveform shape and arrival time.

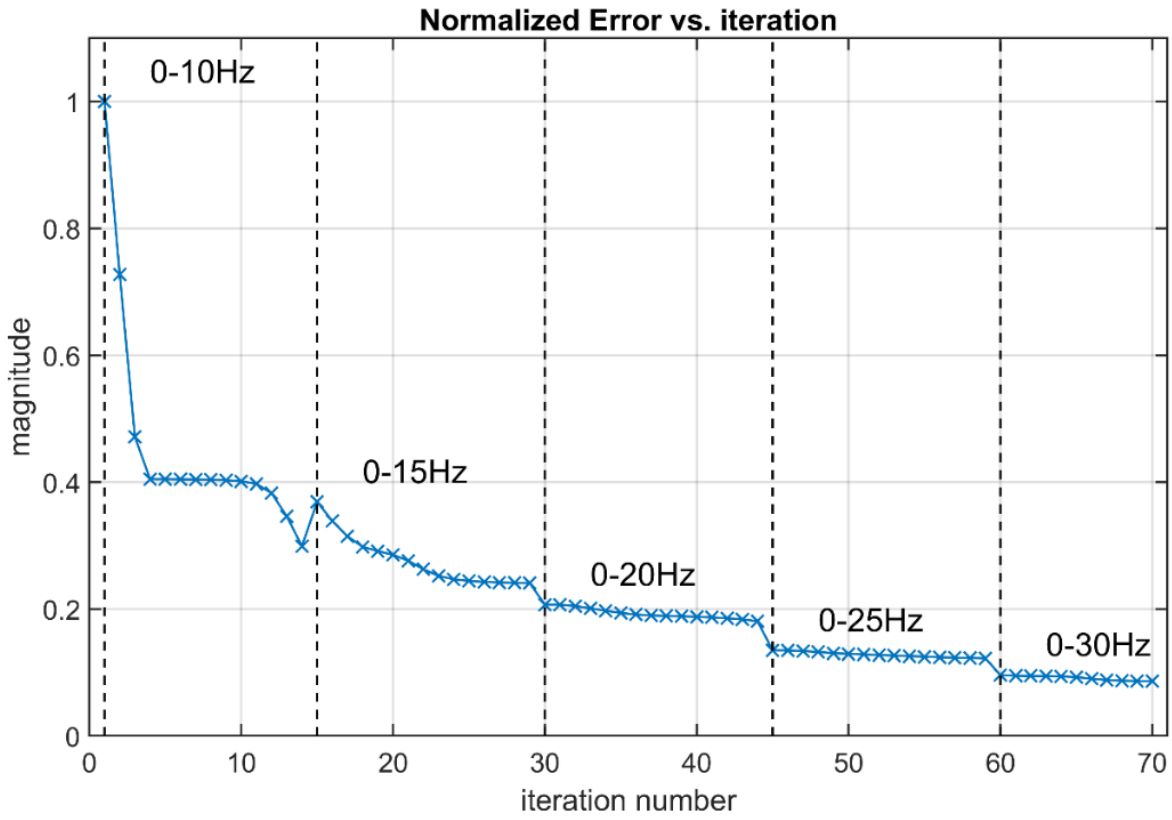

Figure 2.14. Curve of normalized error versus iteration number for all five runs. Error of each iteration is normalized by dividing the initial error.

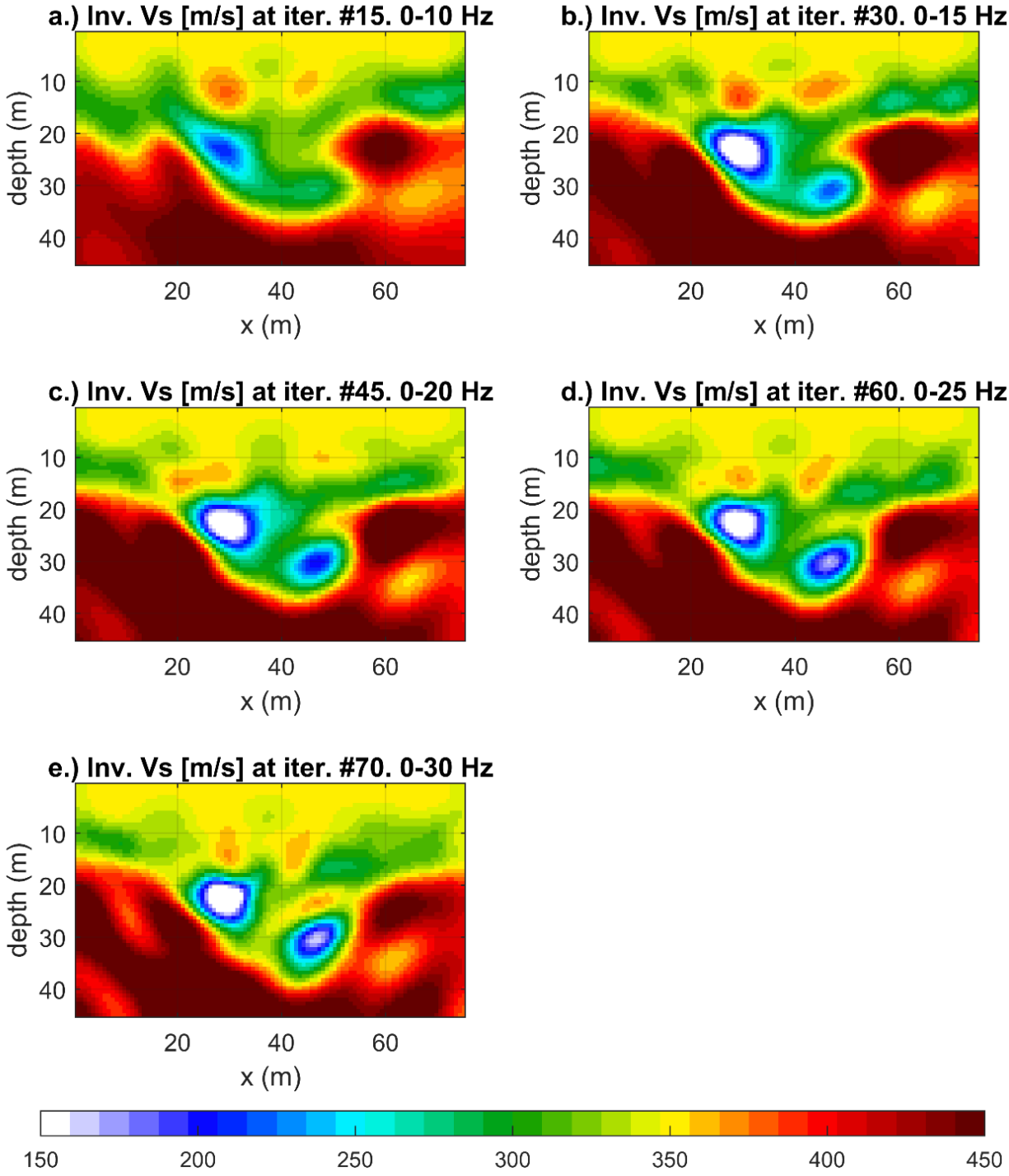

Figure 2.15. Results for the five runs of inversion. The corresponding iteration number and frequency-passing band are displayed in the title of each panel.

Change of the normalized error is shown in Figure 2.14. Each error value is normalized by dividing by the initial error at iteration 1. Similar to the previous one-void example, as the frequency band gets wider, higher high-frequency components are used by the inversion. The normalized error of the seventieth iteration is approximately 10% of the initial error, which indicates the misfit in waveform has been drastically minimized.

Inverted results for each of the five runs are shown in Figure 2.15. Interestingly, as the number of iterations increases, the shallow void at 25-m (83-ft) depth is detected earlier than the deep void at 45-m (150-ft) depth. Due to the spherical spreading and the decay of the wavefield, the scattered information from the shallow void is higher in magnitude and accounts for a larger contribution to the waveform misfit than the deep void. With the help of the multi-scale strategy, the inversion has successfully detected the two voids distinctly. These results demonstrate that the developed 2D ANT method is capable of imaging the deep voids and complex subsurface structures.

2.4 Conclusion

A novel 2D ambient noise tomography (2D ANT) algorithm has been successfully developed for void detection. We derived the theory for noise correlation function and developed the 2D ANT algorithm that works specifically for traffic noise. The algorithm consists of the following steps:

I. Calculating measured cross-correlation function ($C_{obs}^{\alpha\beta}$) between noise recordings for all possible pairs of receivers.

II. Simulating synthetic cross-correlation function ($C_{syn}^{\alpha\beta}$) with eq. (9) and the procedure included in this report.

III. Optimizing the misfit between the synthetic and measured cross-correlation function to retrieve 2D profiles of subsurface elastic velocities.

Two numerical void-detection examples are provided. A one-void model, which has spatially variable layers of Vs and Vp and a void at 30-m (100-ft) depth, is first used to test and refine the 2D ANT algorithm. A two-void model is followed to verify the algorithm's capacity of imaging complex structures. In both examples, the inverted Vs profiles demonstrate the great capabilities of the developed algorithm. The algorithm accurately characterizes the variable layers and detects voids at large depths [20 m (66 ft) and 30 m (100 ft)].

Chapter 3 – OPTIMIZATION OF TEST CONFIGURATIONS AND INVESTIGATION OF AMBIENT NOISES CHARACTERISTICS (TASK 2)

3.1 Introduction

The advanced 2D ambient noise tomography (2D ANT) algorithm was successfully developed in Task 1. The goal of this task was to identify the optimal test configurations (receiver number and spatial density) and noise characteristics (frequency content) for detection of voids at various sizes and depths by the 2D ANT. To achieve this, a number of parametric studies were performed with synthetic (computational) models. The objective was to relate the sizes and embedment depths of targeted voids to the test configurations and frequency content. The test configurations identified in this task were used for field experiments to minimize the efforts of field test and data analysis. The required frequency content was checked during field experiments to enable accurate results.

For the parametric studies, two synthetic models (hypothetical soil/rock profiles) were designed to represent the typical Florida geological condition with soils underlain by variable bedrock. One model includes a small shallow void of 3.75-m (12-ft) diameter at 12-m (40-ft) depth, and the other includes a large deep void of 9-m (30-ft) diameter at 24-m depth (80 ft). For each model, cross-correlation functions were simulated with a range of test configurations and analyzed by the developed 2D ANT algorithm. For the small shallow void, survey lines of receivers on the surface at various spacing at 1.5 m (5 ft), 3.0 m (10 ft), and 4.5 m (15 ft) were studied. For the large deep void, the tested receiver spacing is 1.5 m (5 ft), 3.0 m (10 ft), 6.0 m (20 ft), and 9.0 m (30 ft). For each test configuration, noise data were generated and inverted at different frequency ranges. The accuracy and resolution of inverted profiles were compared among the simulations to identify the optimal test configurations and required frequencies.

Based on processing of actual traffic noise data, low frequency (<25 Hz) components carry most of the high-quality signal energy. Therefore, the frequency range of interest is set to 5~20 Hz and 0~25 Hz for the shallow and deep voids, respectively. The recovery of P-wave velocity (Vp) profile requires high-quality P-wave components up to 40 Hz. Since P-waves at high frequencies are rarely available in field traffic noises, only inverted Vs profiles are used as the criterion for selection of test configurations in this task.

3.2 Small shallow void (12-ft diameter at 40-ft depth)

3.2.1 Test configuration

The developed 2D ANT algorithm in Task 1 was tested on a synthetic model with variable layers and a shallow buried void. The model domain of 37.5 m × 22.5 m (125 ft × 75 ft) (length × depth) consists of three layers, with Vs of 350 m/s, 300 m/s, and 400 m/s from the top to the bottom, respectively (Figure 3.1a). Poisson's ratio of 0.33 was assumed for the entire medium to calculate Vp (Figure 3.1b). The void is 3.75 m (12 ft) diameter with Vs = 0 m/s; Vp = 300 m/s (air filled void) and located 12 m (40 ft, more than three void diameters) below the free surface.

Three test configurations were analyzed to investigate the minimum number of receivers that enabled a successful recovery of the subsurface features including the embedded void. The tests were carried out with increasing number of receivers. The test configures are shown in Figures 3.2 to 3.4. Figure 3.2 shows the least dense test configuration that includes 8 receivers (black dots) placed on the surface at 4.5-m (15-ft) spacing. Figure 3.3 shows the medium dense test configuration of 12 receivers at 3-m (10-ft) spacing. Lastly, Figure 3.4 shows the densest test configuration of 24 receivers at 1.5-m (5-ft) spacing. It is noted that the receiver spacings used in three cases is less than two void diameters.

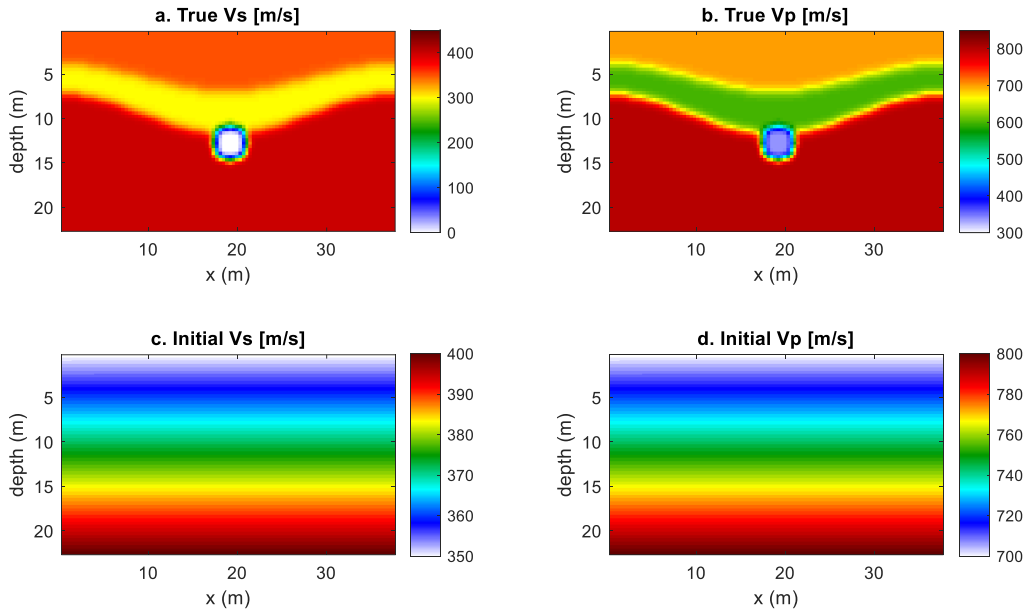

Figure 3.1 Synthetic model with a shallow void of 3.75-m diameter at 12-m depth

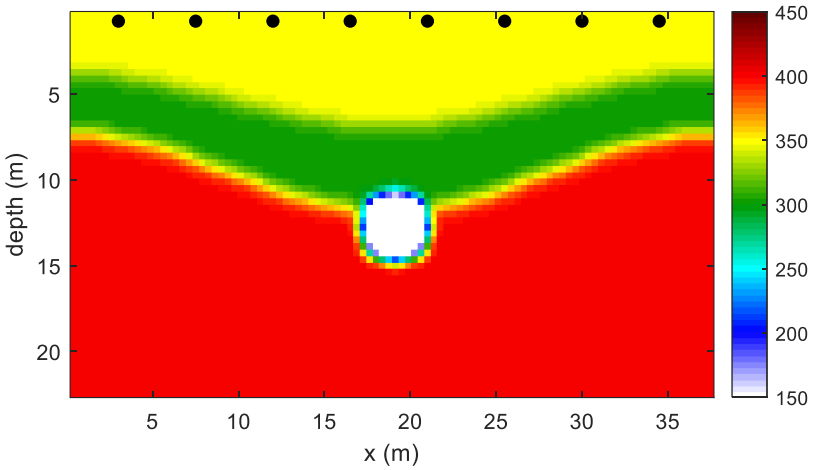

Figure 3.2. Test configuration 1: 8 receivers (black dots) at 4.5-m (15-ft) spacing.

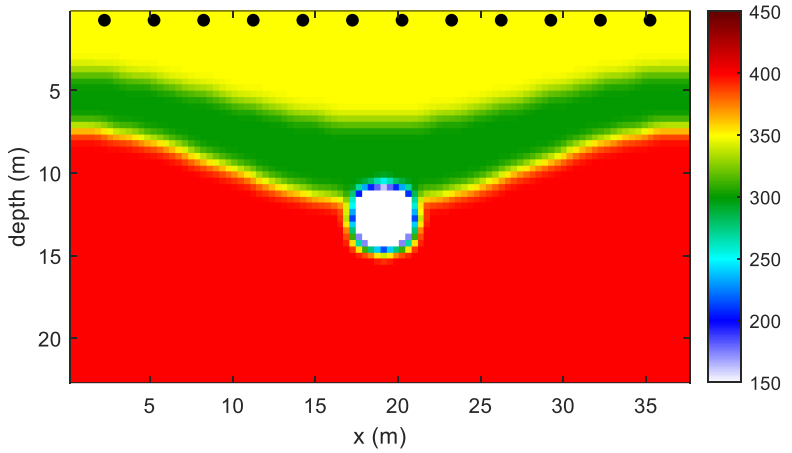

Figure 3.3. Test configuration 2: 12 receivers (black dots) at 3.0-m (10-ft) spacing.

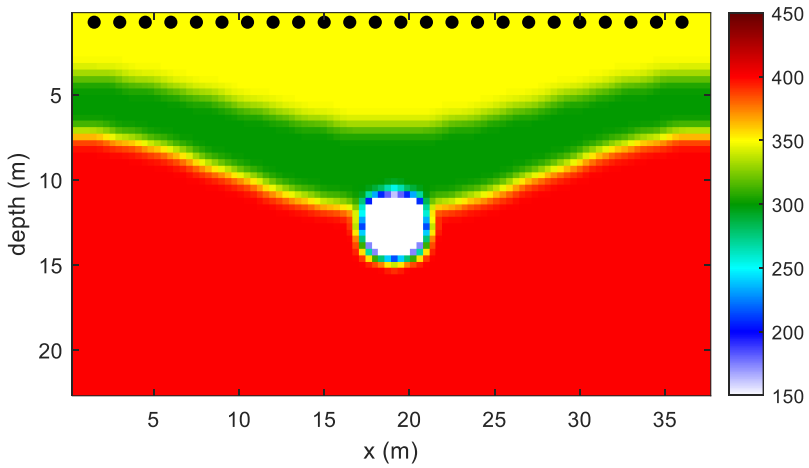

Figure 3.4. Test configuration 3: 24 receivers (black dots) at 1.5-m (5-ft) spacing.

3.2.2 Results for test configuration 1 (8 receivers)

The inversion analysis was first carried out for the least dense configuration of 8 receivers (Figure 3.2). The initial model used in the analysis is a 1D velocity profile that linearly increases with depth with Vs of 350 m/s on the free surface to 400 m/s at the bottom of the model (Figure 3.1c). The initial Vp (Figure 3.1d) is twice that of Vs. Two inversion runs were conducted. The first run began with the low frequency range (5-15 Hz) data on the initial model. The second run

was performed with the higher frequency range (5-20 Hz) data using the inverted result from the first run as the input model. Both runs stopped after 15 iterations.

The inverted Vs profiles of the two inversion runs are displayed in Figure 3.5. The true model features including the void location and the layer layout were generally recovered in the first run (Figure 3.5a). The second run with higher frequencies at 5-20 Hz improved the inverted model from the first run, particularly at the void region (Figure 3.5b). The void location and size are imaged correctly, but the inverted Vs of the void is about 220 m/s (730 ft/s), which is much larger than the true value of 0 m/s. This is due to limited signal coverage at the void location by the coarse receiver array.

Normalized least-squares error for all iterations of the two inversion runs are shown in Figure 3.6, where the error reduced from 1.0 at the first iteration to about 0.25 at the final iteration of the first run, and to 0.4 in the second run. A waveform comparison of the observed and simulated cross-correlation functions is provided in Figure 3.7a. The red curves are the observed cross-correlation function after band-pass filtering at 5-20 Hz. The blue and black dash lines are the initial and final simulated cross-correlation function, respectively. At the far-field traces 16 to 24, the improvement of data fitting is evident. For comparing cross-correlation residuals at the first and last iterations (Figure 3.7b), the residuals are minimized considerably during inversion. For the station pair with the largest offset (first and last receivers), the improvement in data fitting is clearly shown in (Figure 3.7c).

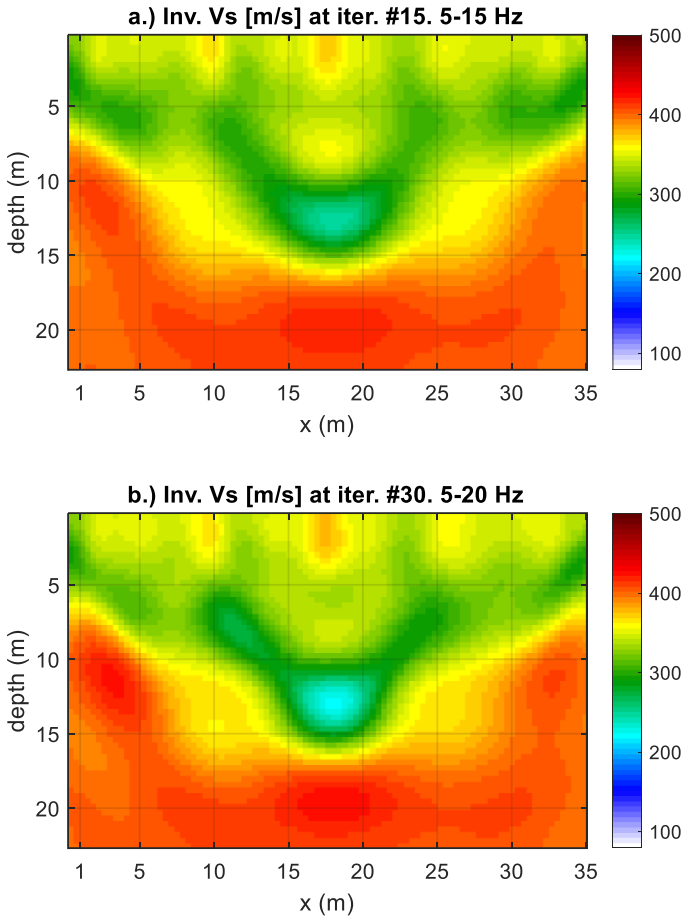

Figure 3.5. Synthetic model of S-wave velocity (m/s): (a) Inverted model at 5-15 Hz; and (b) Inverted model at 5-20 Hz (shallow void, 8 receivers).

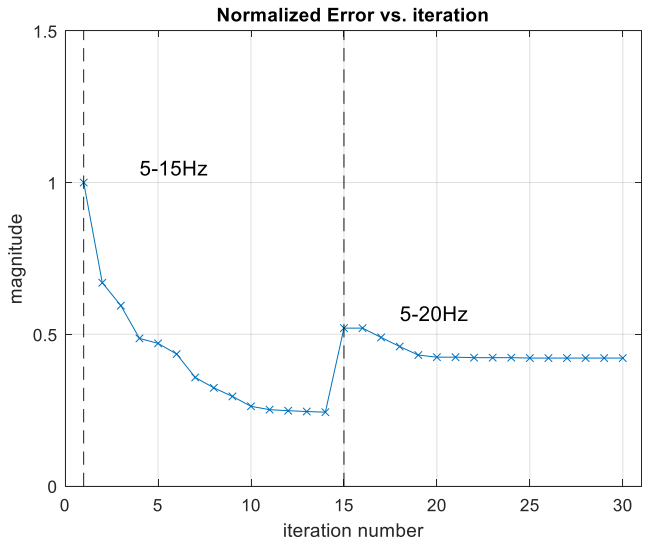

Figure 3.6. Normalized least square error (shallow void, 8 receivers)

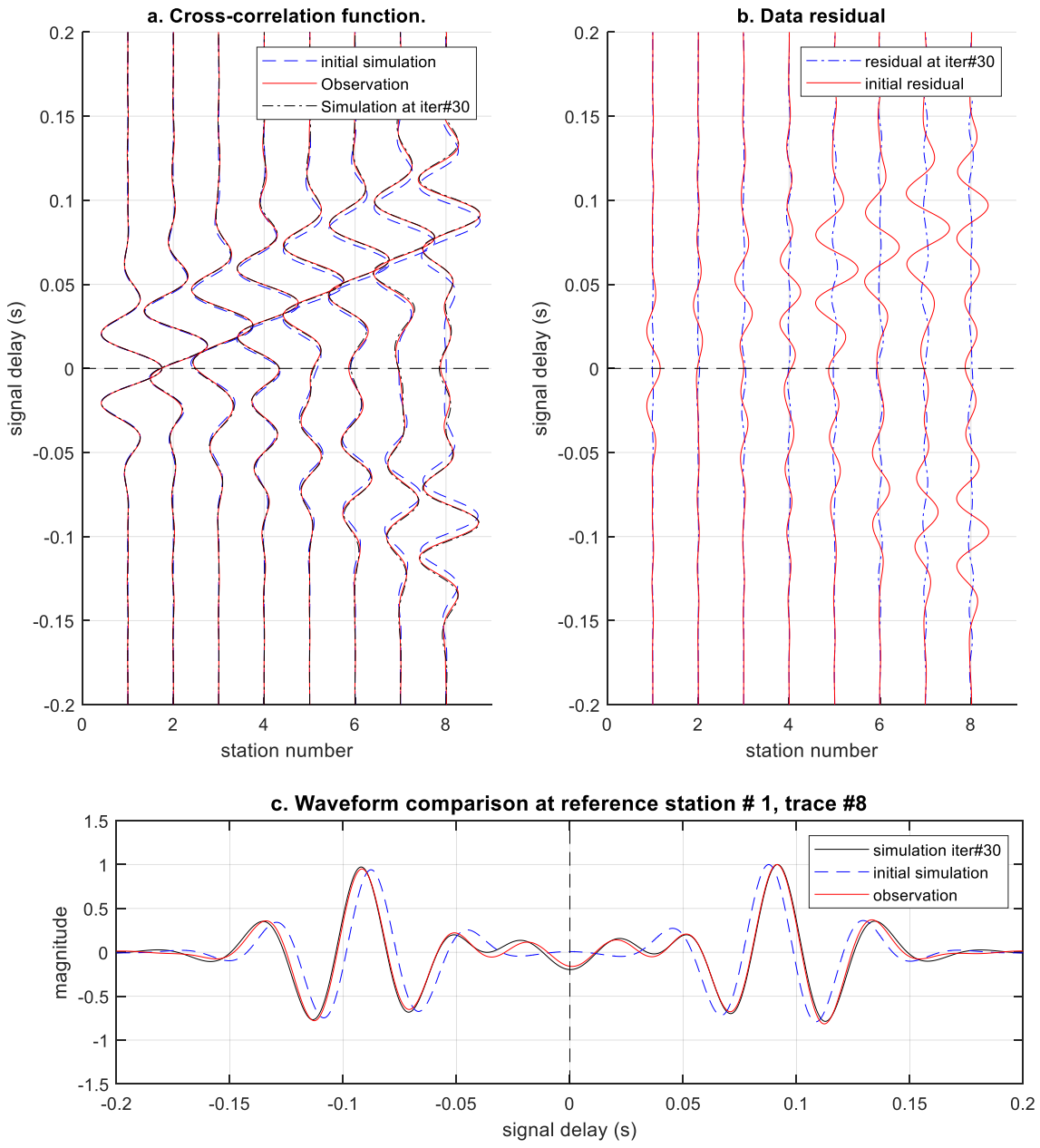

Figure 3.7. Waveform comparison at reference station #1 (shallow void, 8 receivers): (a) Comparison of the observed cross-correlation function (red) to the first simulation (blue) and the final simulation (black); (b) The initial residual (red) is compared to the final residual (blue); and (c) Waveform comparison at the reference station #1, trace #8.

3.2.3 Results for test configuration 2 (12 receivers)

The inversion analysis was then conducted with the test configuration of 12 receivers (Figure 3.3) to assess the result improvement, particularly for velocity profile in the void region. Similar to the analysis of test configuration 1, the inversion began with the same 1D linearly increasing velocity profile. Two inversion runs were conducted with the first run for the lower frequency (5-15 Hz) data on the initial model, and the second run for higher frequency (5-20 Hz) data using the result of the first run as input model.

The inverted Vs profiles of the first and second runs are displayed in Figure 3.8. The true features including the void and layers are clearly recovered after the first run (Figure 3.8a). The second run with higher frequency data up to 20 Hz improved the inverted model, particularly around the void region (Figure 3.8b). The inverted Vs at the void center is about 150 m/s, which is improved comparing the test configuration 1, but still high for voids.

Normalized least-squares error of the two inversion runs is shown in Figure 3.9, where the error reduced from 1.0 at the first iteration to about 0.25 at the end of the first run (iteration #15), and to 0.35 at the end of the second run (iteration #30). Waveform and residual comparisons are displayed in Figure 3.10. The inversion has drastically improved the waveform fitting, especially at far-field traces.

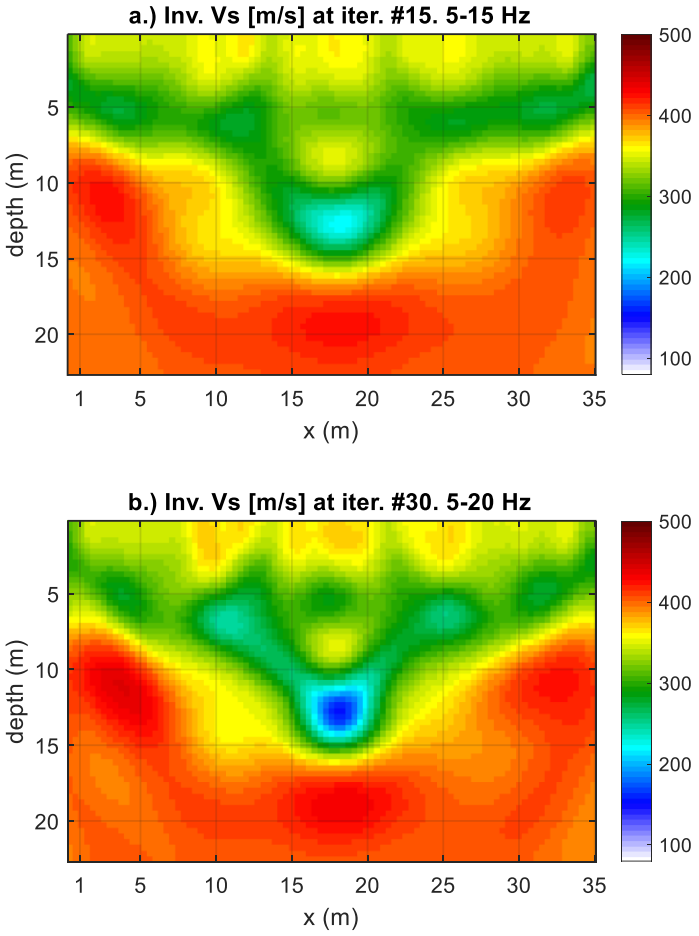

Figure 3.8. Synthetic model of S-wave velocity (m/s): (a) Inverted model at 5-15 Hz; and (b) Inverted model at 5-20 Hz (shallow void, 12 receivers).

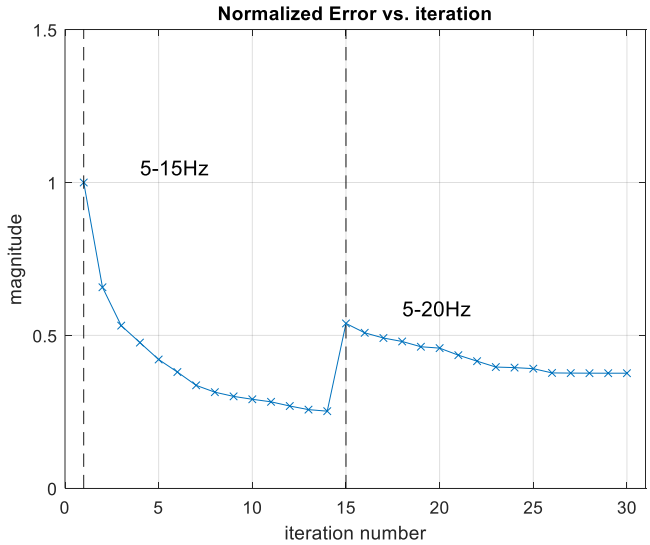

Figure 3.9. Normalized least square error (shallow void, 12 receivers)

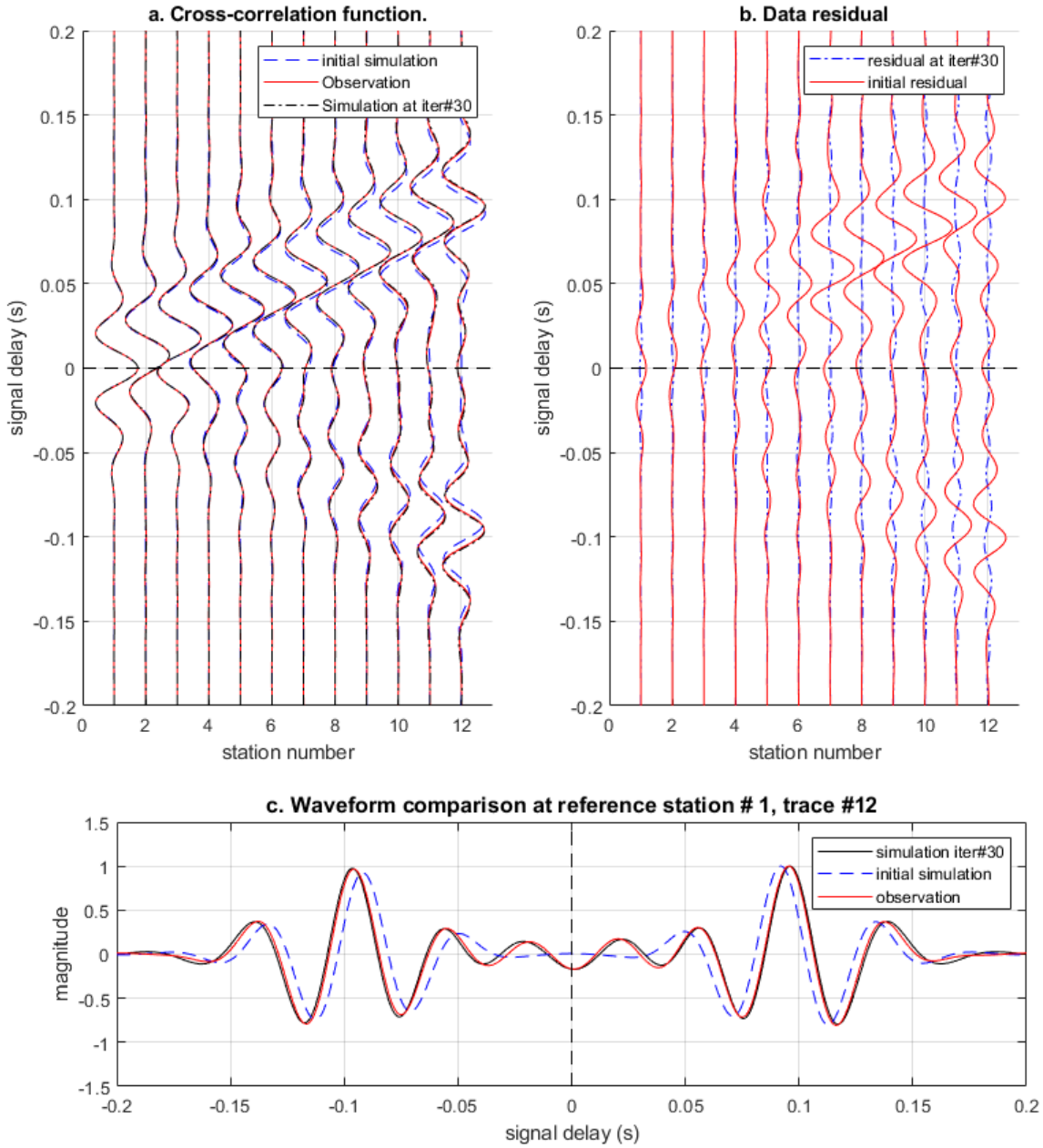

Figure 3.10. Waveform comparison at the reference station #1 (shallow void, 12 receivers): (a) Comparison of the observed cross-correlation function (red) to the first simulation (blue) and the thirtieth simulation (black); (b) The initial residual (red) is compared to the final residual (blue); and (c) Waveform comparison at the reference station #1, trace #12.

3.2.4 Results for test configuration 3 (24 receivers)

Finally, the inversion analysis was performed on the dense test configuration of 24 receivers (Figure 3.4). Similar to the previous two cases, the inversion began on the same initial model with two runs at 5-15 Hz and 5-20 Hz. The inverted Vs profiles are displayed in Figure 3.11. As expected, the layers and void location were correctly characterized in the first run (Figure 3.11a). The depth and size of the void are well recovered in the second run (Figure 3.11b). The inverted Vs at the void center is about 80 m/s (265 ft/s).

Normalized least-squares error for all iterations of the two inversion runs is shown in Figure 3.12. The error reduced from 1.0 at the start of the first iteration to less than 0.25 at the end (iteration #30). Waveform and residual comparisons are displayed in Figure 3.13. The inversion has drastically improved the waveform fitting, especially at far-field traces.

In summary, the 2D ANT algorithm is able to match the observed and simulated waveform cross-correlations well for all test configurations. From the inverted Vs profiles (Figure 3.5, Figure 3.8, Figure 3.11) of the three tests, the increasing of receiver density has evidently improved the accuracy and resolution of the inverted results. It is suggested that the receiver spacing of 5 ft will be used for field experiment to image shallow voids and characterize the subsurface down to 60 ft in depth.

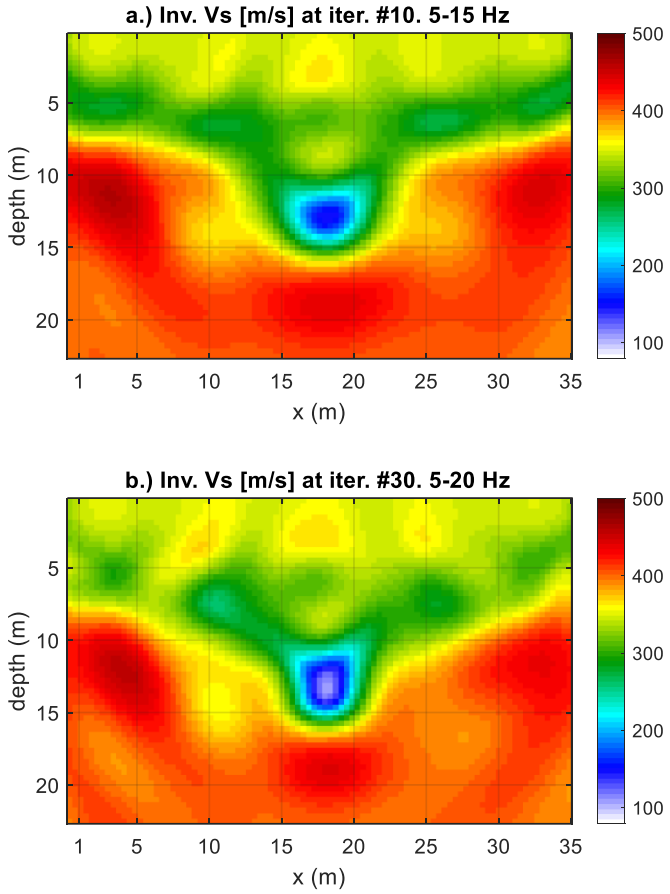

Figure 3.11. Synthetic model of S-wave velocity (m/s): (a) Inverted model at 5-15 Hz; and (b) Inverted model at 5-20 Hz (shallow void, 24 receivers).

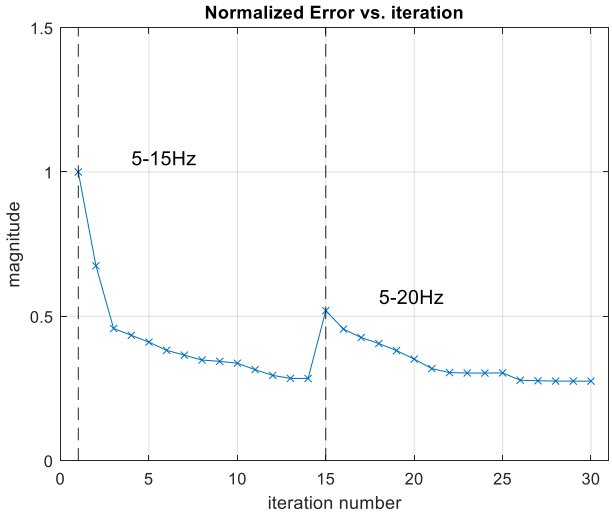

Figure 3.12. Normalized least square error (shallow void, 24 receivers)

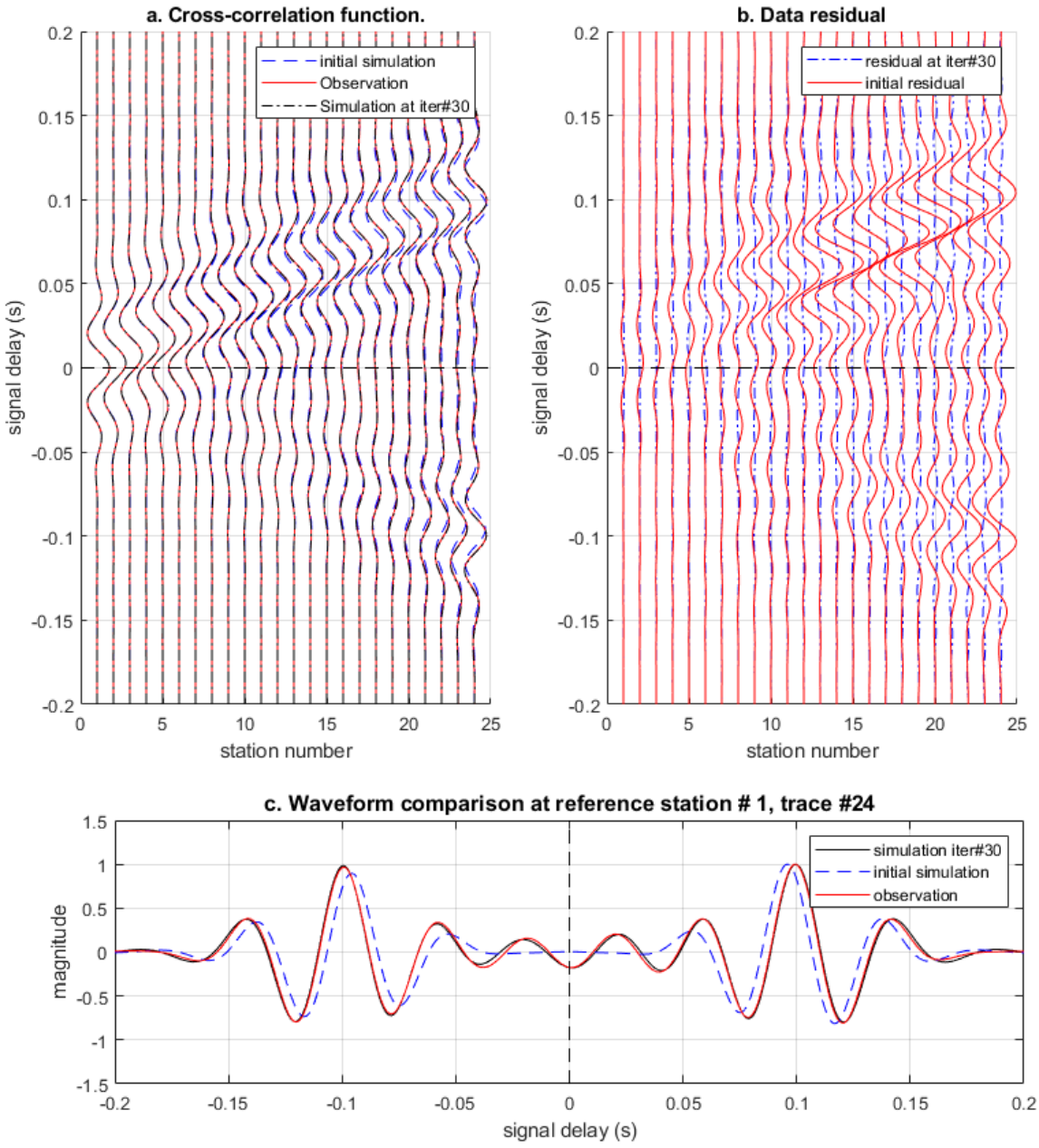

Figure 3.13. Waveform comparison at the reference station #1 (shallow void, 24 receivers): (a) Comparison of the observed cross-correlation function (red) to the first simulation (blue) and the thirtieth simulation (black); (b) The initial residual (red) is compared to the final residual (blue); and (c) Waveform comparison at the reference station #1, trace #24.

3.3 Large deep void (30-ft diameter at 80-ft depth)

3.3.1 Test configuration

With the successful recovery of a small shallow void, the developed 2D ANT algorithm was then tested on a synthetic model consisting of variable layers and a large deep void. The model domain of 75 m × 45 m (250 ft × 150 ft) (length × depth) consists of three layers, with Vs of 350 m/s, 300 m/s, and 400 m/s from the top to the bottom, respectively (Figure 3.14a). Poisson's ratio of 0.33 was assumed for the entire medium to calculate Vp (Figure 3.14b). The void is 9 m (30 ft) diameter with Vs = 0 m/s; Vp = 300 m/s (air filled void) and located at 24 m (80 ft, about three void diameters) below the ground surface.

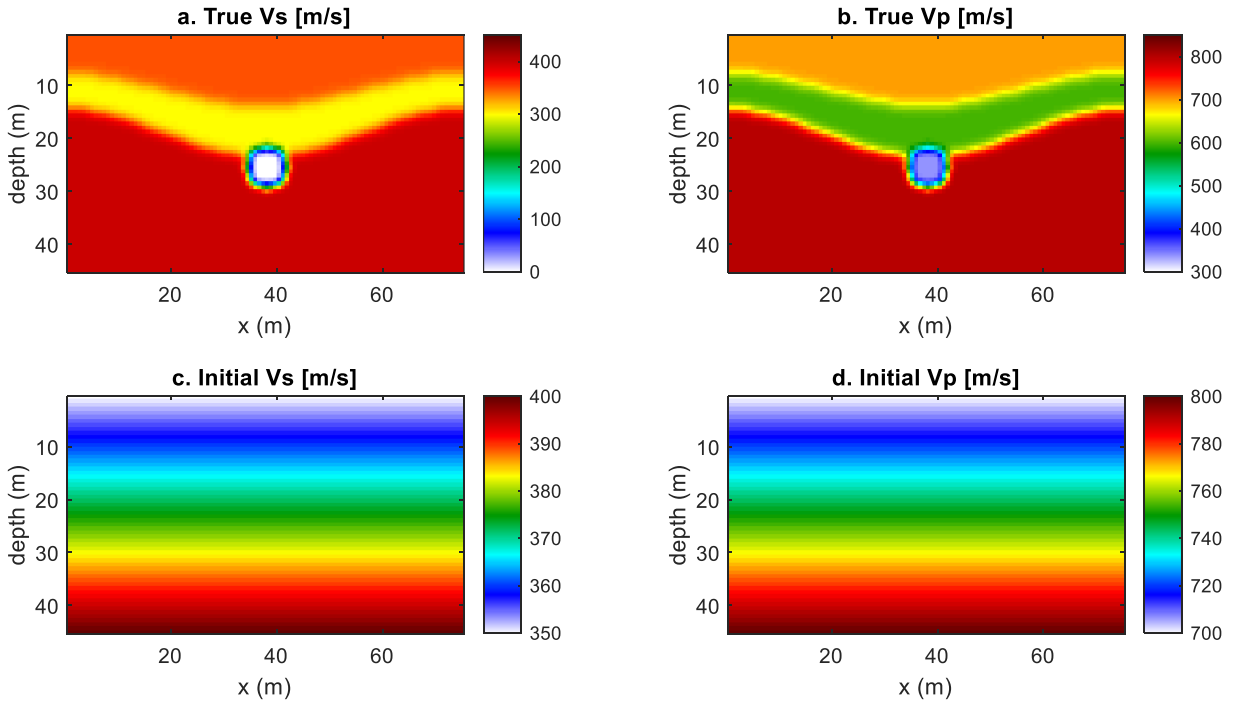

Figure 3.14. Synthetic model with a deep void of 9-m diameter at 24-m depth

The initial model used in the analyses is a 1D velocity profile that linearly increased with depth with a Vs value (Figure 3.14c) of 350 m/s on the free surface to 400 m/s at the bottom, and Vp (Figure 3.14d) is twice that of Vs. This model was tested with four configurations: 8 receivers at 9.0-m (30-ft) spacing (Figure 3.15), 12 receivers at 6.0-m (20-ft) spacing (Figure 3.16), 24 receivers at 3.0-m (10-ft) spacing (Figure 3.17), and 48 receivers at 1.5-m (5-ft) spacing (Figure 3.18). Note that all the geophone spacings used in the analysis are no more than the void diameter. Similar to the previous small shallow void example, each configuration was tested with two inversion runs with frequency ranges of 0-15 Hz and 0-25 Hz, respectively. Each run stopped after 15 iterations.

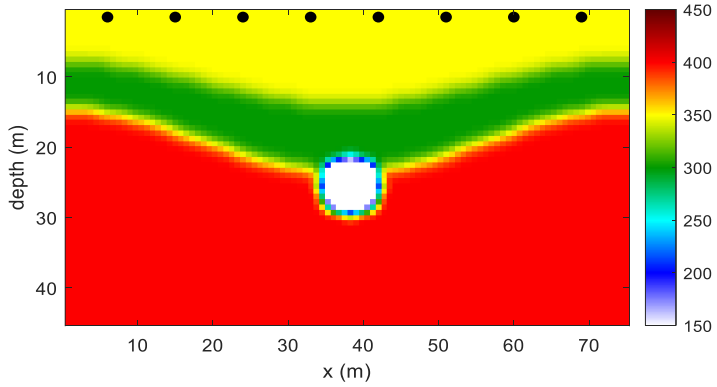

Figure 3.15. Test configuration 1: 8 receivers (black dots) at 9.0-m spacing.

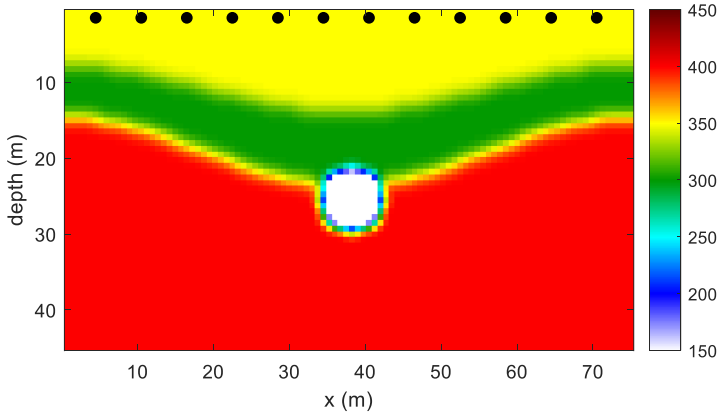

Figure 3.16. Test configuration 2: 12 receivers (black dots) at 6.0-m spacing.

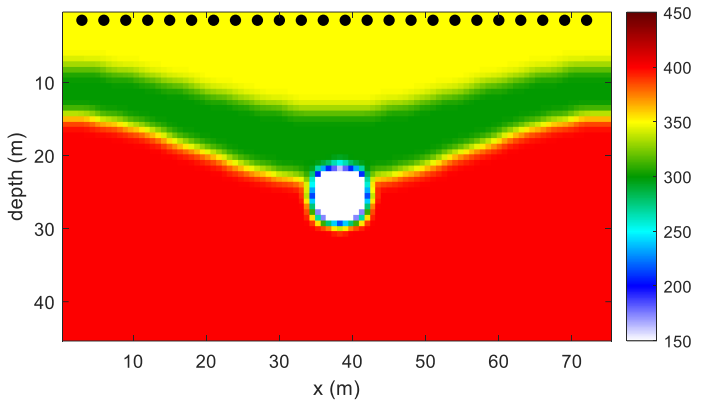

Figure 3.17. Test configuration 3: 24 receivers (black dots) at 3.0-m spacing.

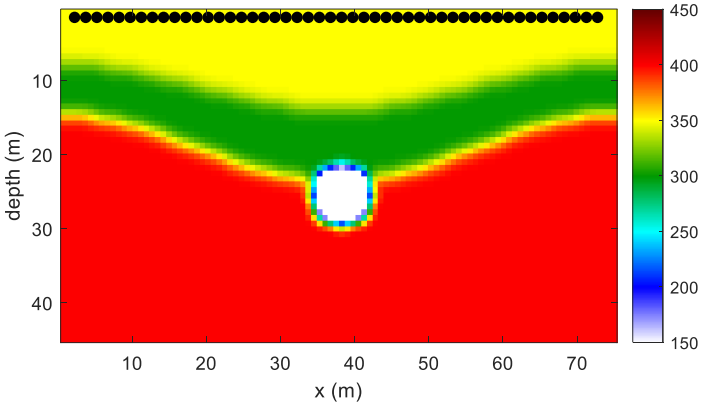

Figure 3.18. Test configuration 3: 48 receivers (black dots) at 1.5-m spacing.

3.3.2 Results for test configuration 1 (8 receivers)

The inversion analysis was first carried out for the least dense configuration of 8 receivers. Two inversion runs were again conducted with the first run for the low frequency range (0-15 Hz) data on the initial model, and the second run for higher frequency range (0-25 Hz) data using the result of the first run as input. The inverted Vs profiles of the two runs are displayed in Figure 3.19. The void geometry and position were vaguely characterized after two runs, suggesting that the spatial sampling of the wavefield was inadequate. The Vs value at the center of the void is 270 m/s after two runs (Figure 3.19b). Evidently, the 9.0-m (30-ft) receiver spacing is too coarse for accurate characterization of the layers and the void

Normalized least-squares error for all iterations of the two inversion runs are shown in Figure 3.20, where the error reduced from 1.0 at the onset of the first iteration to about 0.2 at the final iteration (iteration #15) of the first run, and to 0.3 in the second run. Waveform and residual comparisons are displayed in Figure 3.21. Considerable waveform residual is noticed after 30 iterations.

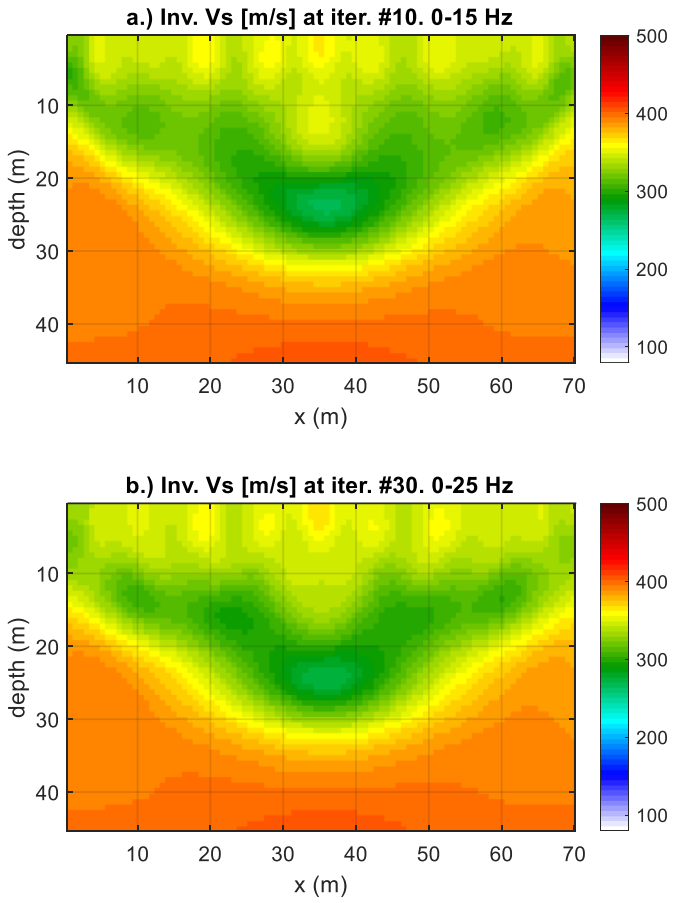

Figure 3.19. Synthetic model of S-wave velocity (m/s): (a) Inverted model at 0-15 Hz; and (b) Inverted model at 0-25 Hz (deep void, 8 receivers).

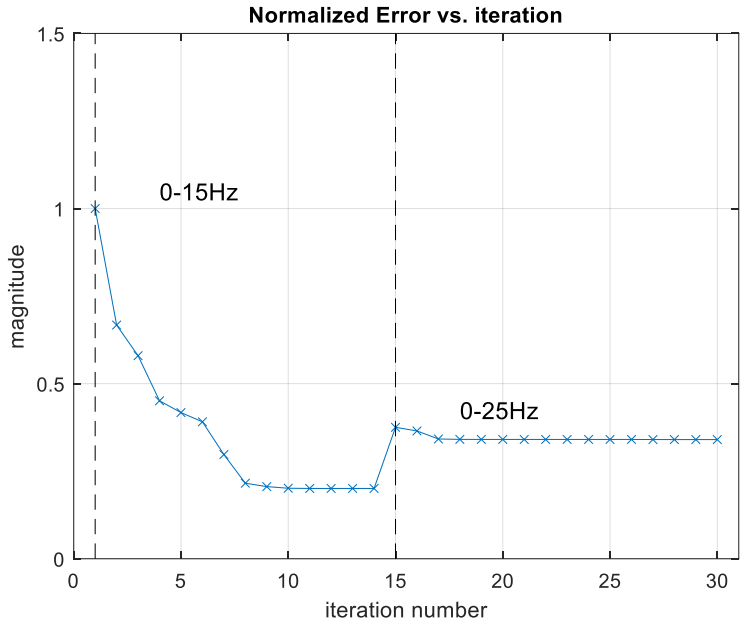

Figure 3.20. Normalized least square error (deep void, 8 receivers)

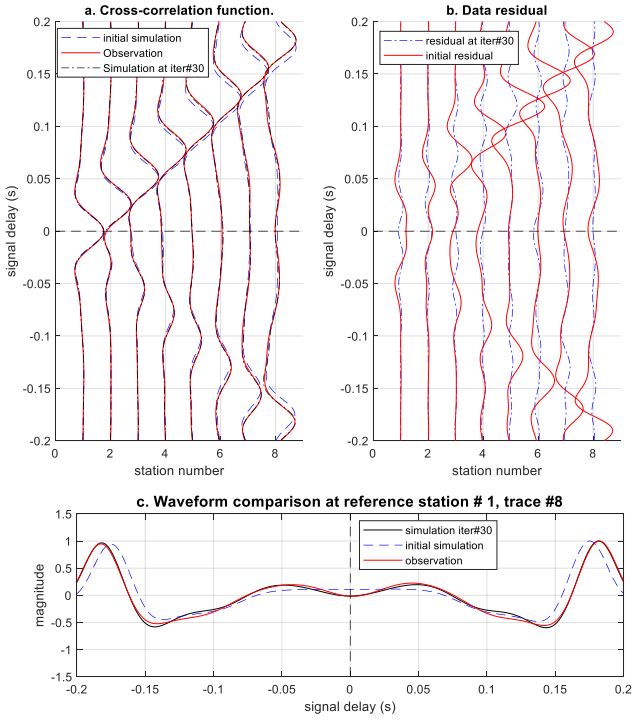

Figure 3.21. Waveform comparison at the reference station #1 (deep void, 8 receivers): (a) Comparison of the observed cross-correlation function (red) to the first simulation (blue) and the thirtieth simulation (black); (b) The initial residual (red) is compared to the final residual (blue); and (c) Waveform comparison at the reference station #1, trace #8

3.3.3 Results for test configuration 2 (12 receivers)

We then tried with a test configuration of 12 receivers (Figure 3.16) to assess result improvement, particularly for velocity profile in the void region. The inverted Vs profiles obtained at iteration #15 and #30 are displayed in Figure 3.22. Compared with the previous case of 8 receivers, the true model features including the void and layers, along with velocity values are generally recovered after the first run (Figure 3.22a). The second run with higher frequency data up to 25 Hz improved the inverted model from the first run, particularly around the void region (Figure 3.22b). The inverted Vs at the center of the void is about 200 m/s, still too high for voids.

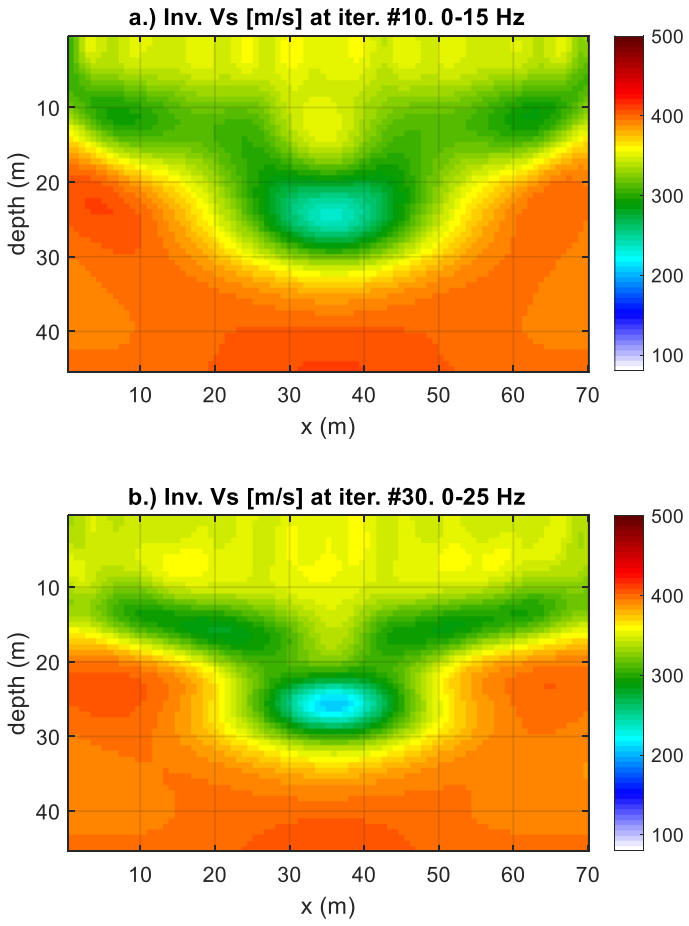

Figure 3.22. Synthetic model of S-wave velocity (m/s): (a) Inverted model at 0-15 Hz by iteration #15; (b) Inverted model at 0-25 Hz by iteration #30 (deep void, 12 receivers).

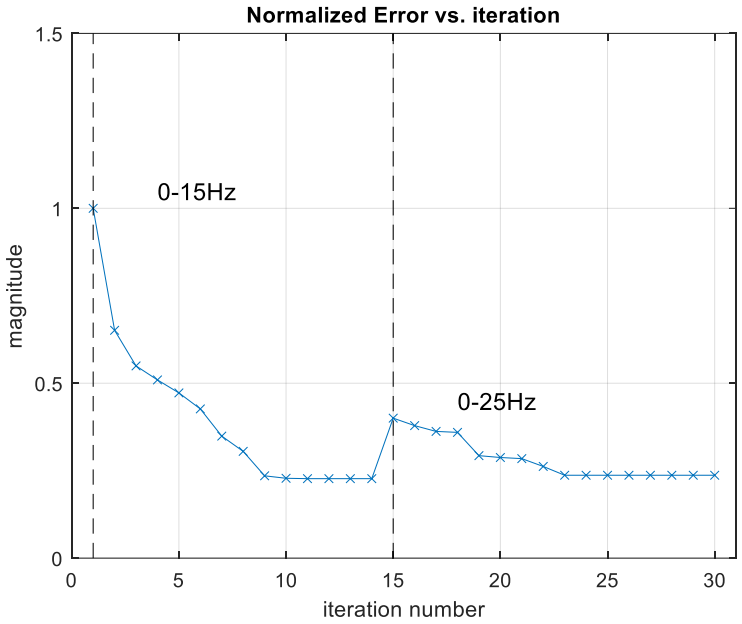

Figure 3.23. Normalized least square error (deep void, 12 receivers)

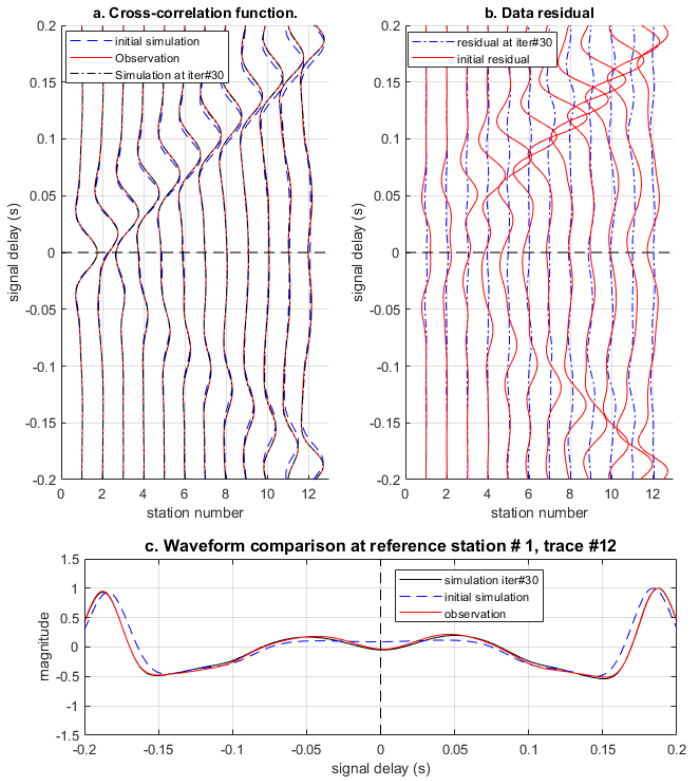

Figure 3.24. Waveform comparison at the reference station #1 (deep void, 12 receivers): (a) Comparison of the observed cross-correlation function (red) to the first simulation (blue) and the thirtieth simulation (black); (b) The initial residual (red) is compared to the final residual (blue); and (c) Waveform comparison at the reference station #1, trace #12.

Normalized least-squares error for all iterations of the two inversion runs are shown in Figure 3.23, where the error reduced from 1.0 at the onset of the first iteration to about 0.25 at the final iteration (iteration #15) of the first run, and 0.25 on the second run. Waveform and residual comparisons are displayed in Figure 3.24. The inversion with 6.0-m (20-ft) geophone spacing has improved the waveform fitting, especially at far wavefield traces.

3.3.4 Results for test configuration 3 (24 receivers)

Next, the inversion was conducted on a dense test configuration of 24 receiver stations (Figure 3.17) to identify any possible improvement over the previous two test configurations of 8 and 12 receivers. The inverted Vs profiles obtained at iteration #15 and #30 are displayed in Figure 3.25. As expected from the previous two analyses, the void geometry and position were correctly characterized after the first run (Figure 3.25a). The Vs value at the void center is 150 m/s after two runs (Figure 3.25b).

Normalized least-squares error for all iterations of the two inversion runs is shown in Figure 3.26. The error reduced from 1.0 at the start of the first iteration to about 0.20 at the end of the analysis (iteration #30). Waveform and residual comparisons are displayed in Figure 3.26. The inversion has drastically improved the waveform fitting, especially at far wavefield traces. Only trivial waveform residual can be identified after thirty iterations, suggesting that 3.0 m (10 ft) is an acceptable geophone spacing.

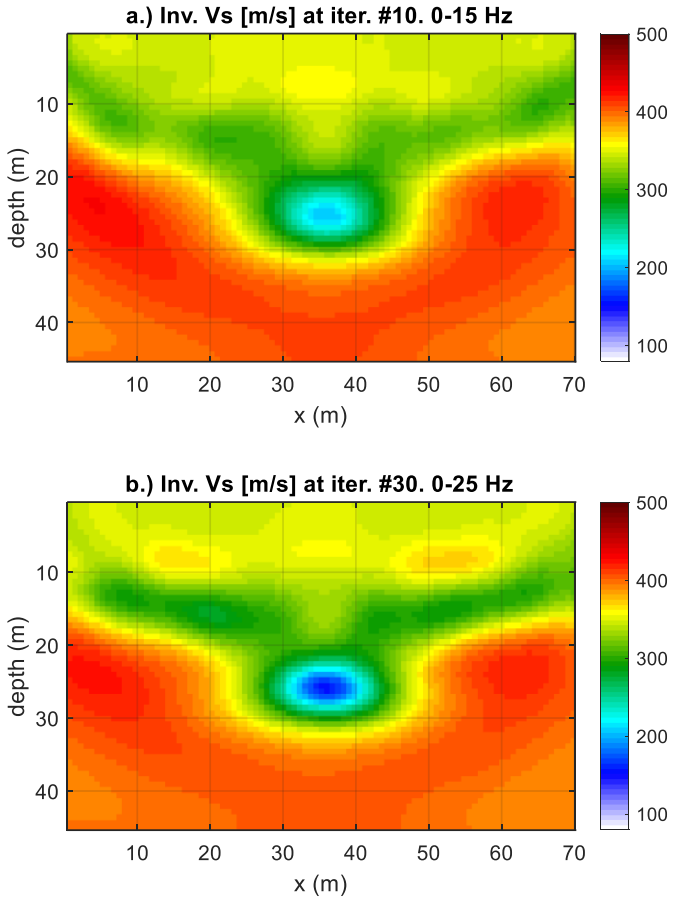

Figure 3.25. Synthetic model of S-wave velocity (m/s): (a) Inverted model at 0-15 Hz by iteration #15; and (b) Inverted model at 0-25 Hz by iteration #30 (deep void, 24 receivers).

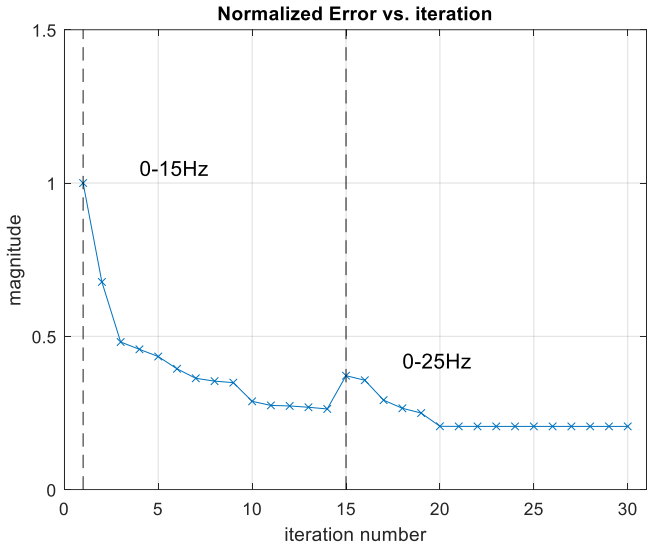

Figure 3.26. Normalized least square error (deep void, 24 receivers)

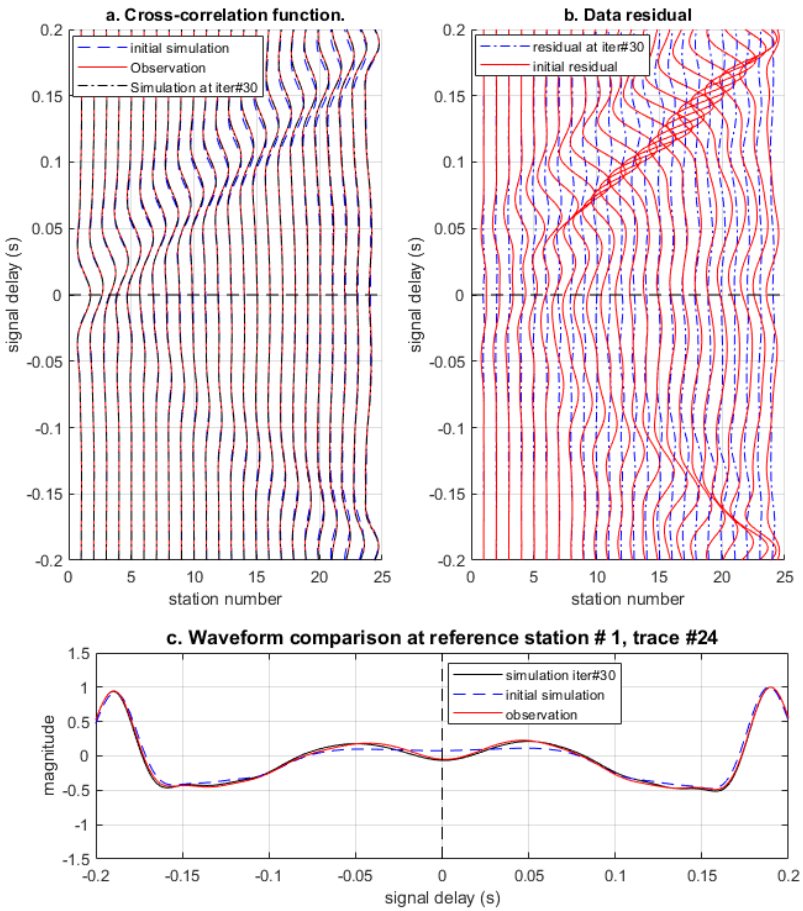

Figure 3.27. Waveform comparison at the reference station #1 (deep void, 24 receivers): (a) Comparison of the observed cross-correlation function (red) to the first simulation (blue) and the thirtieth simulation (black); (b) The initial residual (red) is compared to the final residual (blue); and (c) Waveform comparison at the reference station #1, trace #24.

3.3.5 Results for test configuration 4 (48 receivers)

Finally, the inversion was done on the densest test configuration of 48 receiver stations (Figure 3.18). Using the same inversion parameter settings and initial model, the inverted Vs profiles obtained at iteration #15 and #30 are displayed in Figure 3.28. Similar to what observed from the previous test of 3.0-m (10-ft) receiver spacing, the void geometry and position were correctly characterized after the first run (Figure 3.28a). The Vs value at the center of the void is about 80 m/s after two runs (Figure 3.25b), which is more accurate than the result of the test with 3.0-m (10-ft) receiver spacing.

Normalized least-squares error for all iterations of the two inversion runs are shown in Figure 3.29. The error reduced from 1.0 at the start of the first iteration to less than 0.20 at the end of the analysis (iteration #30). Waveform and residual comparisons are displayed in Figure 3.30. Hardly the waveform residual can be noticed after thirty iterations, suggesting that the configuration using 1.5-m (5-ft) geophone spacing is the optimal one among the four tested configurations.

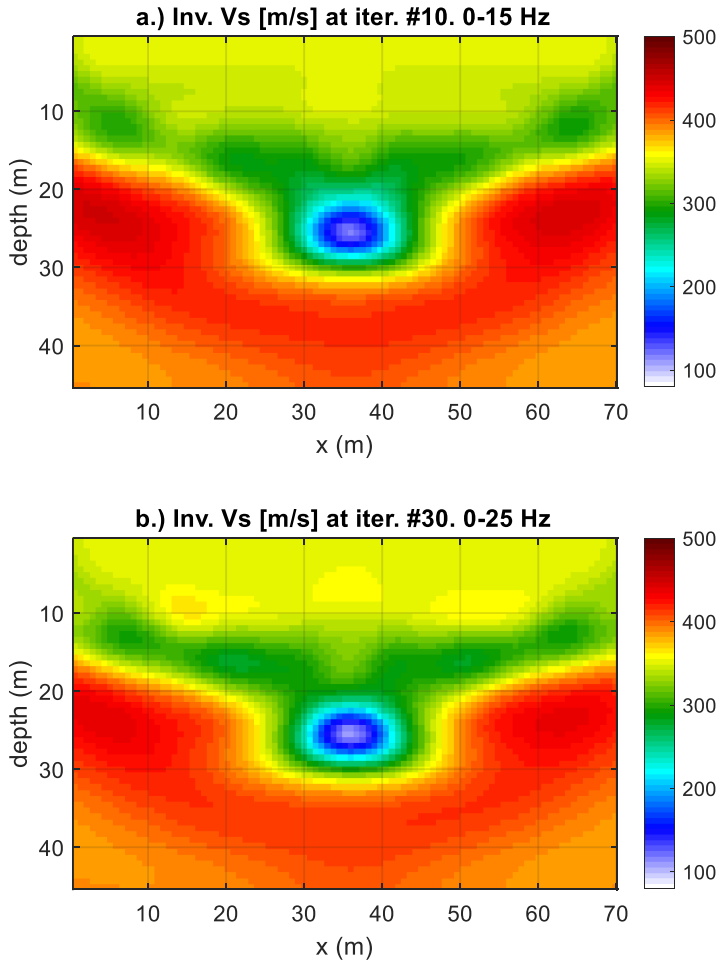

Figure 3.28. Synthetic model of S-wave velocity (m/s): (a) Inverted model at 0-15 Hz by iteration #15; and (b) Inverted model at 0-25 Hz by iteration #30 (deep void, 48 receivers).

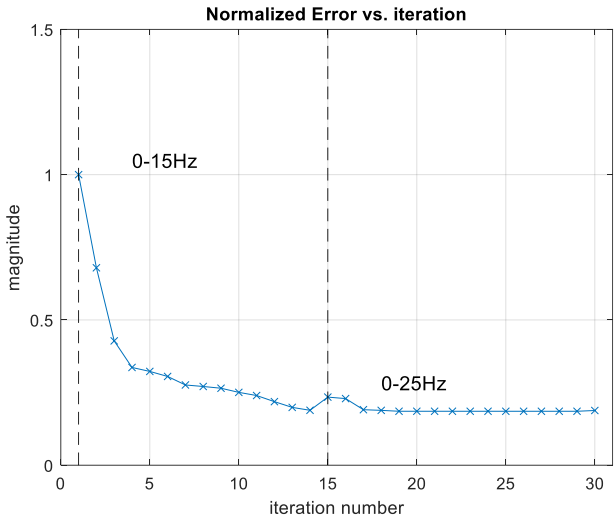

Figure 3.29. Normalized least square error (deep void, 48 receivers)

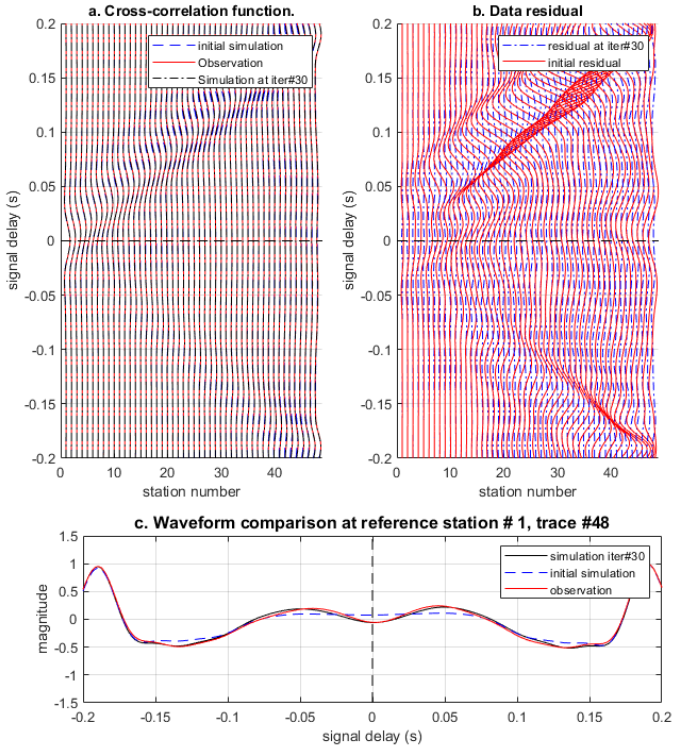

Figure 3.30. Waveform comparison at the reference station #1 (deep void, 48 receivers): (a) Comparison of the observed cross-correlation function (red) to the first simulation (blue) and the thirtieth simulation (black); (b) The initial residual (red) is compared to the final residual (blue); and (c) Waveform comparison at the reference station #1, trace #48.

In summary, tested on deep void model, the 2D ANT algorithm is able to match the observed and simulated waveform cross-correlations for all test configurations. From the inverted Vs profiles (Figure 3.5, 3.22, 3.25, 3.28) of the four tests, the increasing of receiver density has improved the accuracy and resolution of the inverted results. It is suggested that the receiver spacing of 5 to 10 ft will be used for field experiment to image deep voids and characterize the subsurface down to 120 ft in depth.

3.4 Conclusion

An optimization of test configurations (receiver locations) has been performed using the developed 2D ANT algorithm. The goal was to find the minimum number of receivers (maximum spacing) that enabled a successful characterization of variable layers and embedded voids. Several test configurations of receivers equally placed at 1.5 m to 9 m (5 ft to 30 ft) spacing on the surface were analyzed. The configurations were tested on two synthetic models with variable soil/rock layers and embedded voids. Accuracy and resolution of inverted Vs profiles were compared between simulations to identify the optimal test configuration.

The analyses were first performed on the model with a small shallow void, 3.75-m (12.5 -ft) diameter at 12-m (40-ft) depth. Analyses of all three test configurations at 1.5-m (5-ft), 3.0-m (10-ft), and 4.5-m (15-ft) spacing were shown to successfully recover variable layers, as well as the void location. However, the inverted Vs value of the void is moving closer to its true value (0 m/s) as the receiver spacing decreases. The inverted Vs values at the void center for the three configurations are 220 m/s, 150 m/s, and 80 m/s for receiver spacing of 15 ft, 10 ft and 5 ft, respectively. The results suggested that the geophone spacing of 5 ft is the optimal spacing for shallow void imaging.

Next, the inversion analyses were performed on the model on a large deep void, 9-m (30-ft) diameter at a deeper depth of 24 m (80 ft). The 2D ANT analyses showed that all the receiver configurations can produce successful recovery of variable layers. However, only the dense test configurations with geophone spacings of 3.0m (10 ft) and 1.5m (5 ft) were able to accurately recover both the void size and position. The other configurations at 6.0-m (20-ft) and 9.0-m (30-ft) spacing vaguely showed the void location. Similar to the shallow void tests, the inverted Vs value of the void approaches to its true value (0 m/s) as the receiver spacing decreases. The inverted Vs values of the void for the four configurations are 270 m/s (30-ft spacing), 220 m/s (20-ft spacing), 150 m/s (10-ft spacing), and 80 m/s (5-ft spacing), respectively. The results suggest that the geophone spacings of 5 ft and 10 ft are acceptable. If possible, using the smaller (5-ft) receiver spacing (more geophones) would achieve higher imaging resolution.

From the results of the analyses performed in this task, 5-ft receiver spacing is recommended for field testing for both shallow and deep voids. For large (~30-ft diameter) deep voids, 10-ft receiver spacing also generates acceptable inversion results. These optimal test configurations should be used on field experiments. In term of required frequency content, noise data at 5-25 Hz is needed for accurate imaging of voids. The low-frequency components (5-10 Hz) are always available in traffic noises as the main benefit of this 2D ANT approach, recorded noise data should be checked during experiments to make sure the high frequency components (>10 Hz) are recorded for accurate characterization.

Chapter 4 – VERIFICATION OF 2D ANT METHOD ON FIED EXPERIMENTS (TASK 3)

4.1 Introduction

An advanced 2D ambient noise tomography (2D ANT) method was successfully developed in Task 1. The optimal test configurations (receiver number and spatial density) and noise characteristics (frequency content) for detection of voids at various sizes and depths by the 2D ANT were then thoroughly studied in Task 2. With the successful performance on synthetic (computational) noise data, we have subsequently tested the method on field experimental data sets to assess its performance under the real-world conditions. In this task, the method has been tested at four test sites in Florida to verify its capacity of void/anomaly detection.

The 2D ANT method was first tested at US-441 Highway in Marion County with a repaired sinkhole. Ambient traffic noise data were collected for both pre-grouting and post-grouting to assess the subsurface conditions. It was then tested at a bridge construction site in Miami for imaging a deep and large void, which was encountered during construction. The method was next tested on Wekiva Parkway SR-46 with a recently opened sinkhole. It was finally tested at Wekiva Parkway Bridge, where a void and problematic soils were encountered during construction, causing problems with driving the last pile in the group and redesign of the bridge pier. The processing of collected data at each site is documented in detail, and results are compared to the ground truth for verification of the ANT method.

4.2 US-441 Highway

The first test site was on US-441 Highway, in Marion County, Florida, USA. Seismic survey was conducted to assess a roadway segment with a repaired sinkhole (Figure 4.1). The

sinkhole caused excessive localized surface settlements in the roadway in 2011, and the roadway was remediated by compaction of filled sand and gravels. However, the subsidence had continued, suggesting that the void was not completely filled (Tran and Sperry 2018). After further evaluation, subsurface grouting was selected to remediate the roadway substructure. The 2D ANT method was applied to this site to image the pre-grouting void and assess the post-grouting subsurface.

Traffic noise (passive seismic) data sets were acquired along roadway on top of the repaired sinkhole in 2016 (pre-grouting) and 2021 (post-grouting). Data were recorded using a land-streamer of twenty-four 4.5 Hz vertical geophones at 1.5-m (5-ft) spacing for a receiver spread of 34.5 m (115 ft). The repaired sinkhole was approximately 20 m (66 ft) away from the first receiver. The active-source seismic data were also collected in 2016 at the same day with passive seismic data for comparison.

Figure 4.1. US-441 highway test site with a repaired sinkhole (pavement patched area)

4.2.1 Pre-grouting data

The pre-grouting traffic noise data were collected for five records of one-minute each. A sample record of traffic noises is displayed in Figure 4.2a, showing strong noise signals of passing-by vehicles between 5~8 s, 15~30 s, and 48~55 s. For this record, most of vehicles passed by in the direction from receiver 24 to receiver 1 (right to left).

The noise data are filtered to preserve the low frequencies (0-25 Hz), and Figure 4.2b is an example of a segment (6 to 7 s) of the traffic noise record. A series of surface wave events (blue dash lines) were induced by passing-by vehicles acting as (internal) sources within the geophone spread, suggesting that a vehicle is a moving active-source and traffic noises are indeed dominated by surface (Rayleigh) waves.

The record was divided into 0.3-second segments. The segment length of 0.3-second was selected, as it is long enough for wavefields to propagate through the entire geophone spread of 34.5 m (115 ft). A longer segment can also be used, but it potentially leads to cross-correlate wave events from multiple sources (source correlation issue). The cross-correlation function was calculated for each segment and stacked together as shown in Figure 4.2c. As highlighted with blue dash lines, Rayleigh waves are evident and have a consistent pattern of propagation in the retrieved cross-correlation function.

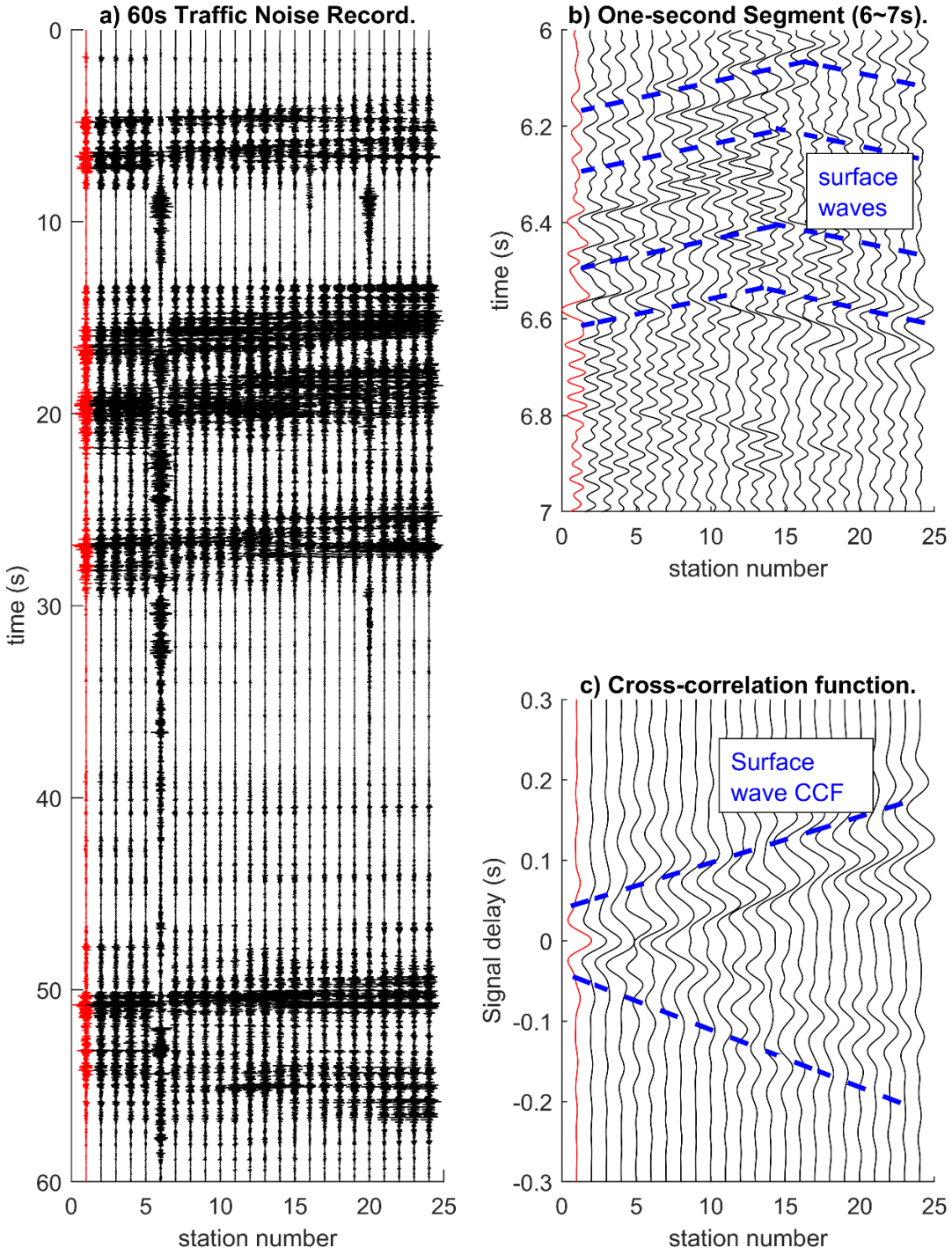

Figure 4.2: Pre-grouting US-441 highway: (a) The raw 60-s length traffic noise record; (b) A one-second (6~7 s) segment of the traffic noise record; and (c) The retrieved cross-correlation function at the reference station #1. The record on the reference station (station #1) is highlighted with red.

4.2.1.1. Source signature and distribution

The source signature and distribution are important for inversion of the cross-correlation functions. As the source spatial distribution of traffic noises is on the road surface and close to the test location, we estimate the source signature and the source power-spectrum density (PSD) for only for surface-based sources from the field data and keep them constant during inversion. The source signatures used for forward simulation are estimated from the field noise autocorrelation. Assuming a source time function (STF) $w(t)$ for a reference station, then the noise autocorrelation at the reference station is equivalent to the autocorrelation of $w(t)$. The goal is to find $w(t)$ having its autocorrelation similar to the noise autocorrelation. For a reference station i, we define an error E_{w_i} consisting of a L-2 norm term of the difference between the autocorrelation of field noise $C_i(t)$ and the autocorrelation of $w(t)$. A L-1 norm term of regularization is added to E_{w_i}.

$$E_{w_i} = \left\| \mathrm{Auto}\big(w(t)\big) - C_i(t) \right\|_{L_2} + \alpha \| w(t) \|_{L_1}, \qquad \mathrm{Auto}\big(w(t)\big) = \int w(t+\tau) w(t) dt. \tag{21}$$

Where $C_i(t)$ is the noise autocorrelation at reference station i. Coefficient α is a regularization factor, which we set to 2.0 in this study.

The minimization of the error in eq. (21) is solved iteratively. For each reference station, a Ricker wavelet is used as the initial guess, and the estimated source signature is obtained when the change of error from two consecutive iterations is below a fixed threshold (e.g., 0.1%, in this example). An example of source estimation for reference station #1 is presented in Figure 4.3. A Ricker wavelet (Figure 4.3a) is input as the initial guess. The autocorrelations of field noise and estimated STF in terms of waveform (Figure 4.3b) and power spectrum (Figure 4.3c) are similar.

The source estimation is performed individually for 24 reference stations and the estimated source signatures are shown in Figure 4.3d. They are consistent in waveform, and thus used for the forward simulation during inversion.

The power-spectrum density (PSD) function was estimated by the time-reverse imaging method (Artman et al., 2010) and shown Figure 4.4 for the source distribution along the ground surface (no embedded source for traffic noise). The PSD represents the equivalent source energy along the test line (both nearby and far-field sources). It reveals the comparable source energy along the test line with the largest energy at distance of 10 m (33 ft). This PSD function is used for simulation of the estimated cross-correlations for inversion.

4.2.1.2. Inversion Analysis

For inversion, the model is discretized into a 100 × 60 grid of 0.375-m (1.25-ft) spacing in the x- and z-directions, respectively. The grid spacing is selected as a quarter of the receiver spacing to conveniently assign receivers to numerical nodes. The receiver spread of 34.5 m (115 ft) is assigned on the free surface, with the first receiver at $x = 0$ m and the last receiver at $x =$ 34.5 m (115 ft). To maintain 10 grid points per wavelength, the selected grid spacing allows wave simulation up to 30 Hz.

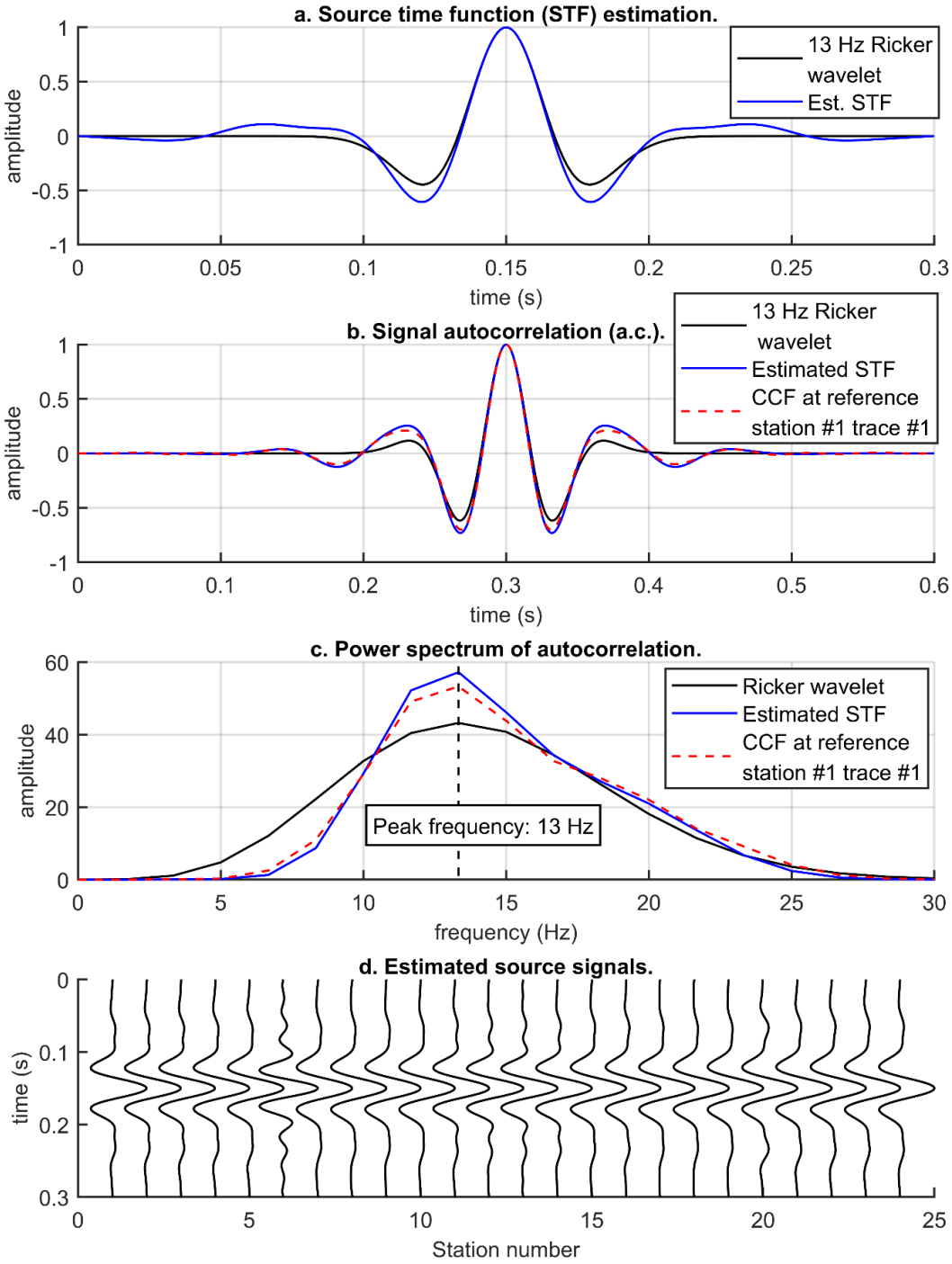

Figure 4.3. Source time function (STF) estimation: (a) Initial guess (black) and estimated STF (blue); (b) Autocorrelations of estimated STF (blue), field noise (red), and Ricker wavelet (black); (c) Power spectrum of the autocorrelations of estimated STF (blue), field noise (red), and Ricker wavelet (black); and (d) Estimated STFs for all 24 reference stations.

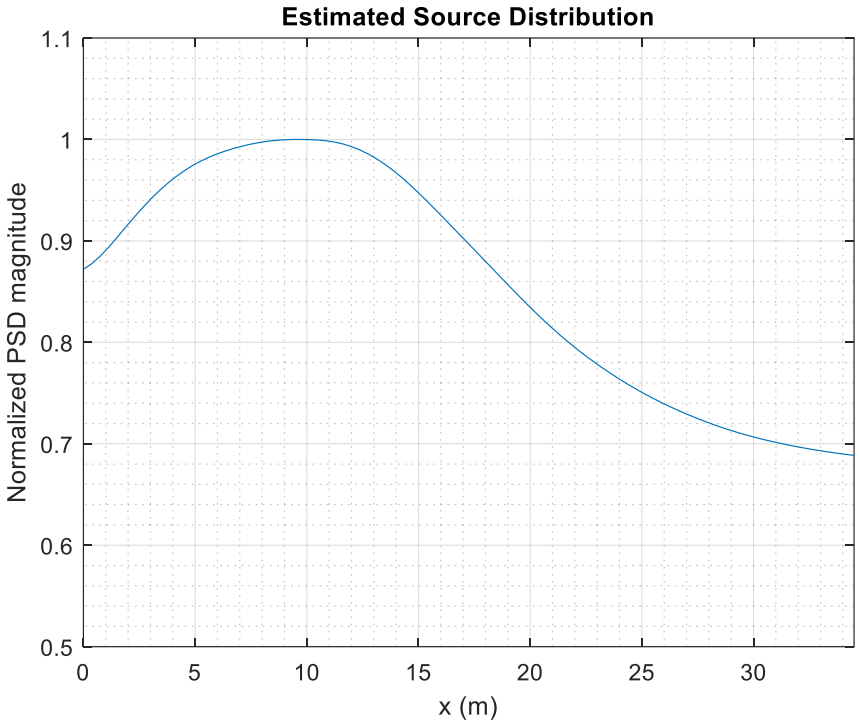

Figure 4.4. Pre-grouting US-441 highway: normalized estimated source power spectrum distribution (PSD) function of the field traffic noise cross-correlation function. The first station (station #1) and the last station (station #24) are located at 0 m and 34.5 m, respectively.

The initial Vs model was established via a dispersion analysis of passive-source surface waves (noise data). The dispersion spectrum image (Figure 4.5a) was created following the method developed by Park et al. (2004). Rayleigh wave phase velocity (V_R) is increasing from 250 m/s to 500 m/s (833 ft/s to 1667 ft/s) as the frequency decreasing from 15 Hz to 5 Hz, which implies that Vs profile generally increases with depth. For comparison, the active-source dispersion spectrum at the same site (Tran and Sperry, 2018) is shown Figure 4.5b. V_R between 10 Hz and 20 Hz have similar trends in both spectra. Both results show V_R slightly above 250 m/s (833 ft/s) at 15 Hz and increase with decreasing frequency. The active-source spectrum has low wave energy below 10 Hz, whereas the passive source spectrum shows strong wave energy at 5 Hz to 10 Hz, which is the advantage of using ambient noise data rich in low frequency components for deep investigations.

The fundamental mode (m0) shows a nearly constant V_R = 250 m/s (830 ft/s) for the frequencies greater than 15 Hz, which suggests that Vs is about 250 m/s for the top layer. The initial Vs model (Figure 4.6a) is set to be lateral homogeneous with values increasing linearly with depth from 250 m/s to 500 m/s (833 ft/s to 1667 ft/s). The initial Vp model is created from the initial Vs model and a characteristic Poisson's ratio of 1/3.

As the consistent cross-correlation signals are available at 5 Hz to 20 Hz, two inversion runs were conducted with frequency bandwidths of 5-15 Hz and 5-20 Hz. The first run started with the lower frequency bandwidth on the initial model (Figure 4.6a), and the second run continued on the first run result as the input model. Each run stopped at a preset number of iterations (15), and it took about one hour on a desktop computer (8 cores of 3.7 GHz processor and 64 GB RAM) for both runs.

The inverted Vs profiles of the two runs are shown in Figure 4.6. The final result of the second run (Figure 4.6c) clearly shows a low-velocity anomaly at 12 m (40 ft) depth. The anomaly center is at distance x= 20 m (67 ft), which is the same as the true location of the repaired sinkhole. The inverted Vs at the anomaly center is about 150 m/s (500 ft/s), which is lower than the values of the surrounding area [>300 m/s (1000 ft/s)], suggesting that the void was not completely filled and compacted. This was supported by the subsequent subsidence after the pre-grouting testing.

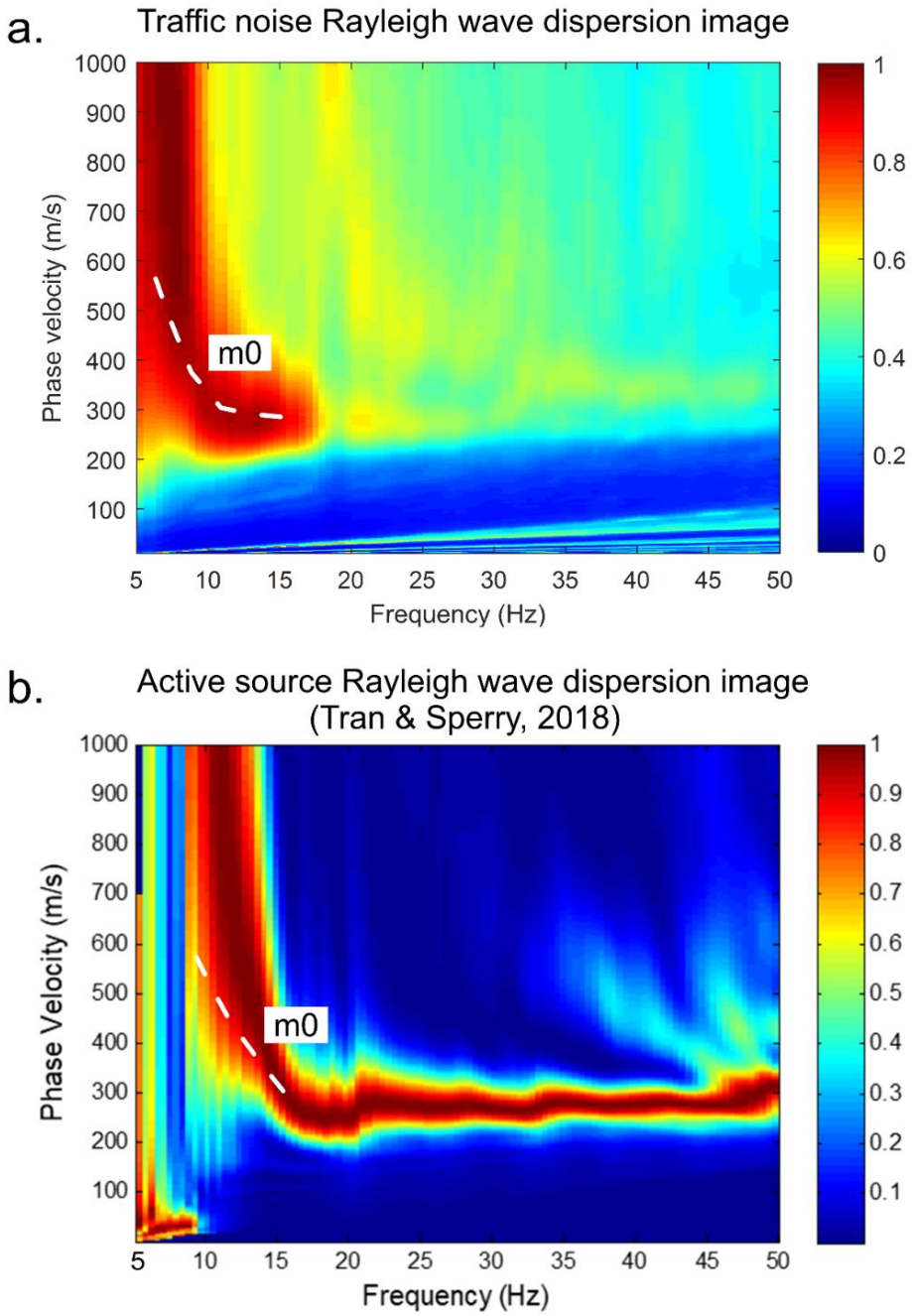

Figure 4.5. Pre-grouting US-441 highway: Rayleigh wave dispersion analysis: (a) Passive source Rayleigh wave dispersion analysis of the traffic noise; and (b) Active source Rayleigh wave dispersion analysis, modified from Tran & Sperry, 2018. The fundamental mode (m0) is marked with white dash lines up to 15 Hz.

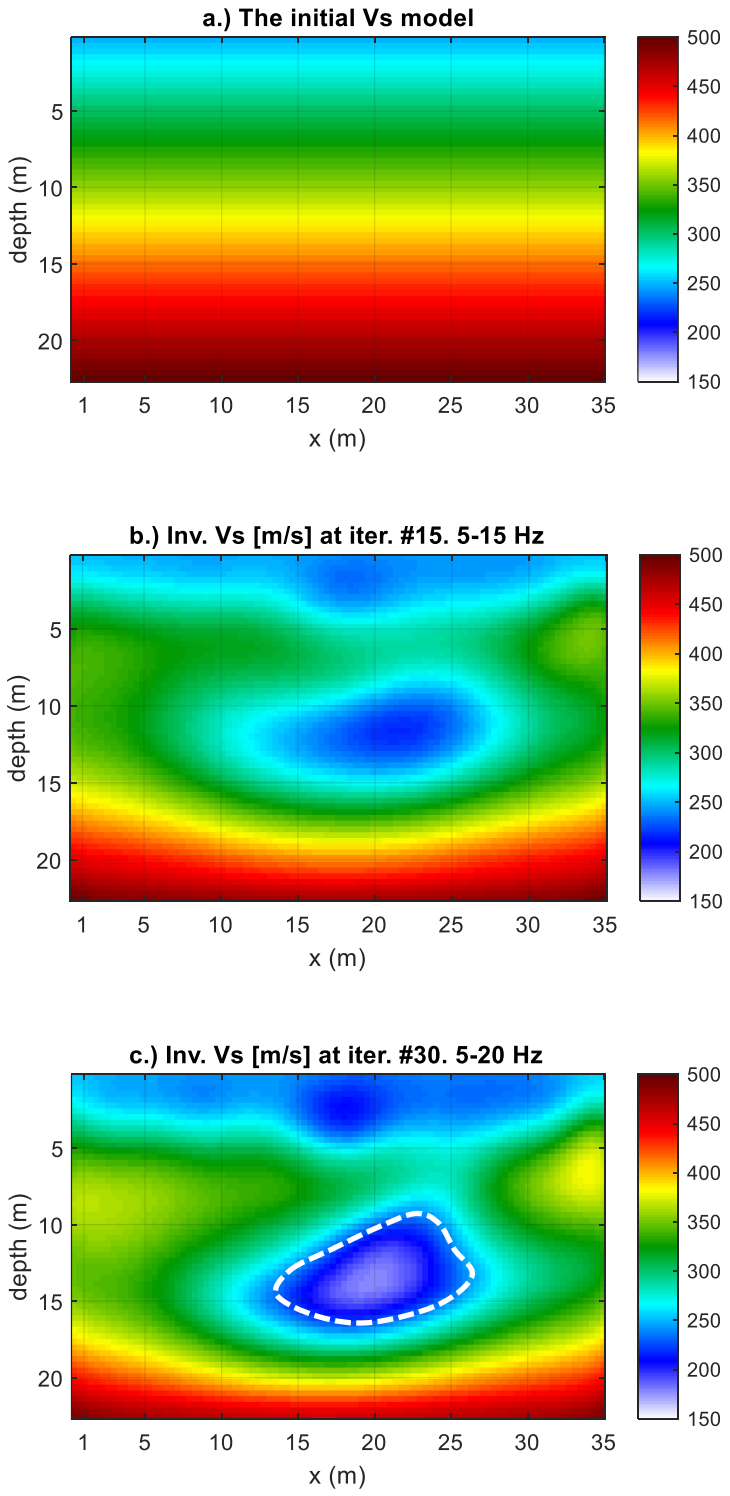

Figure 4.6. Pre-grouting US-441 highway: (a) Initial Vs model; (b) Inverted Vs after 15 iterations (the first run); and (c) Inverted Vs after 30 iterations (the second run). The dash white curve denotes the esimated void location.

The waveform comparison of the observed and simulated cross-correlation functions is shown Figure 4.7a. The red curves are the observed cross-correlation function of field traffic noise at 5-20 Hz. The blue and black dash curves are the initial and the final simulated cross-correlation functions, respectively. At large-offset channels (16 to 24), the improvement of data fitting during inversion is evident. The arrival time of the initial simulation is earlier than that of the observation, suggesting the initial model is stiffer than the true subsurface profile. The misfit between the observation and the simulation is minimized during inversion.

The residuals (Figure 4.7b) decreased from the first to final simulations. The remaining residuals are mostly due to noise in the cross-correlation and the potential error in the source estimation. For better viewing, the comparison of the observed, initial and final simulated cross-correlation functions is shown in Figure 4.7c. Again, the waveform match improved during inversion. The normalized error during inversion is shown in Figure 4.8. The error decreases gradually from 1.0 to approximately 0.7 in the first run and decreases from 0.8 to 0.7 in the second run. The error jump at the beginning of the second run is due to the added higher frequencies.

For verification, Vs profile at the sinkhole location of x=20 m (67 ft) from the 2D ANT is compared to that of 2D active FWI (Tran and Sperry, 2018) in Figure 4.9. Both ambient noise and active-source data were collected at the site on the same day. Starting with the same initial Vs model, the inverted Vs profiles of the two methods are similar at this location, and both indicate the low-velocity anomaly at about 12-m (40-ft) depth. The 2D ANT produces similar results with much less field-testing effort and traffic disruption.

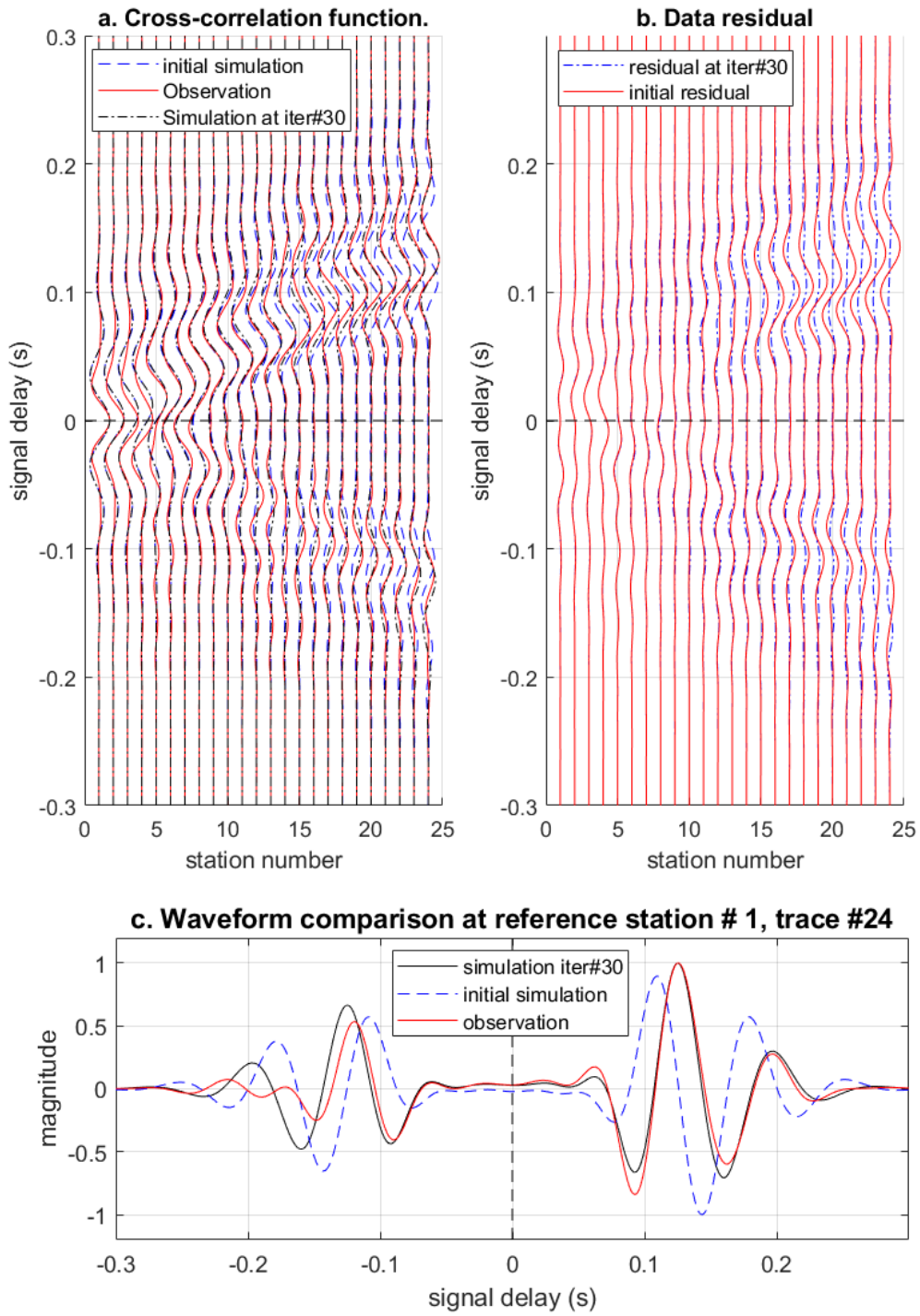

Figure 4.7. Pre-grouting US-441 highway: (a) On the reference station #1, comparison of the observed cross-correlation function (red), first simulation (blue) and final simulation (black); (b) Normalized cross-correlation function residual. Each trace is amplified with the offset distance to the reference station. The initial residual (red) is compared to the final residual (blue); and c) Cross-correlation waveform comparison at the reference station #1, trace #24.

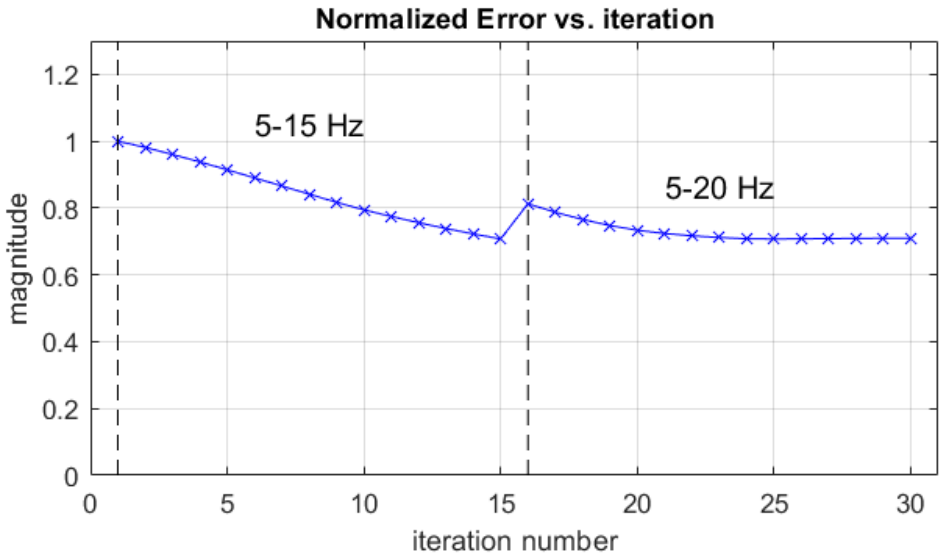

Figure 4.8. Pre-grouting US-441 highway: Normalized misfit error vs. iteration number.

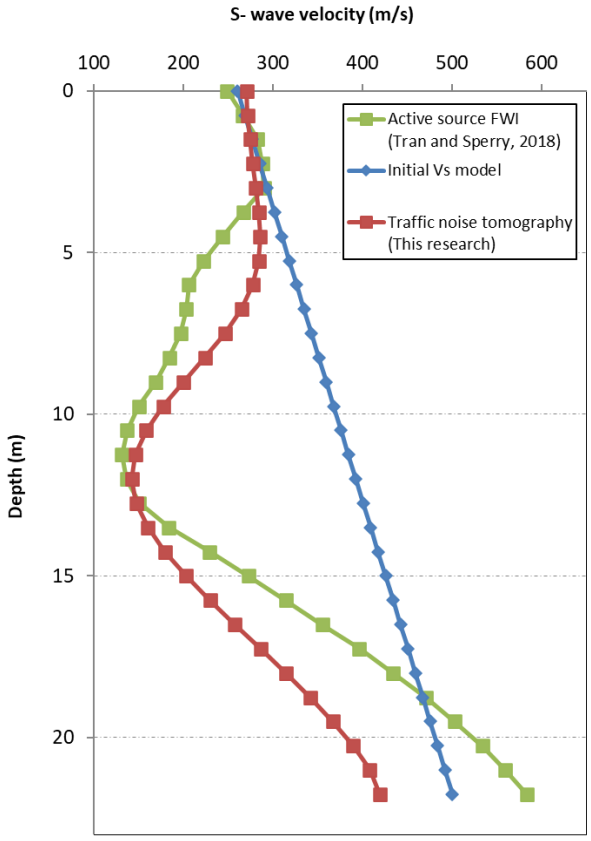

Figure 4.9. Pre-grouting US-441 highway: Comparison of the inverted Vs profiles at the sinkhole at x=20 m (67 ft)

4.2.2 Post-grouting data

After grouting, traffic noise data were acquired at the US441 site again in January 2021. The acquisition system for the post-grouting data was the same as that of the pre-grouting data. The land-streamer of 24 vertical 4.5-Hz geophones at 1.5-m (5-ft) spacing was placed along the roadway on top of the grout. Traffic noise from passing-by vehicles were collected for 10 records of two minutes (120 s) each, for a total recorded time of 20 minutes. With the similar data processing steps of the pre-grouting data, the cross-correlation functions were retrieved from the traffic noise records. Figure 4.10a displays a 120 s record of the traffic noise after low-pass (<30 Hz) filtering. It clearly shows noises induced by several passing-by vehicles.

One recorded vehicle event is shown by Figure 4.10b. In this 3-second record, a vehicle ran through receivers 1 to 24, and generated several surface waves events (highlighted with blue dash lines in Figure 4.10b). The apparent velocity of these surface wave events is about 250 m/s (e.g., 34.5 m in 0.15 s). The filtered noise record is then divided into segments of 0.3 s, cross-correlated, and stacked to generate the cross-correlation functions (Figure 4.10c). The surface wave events (blue dash lines) are evident in the cross-correlation function. The apparent velocity of the surface waves in the cross-correlation function is approximately 250 m/s (833 ft/s).

The same initial model as that of the pre-grouting data inversion is used. The initial Vs is linearly increasing from 250 m/s to 500 m/s (833 ft/s to 1667 ft/s) from the ground surface to 22.5-m (75-ft) depth. Vp is twice Vs, and the density is set to 1800 kg/m^3. Two inversion runs were conducted with frequency bands of 5~15 Hz and 5~20 Hz, respectively. Each run lasted 15 iterations.

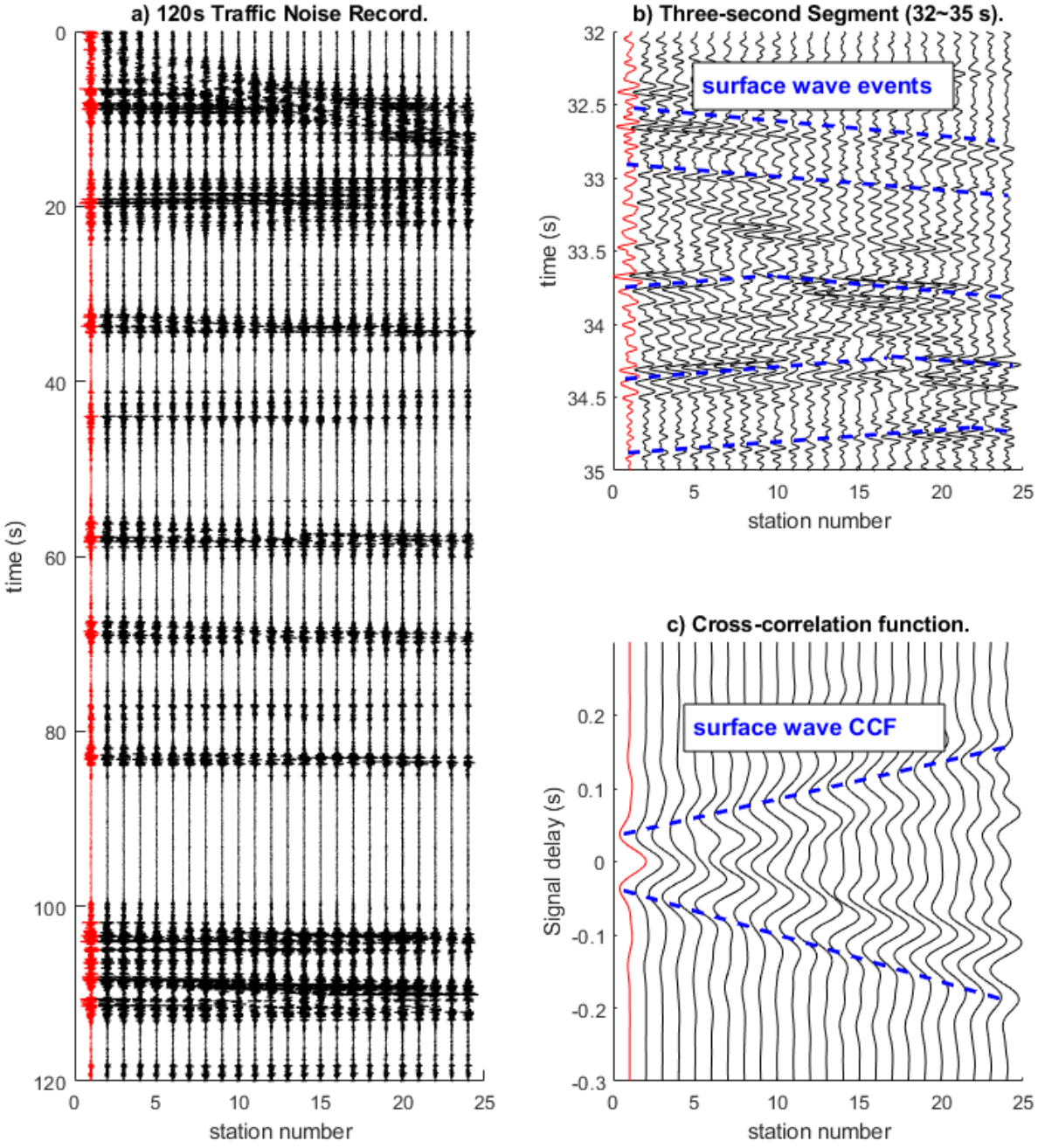

Figure 4.10. Post-grouting US-441 traffic noise data processing: (a) The 120-s length traffic noise record after low-pass (<30 Hz) filtering; (b) A three-second (32~35 s) segment of the traffic noise record; and (c) The retrieved cross-correlation function at the reference station #1. The record on the reference station (station #1) is highlighted with red.

The results of both runs are displayed in Figure 4.11. The final result (Figure 4.11c) reveals a high-velocity zone with Vs ~700 m/s (2300 ft/s) at distance of 20 m (66 ft), which is the same location of grouting. This high-velocity zone represents the grouting material and densified soil around the grouting volume. No evident low-velocity zone at the void location (white curve) exists in the inversion result; suggesting that the grouting operation was successful, and the void was sufficiently filled.

The waveform comparison of the observed and simulated cross-correlation functions is shown Figure 4.12a. The red curves are the observed cross-correlation function at 5-20 Hz. The blue and black dash curves are the initial and the final simulated cross-correlation functions, respectively. The improvement of data fitting during inversion is evident. The arrival time of the initial simulation is later than that of the observation, suggesting the initial model is softer than the true subsurface profile (due to grouting). The misfit between the observation and the simulation is minimized during inversion.

The waveform residual (Figure 4.12b) was relatively small at the beginning of the inversion, suggesting that the ground truth of subsurface Vs is close to lateral homogeneous. The influence of model update is evident in the comparison of the waveform with the largest offset (Figure 4.12c). The initial arrival time of the surface waves is greater than that of the observation. This difference in arrival time has been significantly reduced after 30 iterations of model updating, and observed and simulated waveforms are well matched at the end.

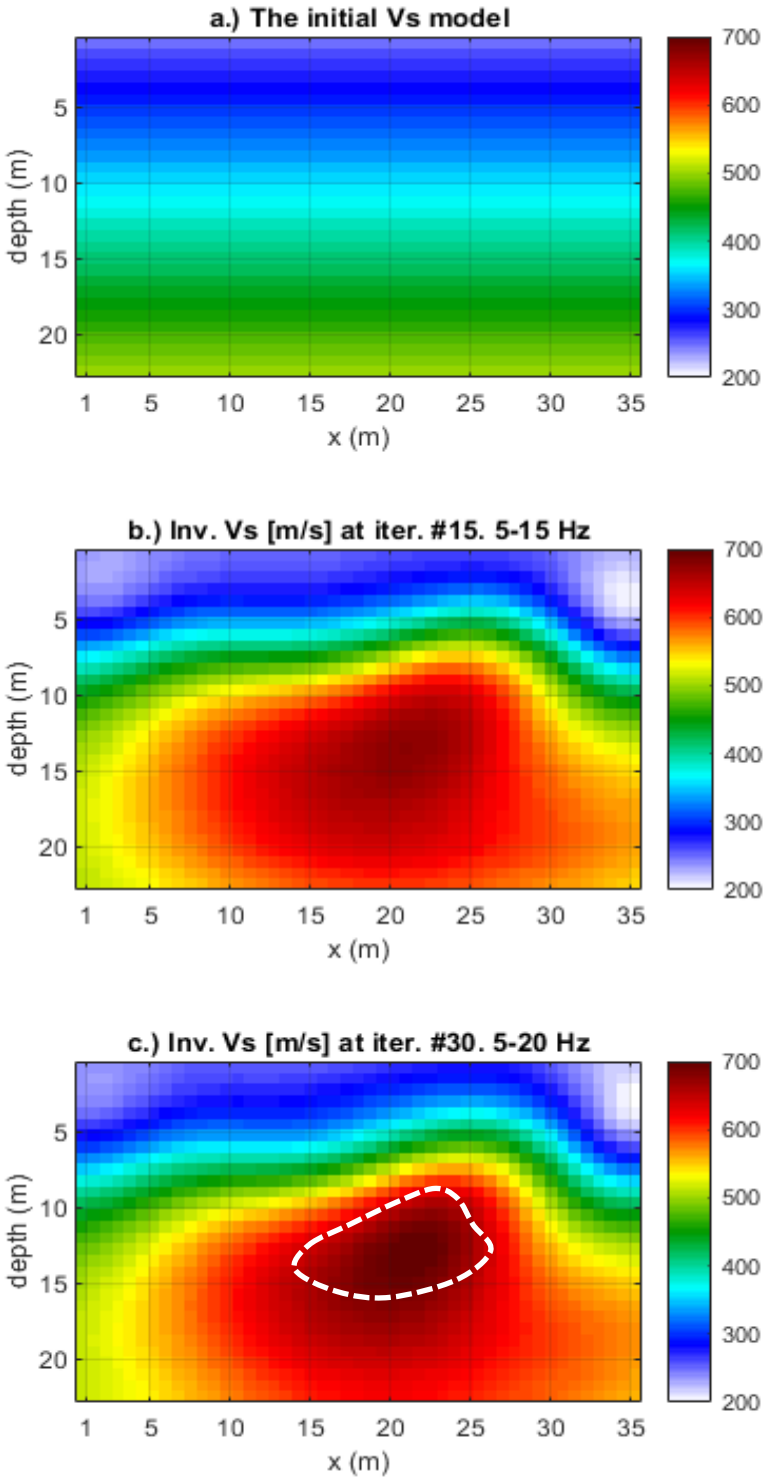

Figure 4.11. Post-grouting US-441 highway: (a) Initial Vs model; (b) Inverted Vs after 15 iterations (the first run); and (c) Inverted Vs after 30 iterations (the second run). The white curve indicates the void location shown in Figure 4.6.c. Vs at shallow depth (0–8 m) of 250–300 m/s is similar to that of pre-grouting condition shown in Figure 4.6.c.

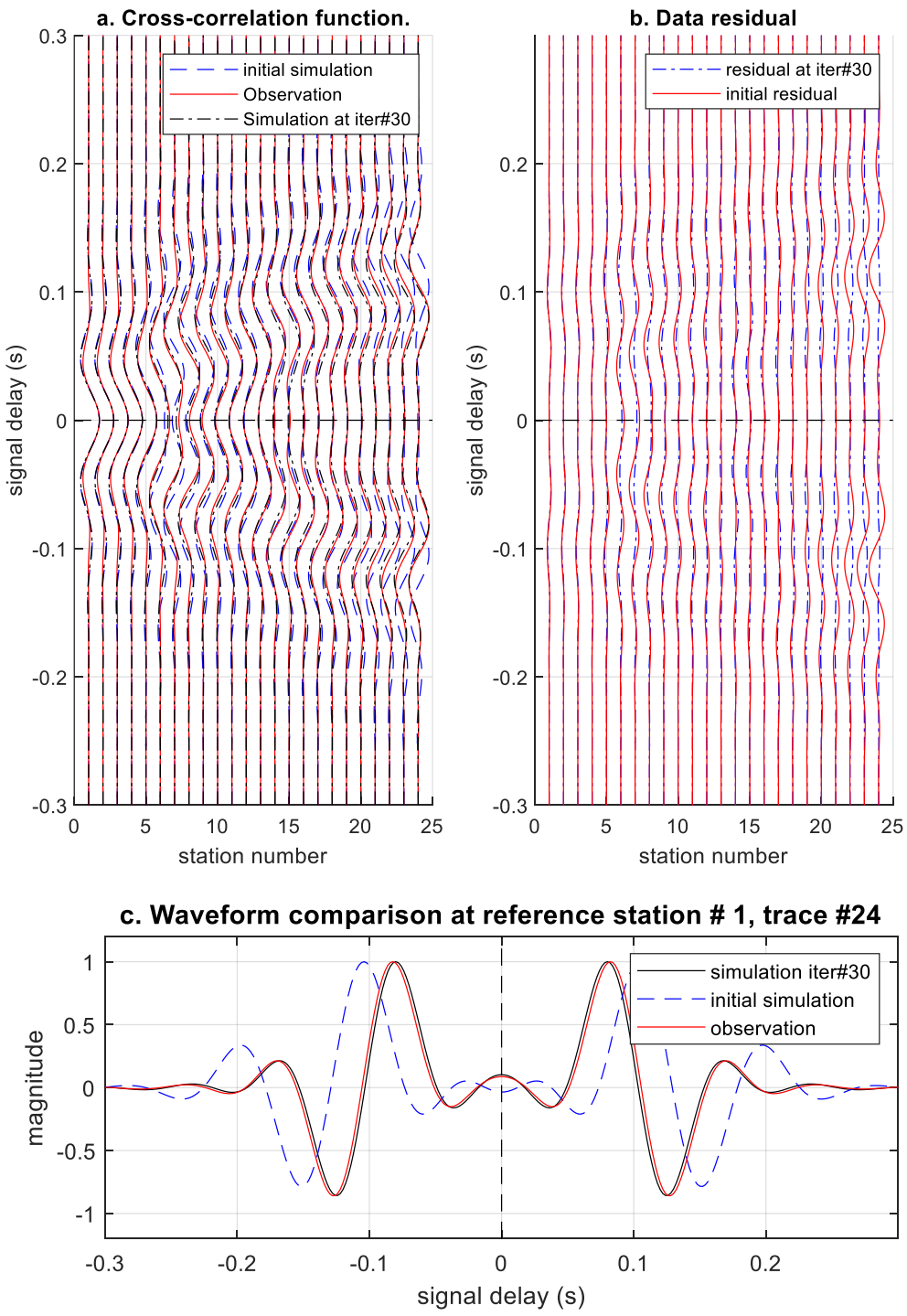

Figure 4.12. Post-grouting US-441 highway: (a) On the reference station #1, comparison of the observed cross-correlation function (red), first simulation (blue) and final simulation (black); (b) Normalized cross-correlation function residual. The initial residual (red) is compared to the final residual (blue); and (c) Cross-correlation waveform comparison at the reference station #1, trace #24.

Because no anomaly exists, the inversion converges rapidly. Figure 4.13 shows the changing of the misfit error with the iteration number. The normalized error drops rapidly to 0.25 after the first run. The location of grouting (Figure 4.11b) is generally identified after the first run. The absolute value of model update is small during the second run. However, the second run refined the model, and increased the velocity of the grouting material at depths of 10-15 m (33-50 ft) (Figure 4.11c).

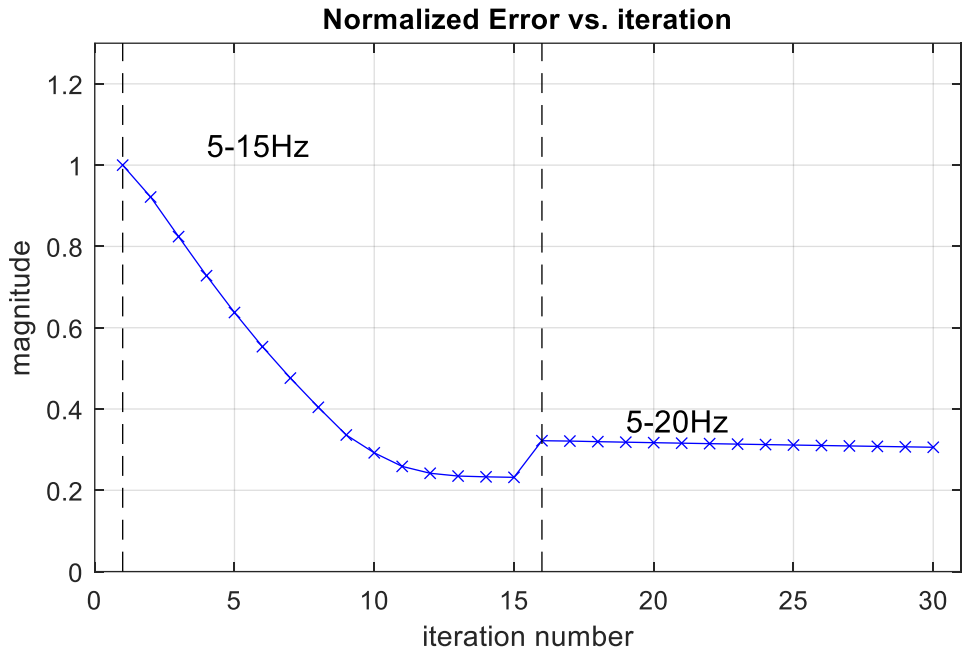

Figure 4.13. Post-grouting US-441 highway: Normalized misfit error vs. iteration number.

4.3 Miami Highway Bridge

The second test site is at a bridge construction site in Miami, containing a deep and large void identified during construction. The test site (Figure 4.14) is in an urban area, and next to Highway I-395 and several local roads. The traffic noise records were collected by a linear array of forty-eight 4.5-Hz vertical receivers at 2.0-m (6.6-ft) spatial interval, for a spread length of 94 m (313 ft). Twelve noise records were collected and each lasted two minutes (120 s) for a total of

24 minutes. Vehicles were frequently passing by during the recording time, providing good signal strength of the traffic-induced surface waves. The seismogram of one traffic noise record is displayed in Figure 4.15.

The traffic noise record is filtered to preserve the low frequencies (<25 Hz) and then divided into 0.3 second segments. The filtered data is shown in Figure 4.15a. The data contain abundant traffic-induced surface waves, because of the high traffic volume around the site area. A sample surface wave event (Figure 4.15b) can be found at 12.4 s. Two blue dash lines are used to highlight this event.

Figure 4.14. Miami test site

The dominant frequency range of the recorded traffic noise is 5-25 Hz, with consistent wave propagation pattern. Therefore, 5-25 Hz data were used for analysis. Higher frequencies (>25 Hz) are not needed for deep void imaging, since these short-wavelength components only propagate at shallow depths, and do not pass by the deep void. The sample cross-correlation functions calculated for one reference trace is shown in Figure 4.15c. The blue dash line highlights the surface wave components. In the cross-correlation functions, the signals with positive lag (signal delay > 0) are dominant. This means the dominant direction of in-coming surface wave signals is the direction with decreasing station numbers (from station 48 to 1). There is an evident phase shift in the surface wave events. The surface waves recorded by stations 26 to 48 appear to be dragged up to the direction of positive time lag (greater time delay). This is a sign of the surface waves traveling through a low-velocity anomaly.

The inversion starts with a homogenous velocity model (Figure 4.16a) with Vs = 700 m/s (2,333 ft/s), Vp = 1400 m/s (4666 ft/s) and density of 1800 kg/m^3. As the consistent cross-correlation signals are available at 5 Hz to 25 Hz, two inversion runs were conducted with frequency bandwidths of 5-15 Hz and 5-25 Hz, respectively. The inverted Vs models of the two runs are displayed in Figures 4.16b and 4.16c, respectively. Both results show a large low-velocity zone at 28-40 m (93-133 ft) depth, which is at the void location. The two results do not differ significantly in terms of the location of the void. However, the second run updates the model to show a high-Vs zone above the void, which is consistent with the SPT data (presented latter in this section).

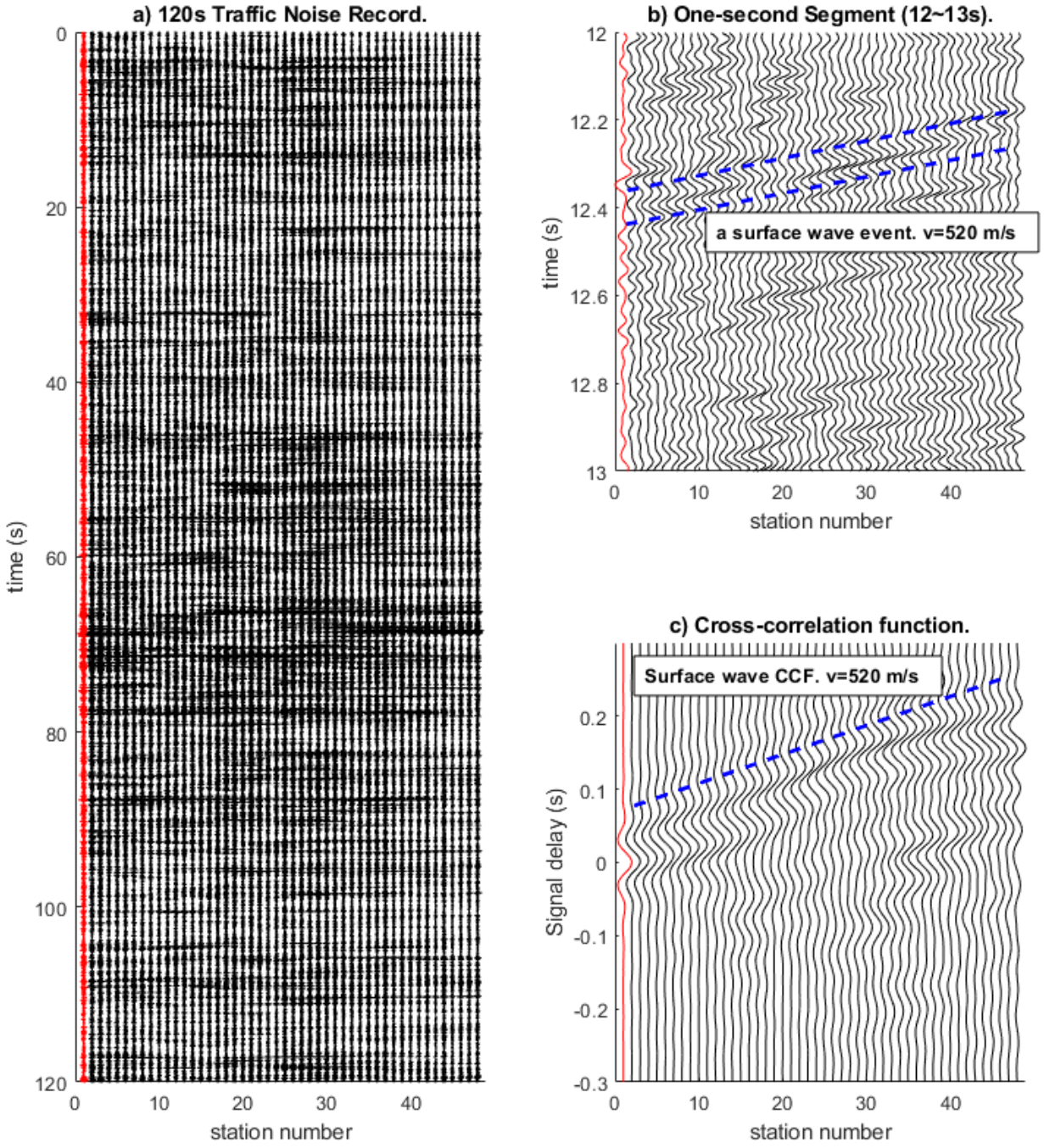

Figure 4.15. Miami site data processing: (a) The 120-s length traffic noise record after low-pass filtering; (b) A one-second segment of the traffic noise record; and c) The retrieved cross-correlation function at the reference station #1. The record on the reference station (station #1) is highlighted with red.

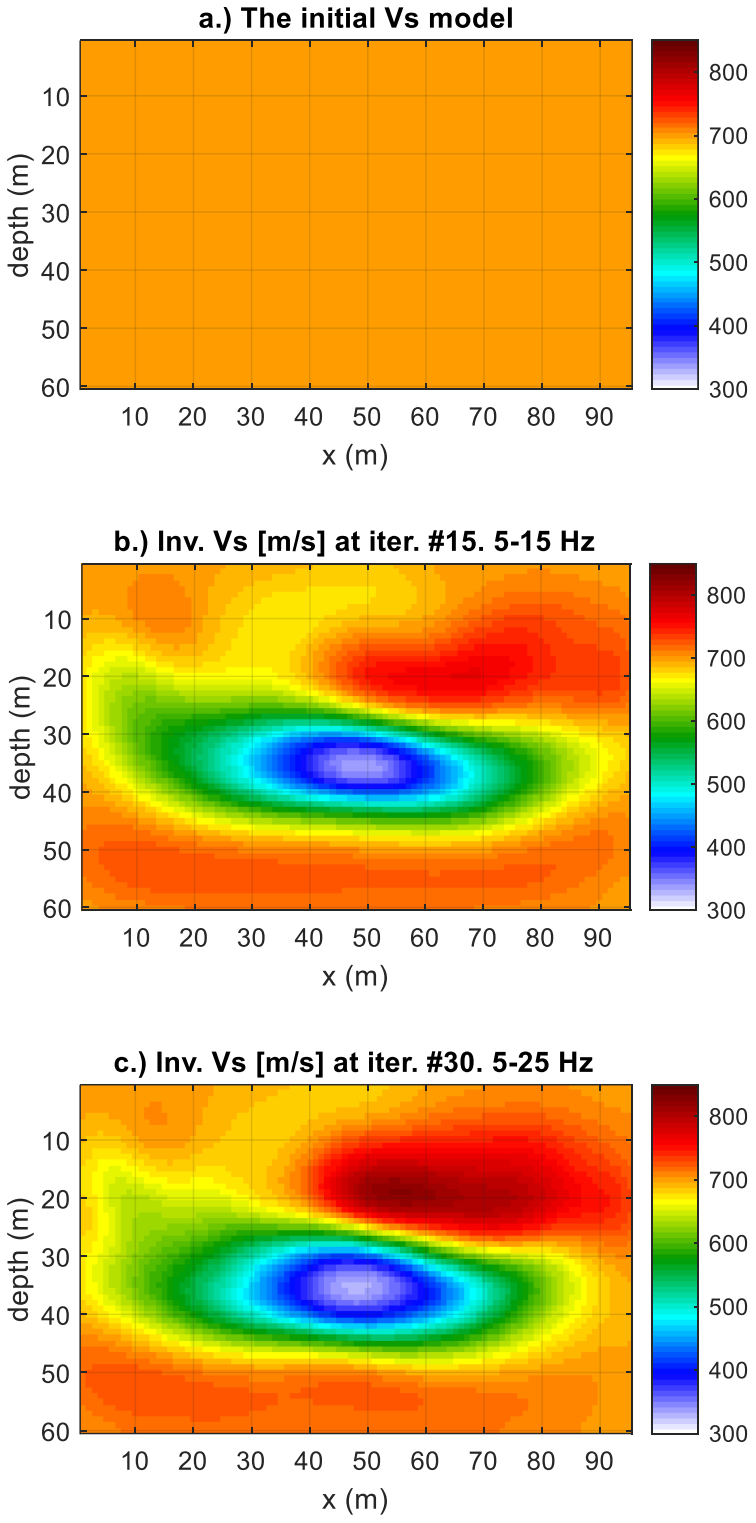

Figure 4.16. Miami site: (a) Initial Vs model; (b) Inverted Vs of the first run at 5-15 Hz; and (c) Inverted Vs of the second run at 5-25 Hz.

The waveform comparison of the observed and simulated cross-correlation functions is shown in Figure 4.17. The red curves are the observed cross-correlation function of traffic noise at 5-25 Hz. The blue and black dash curves are the initial and the final simulated cross-correlation functions, respectively. The overall fitting of the waveforms improved during the inversion. At the large-offset stations (25 to 48), the misfit was substantially reduced. At station 48 with the largest offset from reference station 1, the optimization of surface wave arrival time is evident (Figure 4.17c). The arrival time of the initial simulation is earlier than that of the observation, suggesting the initial model is stiffer than the true subsurface profile (due to the large void). After thirty iterations, the simulation and the observation have similar arrival times and match well.

The normalized misfit error is shown in Figure 4.18 for all iterations. The error decreases from 1 to 0.7 in the first run, and does not change much during the second run. As observed in the inverted results (Figure 4.16), the first run at low-frequency (5-15 Hz) data characterized most of subsurface structure including the void. The second run only updated the velocity of stiff rock above the void, leading to the small change of the error in the second run.

To validate the inversion result, the inverted Vs and SPT-N values are compared in Figure 4.19. The location of both Vs and SPT is at x=50 m (166 ft), which is at the center of the void. The Vs and SPT-N profiles generally agree, including the identification of the void at 28-40 m (93-133 ft) depth. Albeit the lack of high frequencies has prevented the inversion algorithm from obtaining an accurate velocity profile at shallow depths, the inverted Vs is generally consistent with the trend of the SPT-N profile, which shows a high-velocity zone around 24-m (80-ft) depth and a low-velocity zone below 28 m (93 ft). This comparison indicates that the Vs profile retrieved by the ANT method accurately reflects the subsurface conditions of this site.

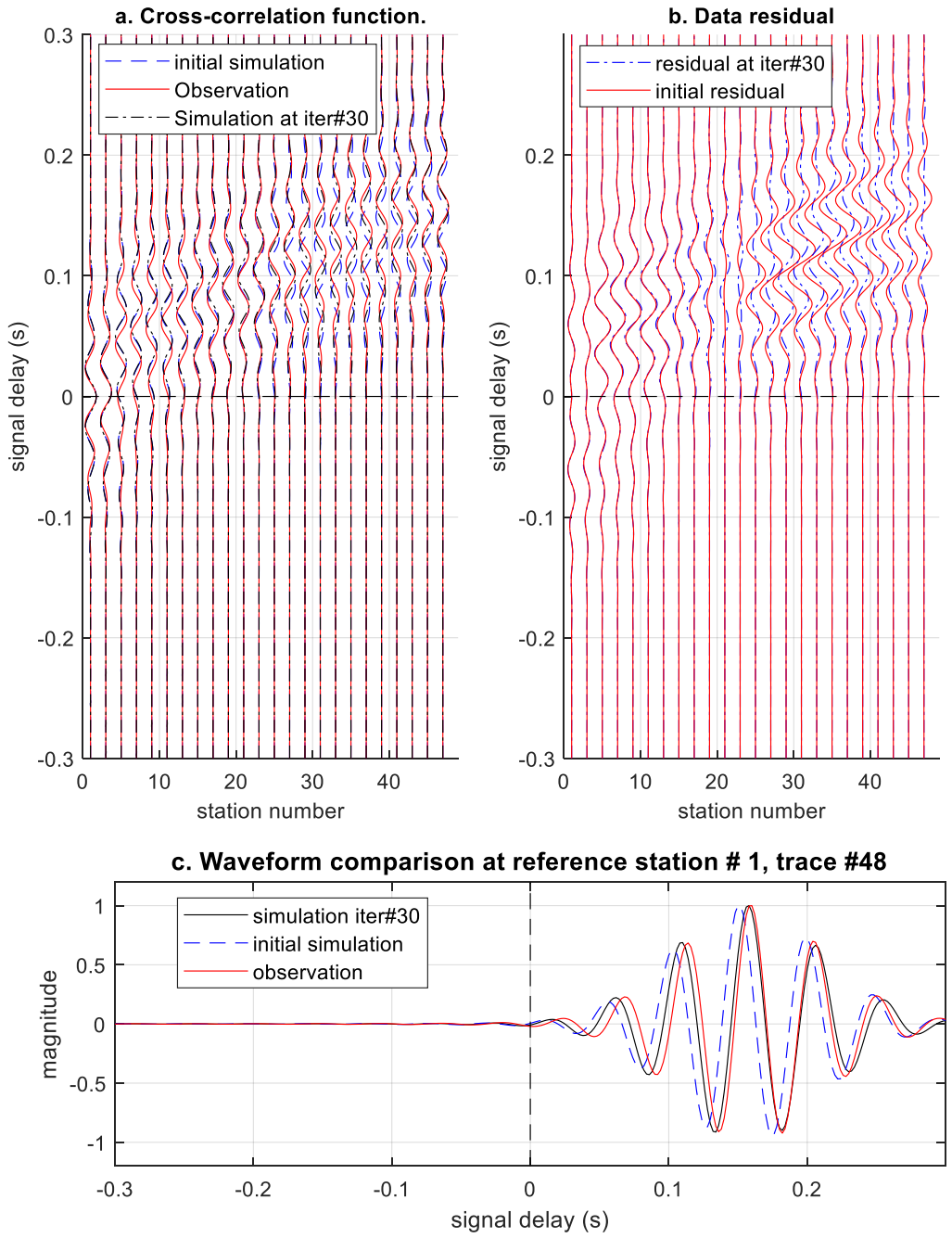

Figure 4.17. Miami site: (a) On reference station #1, comparison of the observed cross-correlation function (red), first simulation (blue) and final simulation (black); (b) Cross-correlation function residual. The initial residual (red) is compared to the final residual (blue); and (c) Cross-correlation waveform comparison at the reference station #1, trace #48.

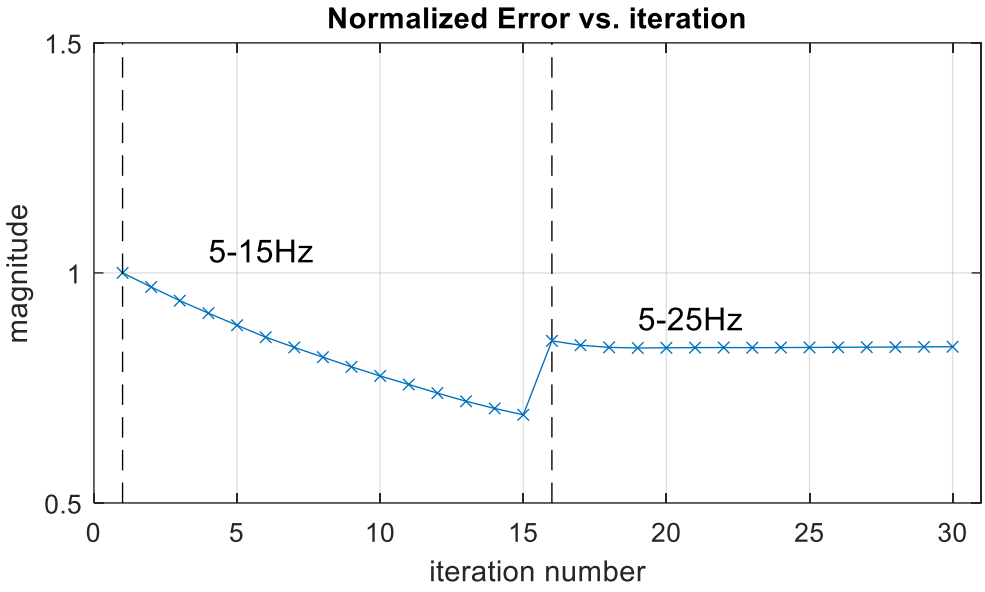

Figure 4.18. Miami site: normalized misfit error vs. iteration number.

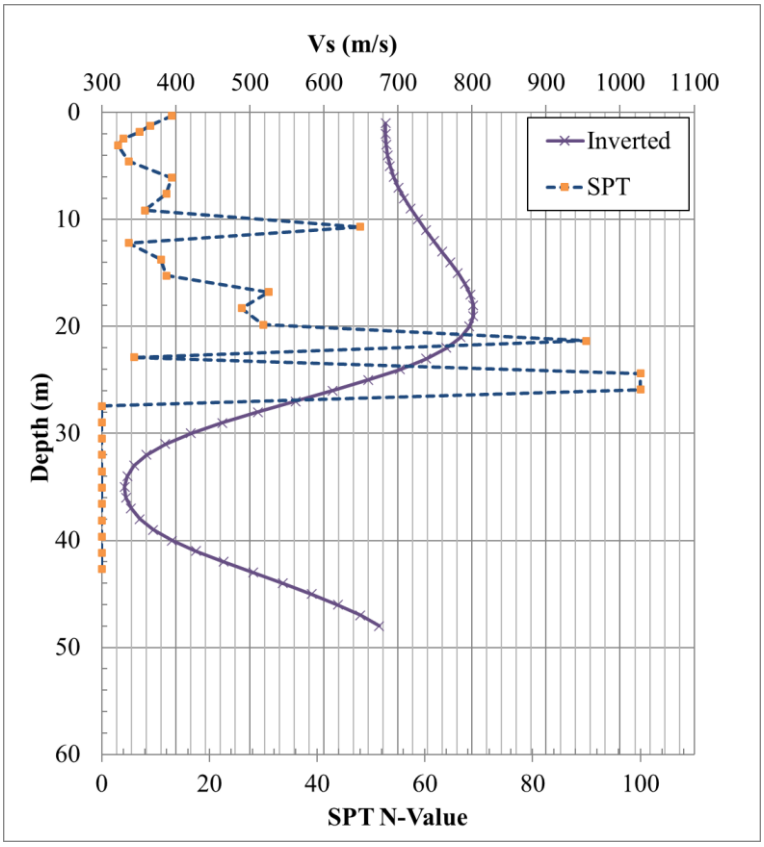

Figure 4.19. Miami site: comparison of Vs and SPT-N values at the void

4.4 Wekiva Parkway SR-46

The third test site is on Wekiva Parkway SR-46 (Figure 4.20), where a sinkhole recently settled, and the roadway was temporarily remediated by compaction of filled sand. Traffic noises were collected by a land-streamer of twenty-four 4.5-Hz vertical geophones at 2.0-m (6.6-ft) spacing for a total test length of 46 m (153 ft). The land-streamer was placed on the road shoulder. Ten noise records were collected and each lasted two minutes (120 s) for a total of 20 minutes. Vehicles were frequently passing by in both directions during the recording time, providing strong signal strengths of the traffic-induced surface waves.

Figure 4.20. Wekiva Parkway SR-46 site with a known sinkhole

With the same data processing steps of the previous sites, the cross-correlation functions were retrieved from the traffic noise records. Figure 4.21a displays a 120-s record of the traffic noise after low-pass (<30 Hz) filtering. It clearly shows noises induced by several passing-by vehicles. One recorded vehicle event is shown by Figure 4.21b, with the vehicle running through all receivers, from receiver 24 to receiver 1, and generating several surface waves events (highlighted with blue dash lines). The filtered noise record is then divided into segments of 0.3 s, cross-correlated, and stacked to generate the cross-correlation functions (Figure 4.21c). The surface wave events (blue dash lines) are evident in the cross-correlation function.

The initial Vs model was again established via dispersion analysis of passive-source surface waves (noise data). The dispersion spectrum image (Figure 4.22) clearly shows strong wave energy down to 5 Hz. The fundamental mode (m0) shows a nearly constant velocity of 250 m/s (833 ft/s) for the frequencies larger than 10 Hz, which suggests that Vs is about 250 m/s (833 ft/s) for the top layer. The initial Vs model (Figure 4.26a) was set to be lateral homogeneous with values increasing linearly with depth from 250 m/s to 350 m/s (833 ft/s to 1167 ft/s). The initial Vp model was created from the initial Vs model and a characteristic Poisson's ratio of 1/3.

With consistent cross-correlation signals at 5 Hz to 20 Hz, two inversion runs were conducted with frequency bandwidths of 5-15 Hz and 5-20 Hz. The first run started with the lower frequency bandwidth on the initial model, and the second run continued on the first run result as the input model. Each run stopped at a preset number of iterations (10), and it took about one hour on the same desktop computer (8 cores of 3.7-GHz processor and 64-GB RAM) for both runs.

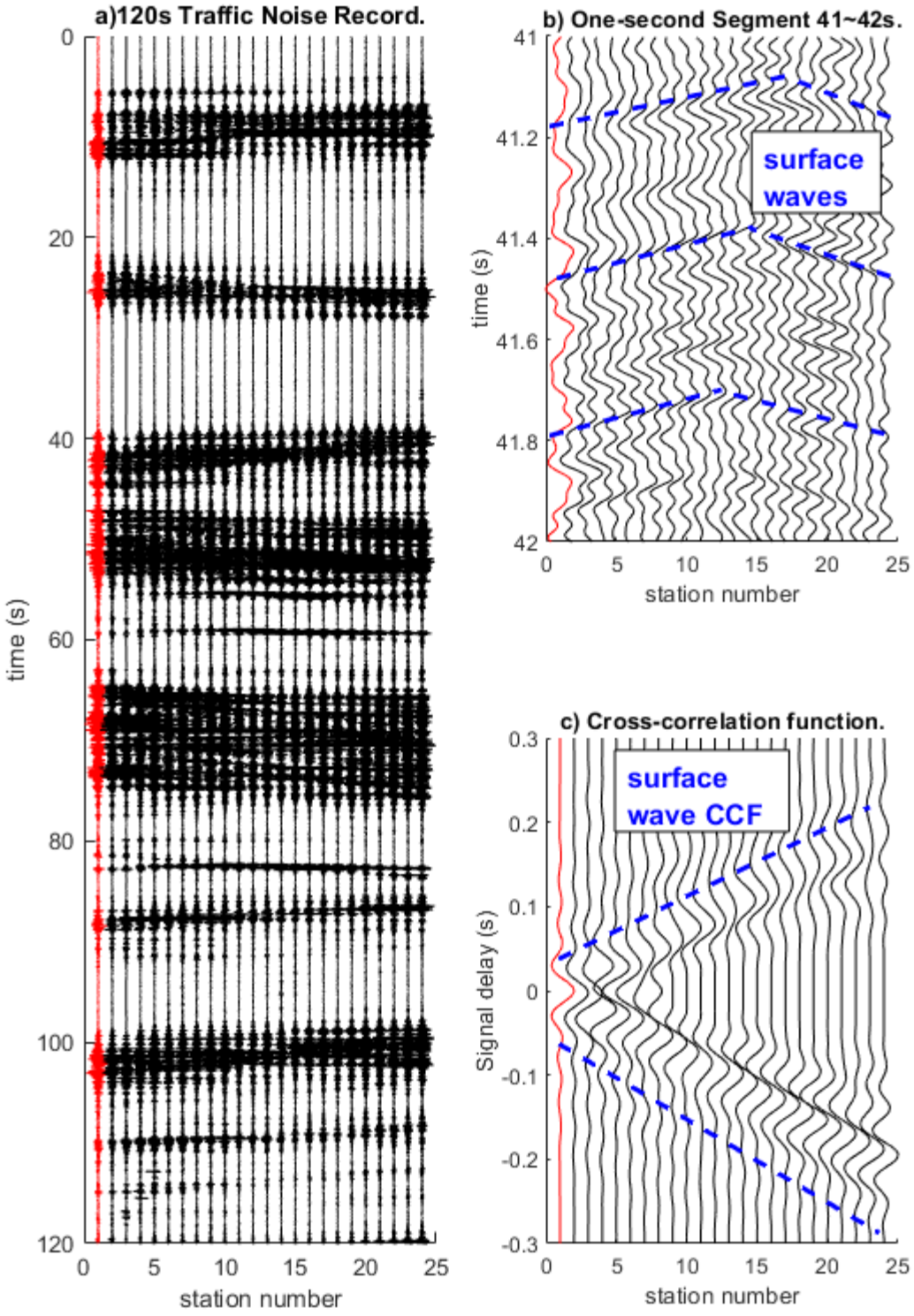

Figure 4.21. Wekiva Parkway SR-46 traffic noise data processing: (a) The raw traffic noise record; (b) A one-second segment of the traffic noise record; and (c) The retrieved cross-correlation function at the reference station #1. The record on the reference station (station #1) is highlighted with red.

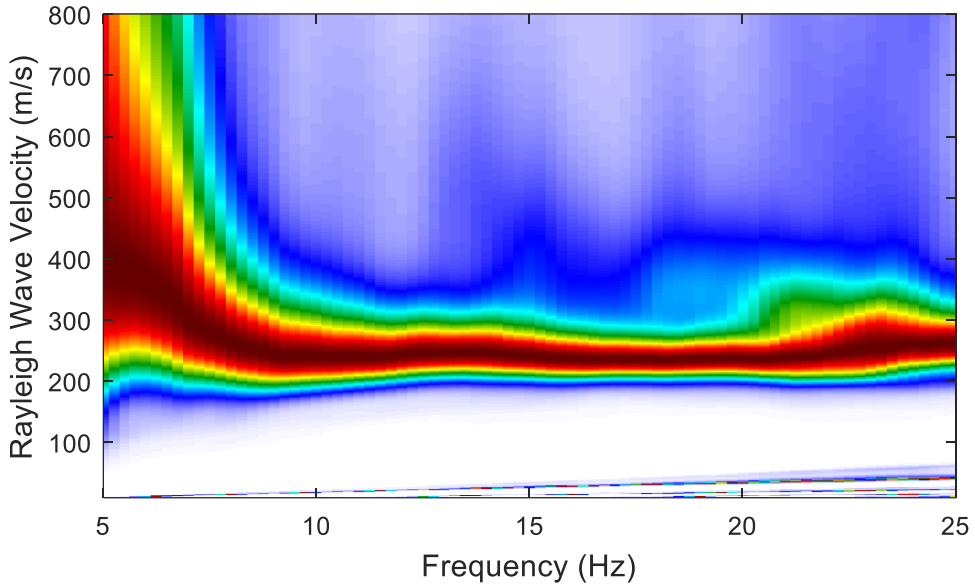

Figure 4.22. Wekiva Parkway SR-46: Rayleigh wave dispersion analysis of the traffic noise

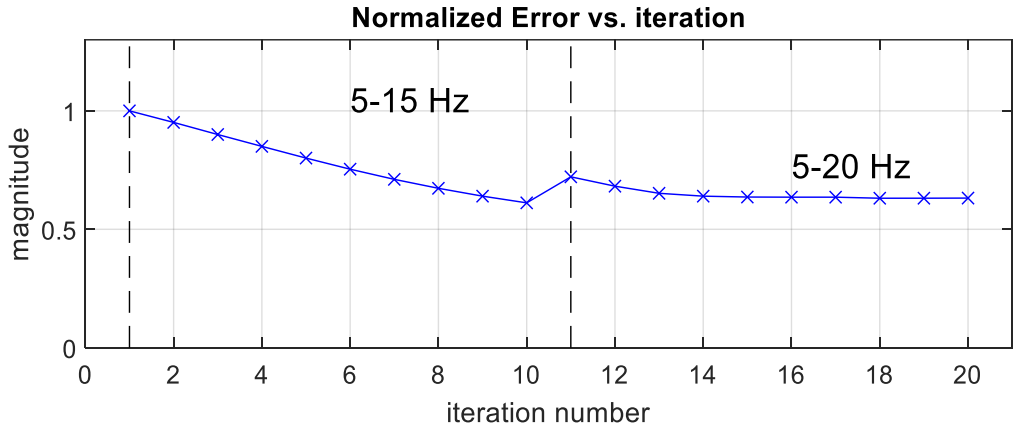

Figure 4.23. Wekiva Parkway SR-46: Normalized misfit error vs. iteration number.

The normalized error during inversion is shown in Figure 4.23. The error decreases gradually from 1.0 to approximately 0.65 in the first run and decreases from 0.7 to 0.65 in the second run. The error jump at the beginning of the second run is due to the added higher frequencies. The waveform comparison of the observed and simulated cross-correlation functions is shown Figure 4.24a. The red curves are the observed cross-correlation functions at 5-20 Hz. The

blue and black dash curves are the initial and the final simulated cross-correlation functions, respectively. The improvement of data fitting during inversion is evident. The arrival time of the initial simulation is earlier than that of the observation, suggesting the initial model is stiffer than the true subsurface profile (due to the existing soft zone). The misfit between the observation and the simulation is minimized during inversion.

The waveform residuals (Figure 4.24b) decreased significantly from the first to final simulations. The influence of the model update is evident in the comparison of the waveforms at the largest offset (Figure 4.24c). Again, the arrival time of the initial simulation is earlier than that of the observation. This difference in arrival time is reduced after 20 iterations; observed and simulated waveforms are reasonably matched at the end.

The inverted Vs profiles of the two runs are shown in Figure 4.25. The final result (Figure 4.25c) clearly shows a large low-velocity anomaly at 10-16 m (33-53 ft) depth. The anomaly center is at distance x =25 m (83 ft), which is at the location of the sinkhole. The inverted Vs at the anomaly center is about 120 m/s (360 ft/s), which is lower than the values of the surrounding area [>200 m/s (600 ft/s)] and represents the temporary backfilling materials. The grouting is planned for June 2021 for permanent remediation.

Figure 4.26 presents the CPT-5 results at a distance of 28 m (93 ft) along the survey line, shown in Figure 4.25c. The CPT-5 tip resistance (qc) is consistent with the seismic result (Figure 4.25c), and both show a soft soil zone from 10 m to 17 m (33 to 57 ft) in depth, and stiffer soil layers from 0-10 m (0-30 ft) and below 17 m (57 ft) depths.

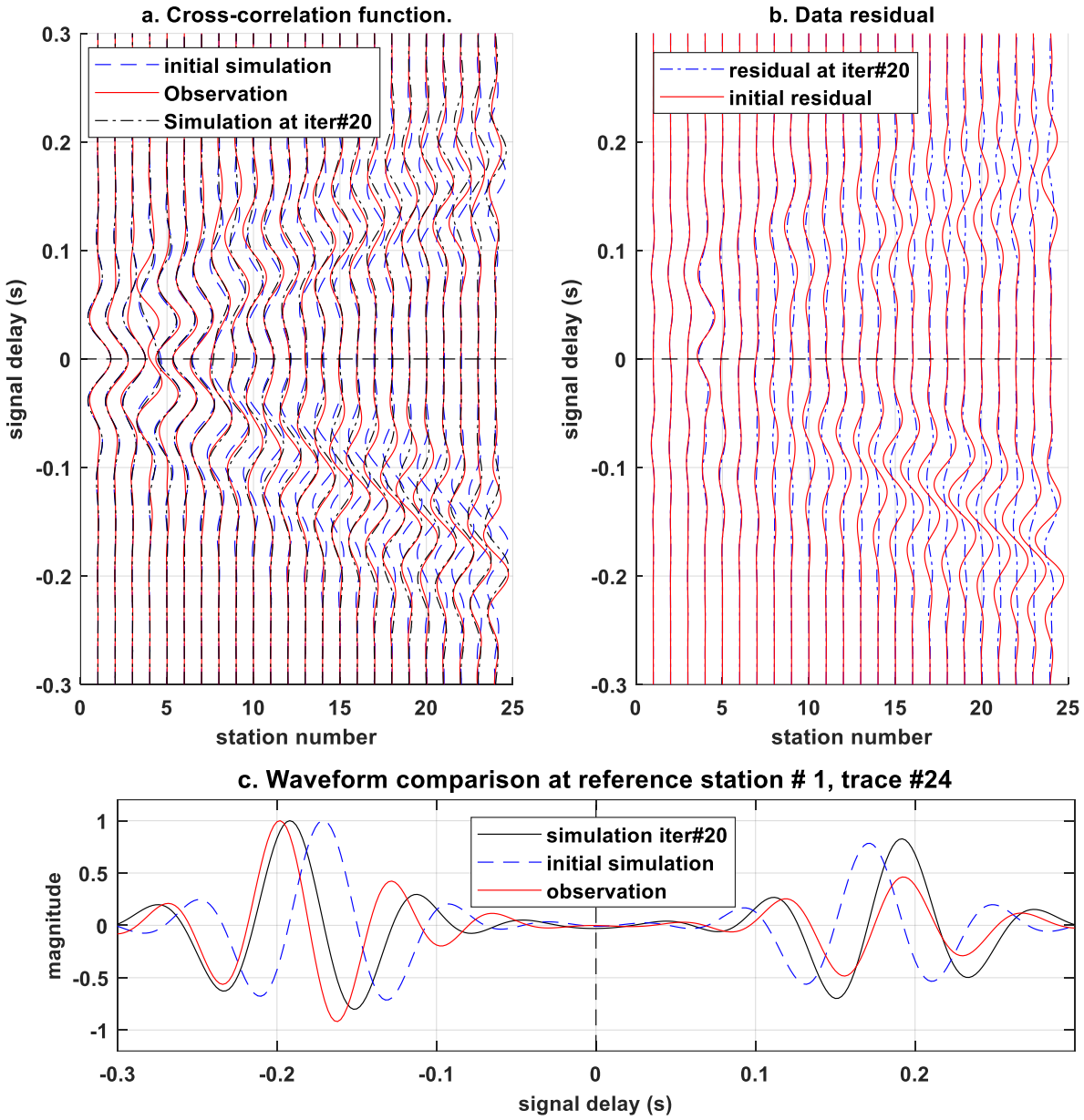

Figure 4.24. Wekiva Parkway SR-46: (a) On the reference station #1, comparison of the observed cross-correlation function (red), first simulation (blue) and final simulation (black); (b) Normalized cross-correlation function residual. Each trace is amplified with the offset distance to the reference station. The initial residual (red) is compared to the final residual (blue); and (c) Cross-correlation waveform comparison at the reference station #1, trace #24.

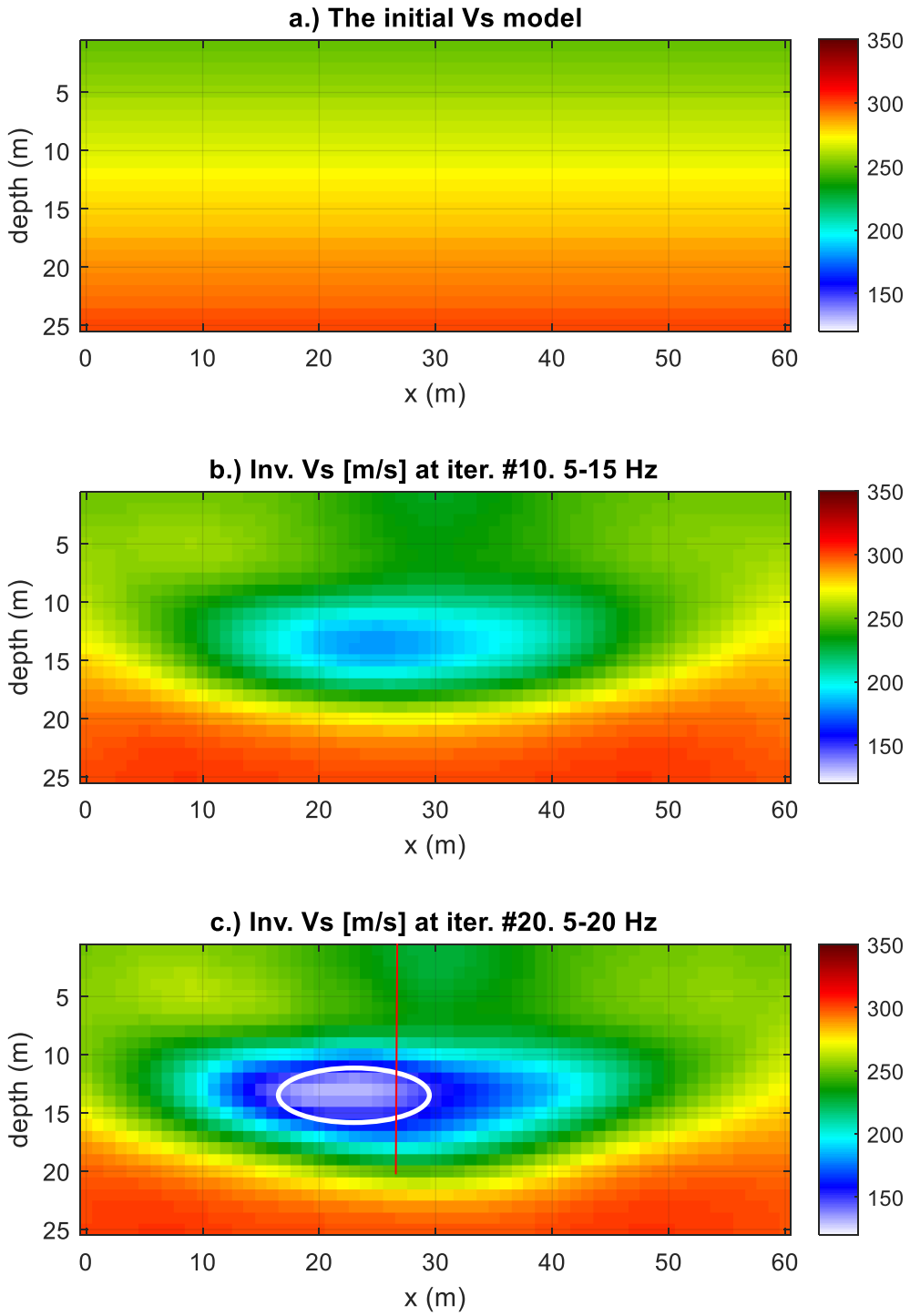

Figure 4.25. Wekiva Parkway SR-46: (a) Initial Vs model; (b) Inverted Vs after 10 iterations (the first run); and (c) Inverted Vs after 20 iterations (the second run). The white curve denotes the estimated void location. The vertical red line denotes CPT-5 shown in Figure 4.26.

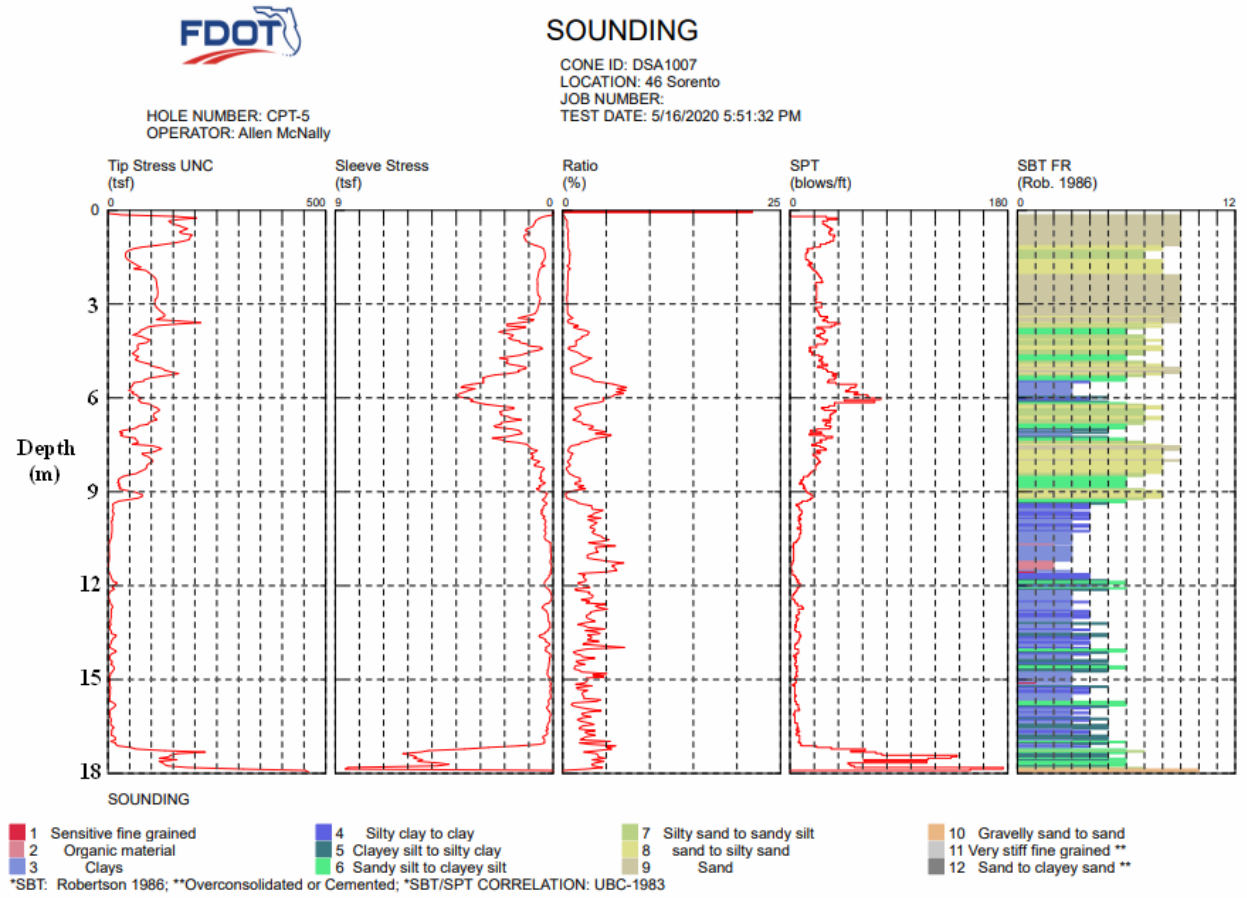

Figure 4.26. Wekiva Parkway SR-46: CPT-5 sounding results.

4.5 Wekiva Parkway Bridge

The final test site is at Wekiva Parkway, Bridge No. 110110, Bent 3 (Figure 4.27), where a void and problematic soils were encountered during the bridge foundation construction. The traffic noise records were collected by a linear array of thirty-six 4.5 Hz vertical receivers at 2.0-m (6.6-ft) spatial interval, for a spread length of 70 m (233 ft). Bridge Bent 3 is at the middle of geophone line at distance 35 m (117 ft). Ten noise records were collected and each lasted two minutes (120 s) for a total of 20 minutes. Unlike the previous sites, data were collected beneath an elevated bridge, and most of traffic noises were from the embankment at one bridge end (about

200 ft from the first geophone). Noises from vehicles passing on the elevated bridge did not propagate along the geophone line.

Figure 4.27. Wekiva Parkway, Bridge No. 110110, Bent 3 with problematic soils. A 70-m geophone array was used to record noise data and Bent 3 is at the middle of geophone array at distance of 35 m (117 ft).

A sample traffic noise record is displayed in Figure 4.28a, and a one-second blowup of the data is shown in Figure 4.28b. The noise data were filtered, divided into segments of 0.3 s, cross-correlated, and stacked to generate the cross-correlation functions (Figure 4.28c). Cross-correlation functions are only consistent at stations 1-24 and interrupted at stations 25-36. This is due to limited noise energy propagating from the embankment. Thus, only consistent cross-correlation functions at stations 1-24 were used for analysis, leading to a shorter testing length of 46 m (153 ft).

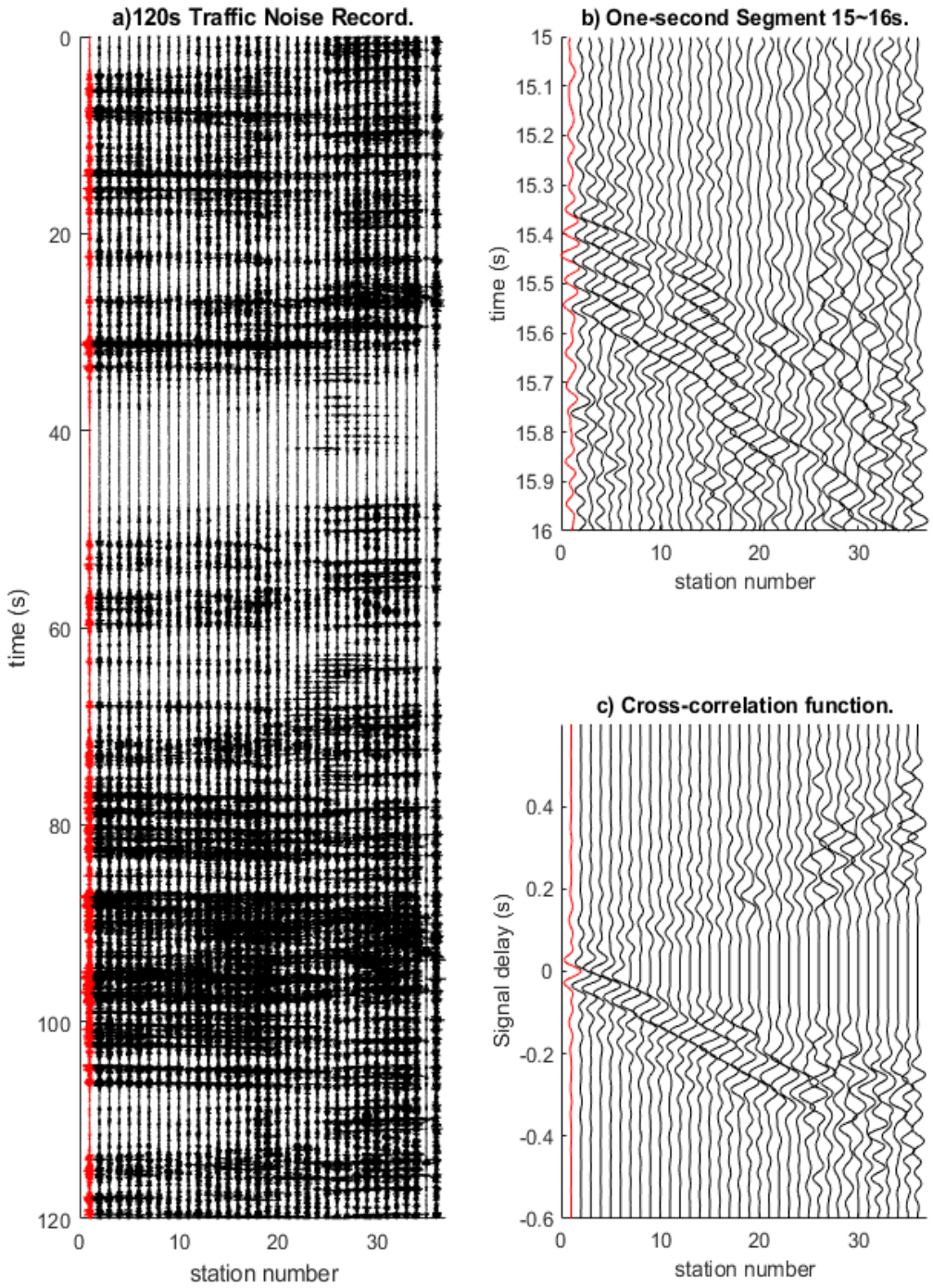

Figure 4.28. Wekiva Parkway, Bridge No. 110110, Bent 3: traffic noise data processing: (a) The raw traffic noise record; (b) A one-second segment of the traffic noise record; and (c) The retrieved cross-correlation function at the reference station #1. The record on the reference station (station #1) is highlighted with red. Consistent cross-correlation functions at stations 1-24 are used for analysis.

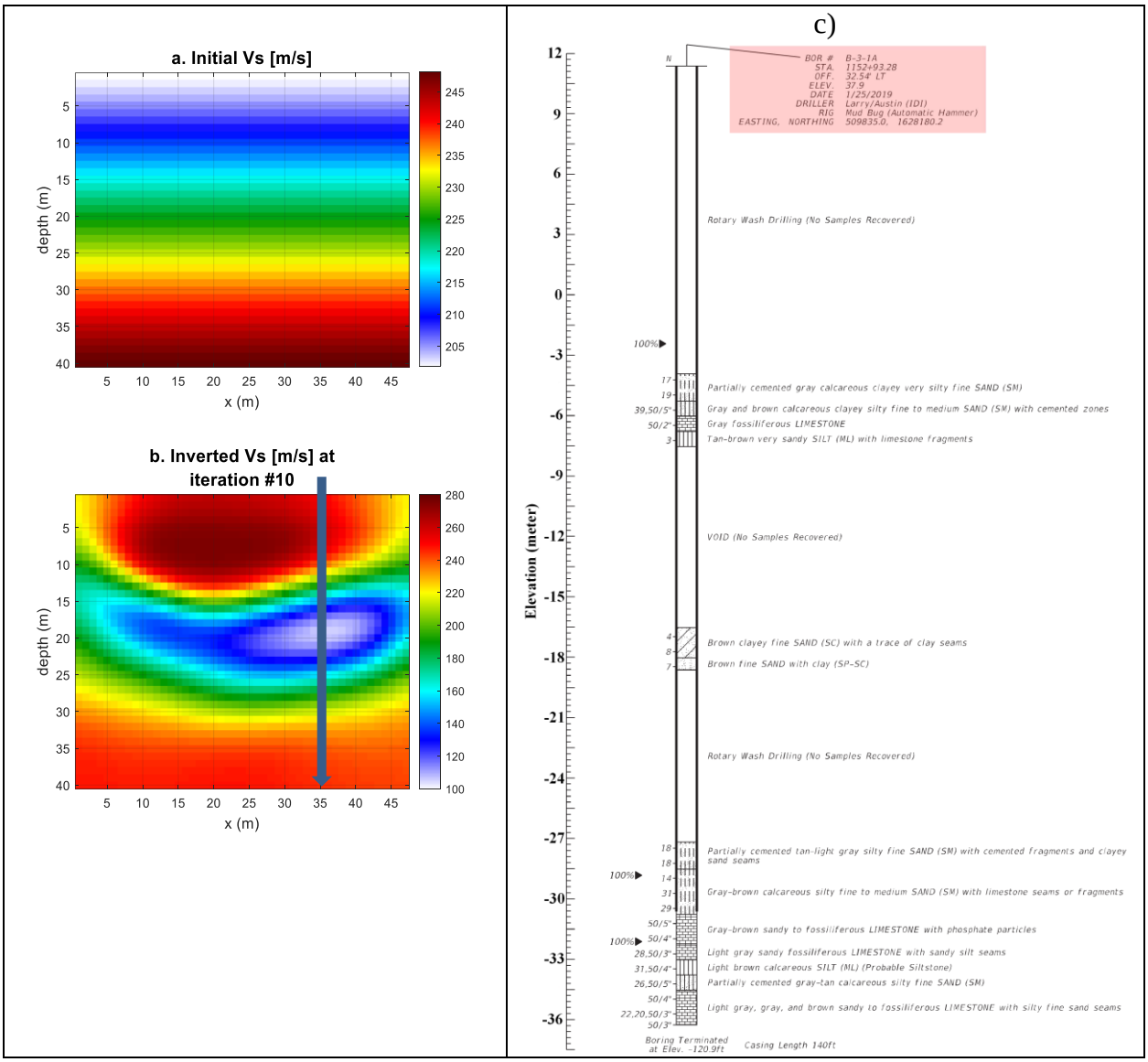

Figure 4.29. Wekiva Parkway, Bridge No. 110110, Bent 3: (a) Initial Vs model; (b) Inverted Vs and SPT boring at Bent 3 (distance of 35 m); and (c) SPT boring profile at a distance of 35 m with a void at 18-27 m below the ground surface.

As the consistent cross-correlation signals are only available at 5 Hz to 15 Hz (low frequency data can be propagating farther to geophone line), one inversion run was conducted on the initial model (Figure 4.29a). The inverted Vs profile is shown in Figure 4.29b. It clearly shows a low-velocity anomaly (Vs ~ 100 m/s) at about 17 - 25 m (57-83 ft) depth. The anomaly center of distance x = 35 m (117 ft) is at the Bent 3 location. The SPT boring profile at a distance of 35 m

(Figure 4.29c) shows a void at elevations of -7 to -16 m (-23 to -53 ft), or 18 - 27 m (60 - 90 ft) below the ground surface, which is comparable to the anomaly depth.

4.6 Conclusion

A new 2D ambient noise tomography (2D ANT) method has been successfully developed and applied to field experimental data for characterization of buried voids and roadway substructures. The method has been tested at four test sites: US-441 highway (pre- and post-grouting), Miami highway bridge, Wekiva Parkway SR-46, and Wekiva Parkway Bridge No. 110110. For each site, traffic noises were recorded continuously for 5 to 20 minutes by a linear array of geophones at 120 to 300 ft spread length. The cross-correlation functions of the traffic noise recordings were inverted to obtain subsurface Vs profiles.

For the US-441 highway site, the pre-grouting result shows that the 2D ANT successfully detects a low-velocity anomaly at the repaired sinkhole. It produces an inverted Vs profile comparable to that of the 2D active-source FWI, including Vs values and the depth and size of the anomaly. The post-grouting results suggest the void was efficiently grouted. For the Miami highway bridge site, the 2D ANT successfully detects a large and deep void with only surface measurement of traffic noises. The Vs and SPT-N profiles generally agree, including the identification of the void at 28-40 m (93-133 ft) depth. For the Wekiva Parkway SR-46 site, a low-velocity anomaly was identified at the sinkhole, suggesting the void has not been completely filled by the temporary backfilling operation. The Vs and CPT tip resistance (qc) profiles agree well, including the identification of the low-velocity anomaly at 33-58 ft depth. Lastly, for Wekiva Parkway Bridge No. 110110 site, even with limited noise data due to the elevated bridge, the method was able to image a problematic soil zone at 60 ft depth.

Based on the field experiments and results at the four test sites, the 2D ANT method showed several advantages. First, no wave citation is needed, thus minimizing the risk of collapse due to ground perturbation as well as reducing testing efforts. Second, land-streamer geophones can be deployed quickly in a few minutes on asphalt pavement, and data are acquired with minimal traffic interruption. Third, traffic noises from passing-by vehicles with various weights and speeds are sufficient to create a wide frequency range from 5 Hz to 20 Hz needed for subsurface imaging at good resolutions. The 2D ANT method can provide subsurface profiles at 3-ft resolution to 60-ft depth and at 5-ft resolution to 150-ft depth. It has been shown to be an effective geophysical tool for detection of road sinkholes and characterization of roadway substructures.

Chapter 5 – IMPLEMENTATION OF 2D ANT SOFTWARE (TASK 4)

5.1. Introduction

Task 4 was to develop a Graphical User Interface (GUI) software and user manual for the use of the 2D ANT method. The effort was focused on developing the software for graphical input, analysis, and output. The GUI was developed for technician-level personnel that can operate in the field, following basic training. For example, the user inputs dimensions of analyzed domain, locations of receivers (geophones), and the ambient traffic noise data collected in the field. The user is able to do data conditioning (i.e., filtering, windowing), remove poor channels (bad receivers) of recorded data, and check the quality of the conditioned data for individual receivers (cross-correlation function) before the data are used in the inversion analysis. The software then performs the ANT analysis (i.e., multiple frequency ranges) developed in Task 1 and produces profiles of subsurface S-wave velocity, which is displayed on the GUI. The user is able to save the input parameters, conditioned data, S-wave velocity (Vs), waveforms, and least-squares error, which can be opened in the GUI for future analysis and transferring analysis files. This report includes the user manual to run the software. A summary of the software development follows.

5.2. Summary of software development and validation

The goal of developing the GUI software is for users to upload data files, analyze the data, and obtain subsurface S-wave profiles, without requirement of programing knowledge. To accomplish this, the GUI has been developed using the MATLAB, which is the same programming language as the original ANT code. To guarantee that the GUI works the same as the original code and showing that it was implemented correctly without any losses or introduced errors, each major computational part of the code has been validated. The validation consisted of running field experimental data at the four test sites (US-441, Wekiva SR-46, Wekiva Bridge, and Miami) by

the GUI, and comparing the software results with the original results. In each case, the absolute difference between the two results was calculated, and there was zero or a negligible difference. This shows the GUI implementation was accurate, and the software is robust for various site conditions.

5.3. Conclusion

A standalone GUI software of the 2D ANT analysis has been developed. It was written in MATLAB and compiled to an executable file that can be run on computers without MATLAB. The required computer time is 30 to 60 minutes for analysis of each test lines (24 geophones), depending on the test lengths and amount of recorded traffic noise data.

The software includes several features that allow to graphically input parameters, import data, generate an initial model using spectral analysis, and run the analysis to obtain the final output (S-shear velocity profile). As a feature for the result assessment, the program provides the observed, estimated, and residual waveforms, as well as the least-squares error for each iteration. Furthermore, the inversion results and input parameters can be saved and opened in the program, allowing for future analysis and transfer of analysis files. A user manual for the ANT software is included in the Appendix.

Chapter 6 – SUMMARY

6.1. General

This project developed a novel 2D ambient noise tomography (2D ANT) method for imaging voids under roadway. Specifically, the cross-correlation function of traffic noise recordings is inverted directly to obtain velocity structures. The 2D ANT method was first demonstrated on realistic synthetic models with the accurate recovery of the model variable layers and buried voids. It was then applied to field data at four test sites in Florida. The field experimental results show that the method is capable of resolving subsurface S-wave velocity (Vs) structures and detecting voids/anomalies at various sizes and depths. The method can characterize subsurface profiles at good resolutions (3-ft pixel to 60 ft depth and 5-ft pixel to 150 ft depth). The inverted Vs profiles generally agree with the invasive tests (SPT and CPT), including the identification of voids and anomalies and depth of limestone layers. A standalone GUI software of the 2D ANT analysis has also been developed and transferred to FDOT for future uses. A discussion of each main aspect of this study follows.

6.2. Development of 2D ANT computational algorithm

A novel 2D ANT algorithm has been developed for void detection. We derived the theory for computing the noise correlation function implicitly and developed the 2D ANT algorithm that works specifically for traffic noise. Passing vehicles are assumed as moving sources along the receiver array for derivation of the model structural kernel (gradient). The source power-spectrum density is determined via the reverse-time imaging approach to approximate the source distribution. The algorithm was tested on two synthetic models (hypothetical soil/rock profiles) representing the typical Florida geological condition with soils underlain by variable bedrock, together with buried voids. One model with a void at 100-ft depth, and the other model with two

voids at 67-ft and 100-ft depths. In both cases, the inverted Vs profiles demonstrate the great capabilities of the developed algorithm in characterizing layering and buried voids. The variable layers and voids at different depths are successfully characterized at high resolution and accuracy. The void locations and sizes are well imaged.

6.3. Optimization of test configurations and noises characteristics

Optimization of test configurations (receiver locations) has been performed for the 2D ANT algorithm. The goal was to find the minimum number of receivers (maximum spacing) that enabled a successful characterization of variable layers and embedded voids. Several test configurations with receiver spacing of 5 ft to 30 ft were tested on two synthetic models with variable soil/rock layers and embedded voids. Accuracy and resolution of inverted Vs profiles were compared between simulations to identify the optimal test configuration.

From the results of the performed analyses, 5 ft receiver spacing is recommended for field testing for both shallow and deep voids. For large voids (> 20 ft diameter), 10 ft receiver spacing also generates acceptable inversion results. These optimal test configurations are recommended for field experiments. In term of required frequency content, noise data at 5-25 Hz is needed for accurate imaging of voids. The low-frequency components (5-10 Hz) are always available in traffic noises as the main benefit of this 2D ANT approach, recorded noise data should be checked during experiments to make sure the high frequency components (> 10 Hz) are recorded for accurate characterization.

6.4. Verification of 2D ANT method at field test sites

The developed 2D ANT method has been successfully applied to field experimental data for characterization of buried voids and roadway substructures. It has been tested at four test sites:

US-441 highway (pre- and post-grouting), Miami highway bridge, Wekiva Parkway SR-46, and Wekiva Parkway Bridge No. 110110. For each site, traffic noises were recorded continuously for 5 to 20 minutes by a linear array of geophones at 120 to 300 ft spread length. The cross-correlation functions of the traffic noise recordings were inverted to obtain subsurface Vs profiles.

Based on the field experiments and results at the four test sites, the 2D ANT method showed several advantages. First, no wave citation is needed, thus minimizing the risk of collapse due to ground perturbation as well as reducing testing efforts. Second, land-streamer geophones can be deployed quickly in a few minutes on asphalt pavement, and data are acquired with minimal traffic interruption. Third, traffic noises from passing-by vehicles with various weights and speeds are sufficient to create a wide frequency range from 5 Hz to 20 Hz needed for subsurface imaging at good resolution and accuracy. The 2D ANT method can provide subsurface Vs profiles at 3-ft pixels to 60-ft depth and at 5-ft pixels to 150-ft depth. The characterized Vs profiles generally agree with invasive tests (SPT and CPT), including identification of voids at various diameters (10 to 60 ft) buried at various depths (30 to 130 ft) and soil/rock layers. The field results have shown that the 2D ANT is an effective geophysical tool for detection of road sinkholes and characterization of roadway substructures.

6.5. Implementation of 2D ANT software

A standalone GUI software of the 2D ANT analysis has been developed. It was written in MATLAB and compiled to an executable file that can be run on computers without MATLAB. The required computer time is 30 to 60 minutes for analysis of each test lines (24 geophones), depending on the test lengths and amount of recorded traffic noise data.

The software includes several features that allow to graphically input parameters, import data, and run the analysis. The software users graphically input the spacing and number of

geophones, all raw collected ambient noise data from a hard drive. The users can condition the input data (i.e., filtering, windowing, removing bad channels), and check the quality of conditioned data before using for analyses. The software subsequently produces subsurface profile (S-shear velocity), which the GUI shows both on screen and in print. The guideline (software manual) is documented in detail (step by step) so that users can follow without significant training. Examples of real traffic noise recordings are also included for visual aids. The manual is included in the Appendix.

REFERENCES

Aki, K., and P. G. Richards, 2002, *Quantitative Seismology*, University Science Book, Mill Valley, CA 94941.

Artman, B., I. Podladtchikov, and B. Witten, 2010, Source location using time-reverse imaging, *Geophysical Prospecting*, 58, 861–873.

Bensen, G.D., M. H. Ritzwoller, M.P. Barmin, A.L. Levshin, F. Lin, M.P. Moschetti, N.M. Shapiro, and Y. Yang, 2007, Processing seismic ambient noise data to obtain reliable broad-band surface wave dispersion measurements, *Geophysical Journal International*, 169, no. 9, 1239–1260.

Bunks, C., F. M. Saleck, S. Zaleski, and G. Chavent, 1995, Multiscale seismic waveform inversion, *Geophysics*, 60, no. 5, 1457–1473.

Chen, J., C. A. Zelt, and P. Jaiswal, 2016, Detecting a known near-surface target through application of frequency-dependent traveltime tomography and full-waveform inversion to P-and SH-wave seismic refraction data, *Geophysics*, 82, no. 1, R1–R17.

de Ridder, S. A. L., and J. R. Maddison, 2018, Full wavefield inversion of ambient seismic noise, *Geophysical Journal International*, 215, no. 2, 1215–1230.

Foti S., C. G. Lai, G. Rix, and C. Strobbia, 2014, Surface wave methods for near-surface site characterization, CRC Press, London

Klessig, R., and Polak, E., 1972, Efficient Implementations of the Polak–Ribière Conjugate Gradient Algorithm, *SIAM J. Contro*l, 10, no. 3, 524–549.

Levander, A. R., 1988, Fourth-order finite-difference P-SV seismograms, *Geophysics*, 53, no. 11, 1425–1436.

Li, Y.E., Y. Zhang, E. Nilot, and T. Ku, 2020, Passive seismic methods for shallow and deep bedrock detection in Singapore, Fifth International Conference on Engineering Geophysics (ICEG), Society of Exploration Geophysicists, 176–180.

Liu, Q. and J. Tromp, 2004, Using Adjoint Methods to Construct 3-D Banana-Doughnut Kernels, In AGU Fall Meeting Abstracts, vol. 2004, pp. S31B-1042.

Mora, P., 1987, Nonlinear two-dimensional elastic inversion of multioffset seismic data, *Geophysics*, 52, no. 9, 1211–1228.

Nocedal, J., and S. J. Wright, 2006. Numerical optimization. Springer Science & Business Media.

Park, C., R. Miller, D. Laflen, C. Neb, J. Ivanov, B. Bennett, and R. Huggins, 2004, Imaging dispersion curves of passive surface waves: SEG Technical Program Expanded Abstracts 2004, Society of Exploration Geophysicists, 1357–1360.

Park, C. B., R. D. Miller, J. Xia, 1999, Multichannel analysis of surface waves, *Geophysics*, 64, no. 3, 800–808.

Ravaut, C., S. Operto, L. Improta, J. Virieux, A. Herrero, and P. Dell'Aversana, 2004, Multiscale imaging of complex structures from multifold wide-aperture seismic data by frequency-domain full-waveform tomography, Application to a thrust belt: *Geophysical Journal International*, 159, no. 3, 1032–1056.

Sager, K., L. Ermert, C. Boehm, and A. Fichtner, 2018, Towards full waveform ambient noise inversion, *Geophysical Journal International*, 212, no. 1, 566–590.

Shipp, R. M., and S. C. Singh, 2002, Two-dimensional full wavefield inversion of wide-aperture marine seismic streamer data, *Geophysical Journal International*, 151, no. 2, 325–344.

Sloan, S. D., 2017, Role of depth in anomaly detection using near-surface seismic methods: International Conference on Engineering Geophysics, Al Ain, United Arab Emirates, 9-12 October 2017, Society of Exploration Geophysicists, 132–135.

Sourbier, F., S. Operto, J. Virieux, P. Amestoy, and J. Y. L'Excellent, 2009a, FWT2D: A massively parallel program for frequency-domain full-waveform tomography of wide-aperture seismic data - Part 2: Numerical examples and scalability analysis, *Computers and Geosciences*, 35, no. 3, 496–514.

Sourbier, F., S. Operto, J. Virieux, P. Amestoy, and J. Y. L'Excellent, 2009b, FWT2D: A massively parallel program for frequency-domain full-waveform tomography of wide-aperture seismic data - Part 1: Algorithm, *Computers and Geosciences*, 35, no. 3, 487–495.

Tarantola, A., 1984, Inversion of seismic reflection data in the acoustic approximation: *Geophysics*, 49, no. 9, 1259–1266, doi: 10.1190/1.1441754.

Tran, K. T., and D. R. Hiltunen, 2012, Two-dimensional inversion of full waveforms using simulated annealing: *Journal of Geotechnical and Geoenvironmental Engineering*, 138, 1075–1090.

Tran, K. T., M. McVay, M. Faraone, and D. Horhota, 2013, Sinkhole detection using 2D full seismic waveform tomography, *Geophysics*, 78, no. 5, R175–R183, doi: 10.1190/geo2013-0063.1.

Tran, K. T., and J. Sperry, 2018, Application of 2-D full waveform tomography on land-streamer data for assessment of roadway subsidence, *Geophysics*, 83, no. 3, EN1–EN11.

Tromp, J., Y. Luo, S. Hanasoge, and D. Peter, 2010, Noise cross-correlation sensitivity kernels, *Geophysical Journal International*, 183, no. 2, 791–819.

Virieux, J., 1986, P-SV wave propagation in heterogeneous media: Velocity-stress finite-difference method, *Geophysics*, 51, 889–901.

Wang, Y., R. D. Miller, S.L. Peterie, S. D. Sloan, M. L. Moran, H. H. Cudney, J. A. Smith, D. Borisov, R. Modrak, and J. Tromp, 2018, Tunnel detection at Yuma Proving Ground, Arizona, USA - Part 1: 2D full-waveform inversion experiment, *Geophysics*, 84, no. 1, 1-44.

Wang, Y, K. T. Tran, and D. Horhota, 2020, Road Sinkholes Assessment with 2D Traffic Noise Cross-correlation Inversion", expanded abstract, SEG annual meeting, Houston, Texas, October 11-16.

Zhang, Y., Y. E. Li, H. Zhang, and T. Ku, 2019, Near-surface site investigation by seismic interferometry using urban traffic noise in Singapore, *Geophysic*s, 84, no. 2, B169–B180.

Appendix: Software Manual

1. Introduction

Welcome to Ambient Noise Tomography (ANT) software program. This program analyzes ambient traffic noises to extract 2D subsurface S-wave velocity profiles. It can be used for characterization of roadway sinkholes/anomalies and substructures. The software includes several features such as:

- Modifiable parameters
- Easily import and condition data
- Run analysis and export results

2. Start Page

Figure shows the first page when you run the software. The main menu includes File, Settings, and Help.

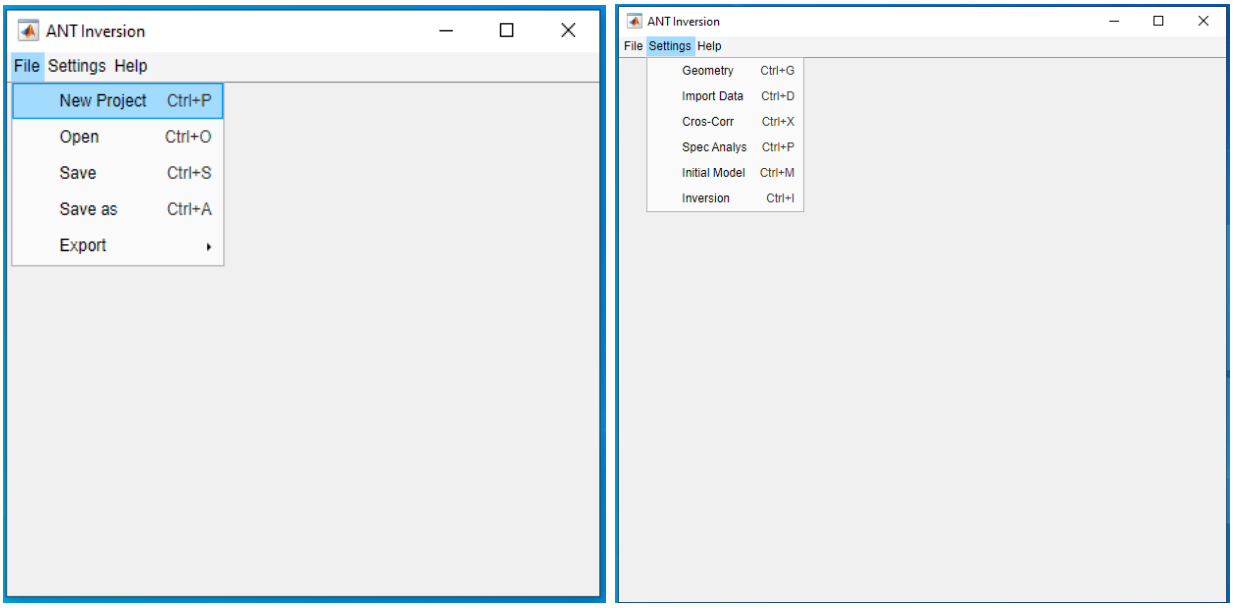

Figure 1. Start page

To start a project, you select File/New Project. This action will open the "Geometry" page as seen in Figure 2.

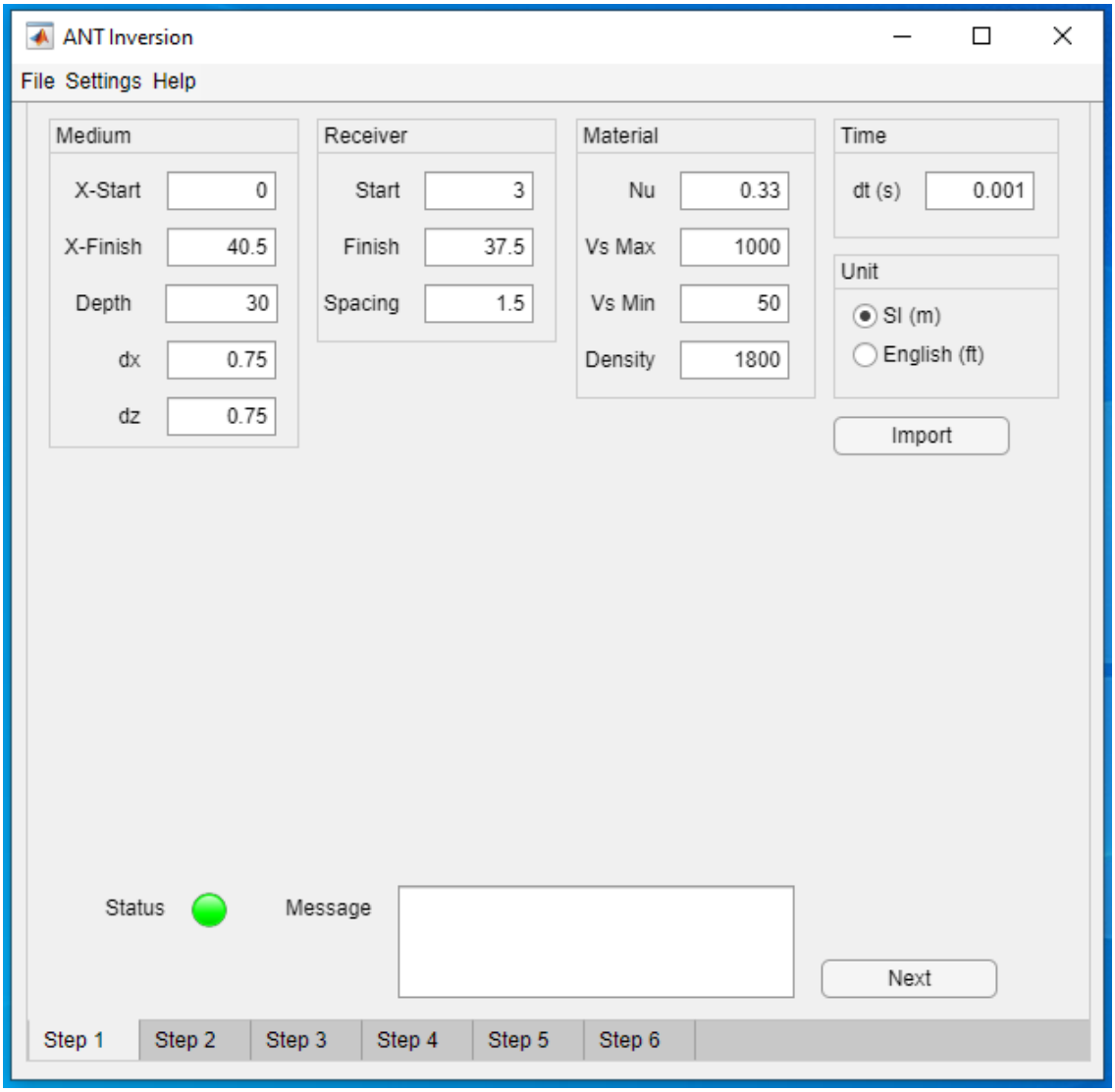

Figure 2. Geometry page

There are six required steps for the ANT analysis, as shown in the Settings menu (Figure 1, right) including:

1. Geometry
2. Input Data
3. Cross Correlation
4. Spectral Analysis
5. Initial Model

6. Inversion

3. Input Parameters

Step 1 of the ANT analysis is to input parameters that define the analyzed domain and datasets. On the "Geometry" page (Figure 2), there are a number of required parameters as defined in the below table.

Medium	Material	Receiver	Time
X-Start: Start location for the analyzed domain	Nu: Approximate Poison ratio (v) of material	Start: Physical start location of receivers	dt: data sampling rate (time interval)
X-Finish: End location the analyzed domain	Vs Max: Maximum S-wave velocity of material	Finish: Physical end location of receivers	
Depth: depth of the analyzed domain	Vs Min: Minimum S-wave velocity of material	Spacing: Spacing of receivers	
dx: Grid spacing in x direction	Density: Approximate density of material		
dz: Grid spacing in z direction			

You enter values in editable boxes for the corresponding parameters. After entering all the required parameters, the next step is to click on the "Import" button as shown in Figure 3. If the parameters are properly imported, there will be a sketch of the analyzed domain displayed in the "Step 1" tab with a message "Parameters parsed successfully". Otherwise, you need to fix any errors in the parameters.

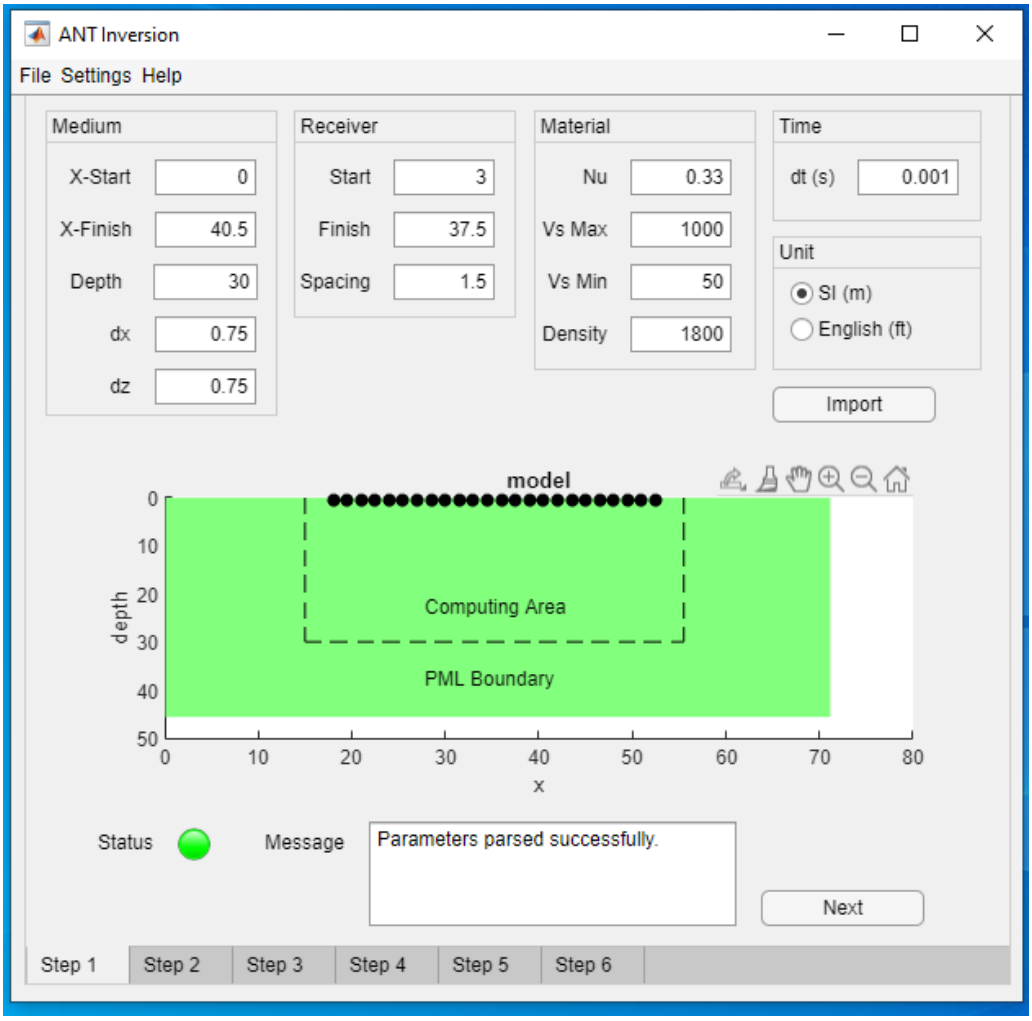

Figure 3. Import geometry parameters

4. Input Data

Step 2 of the ANT analysis is to input data. For this purpose, choose either:

1. Settings > Input Data
2. Click the “Next” button in the “Step 1” tab

to enter the “Step 2” tab (Figure 4) and then click on “Open” button on the upper left.

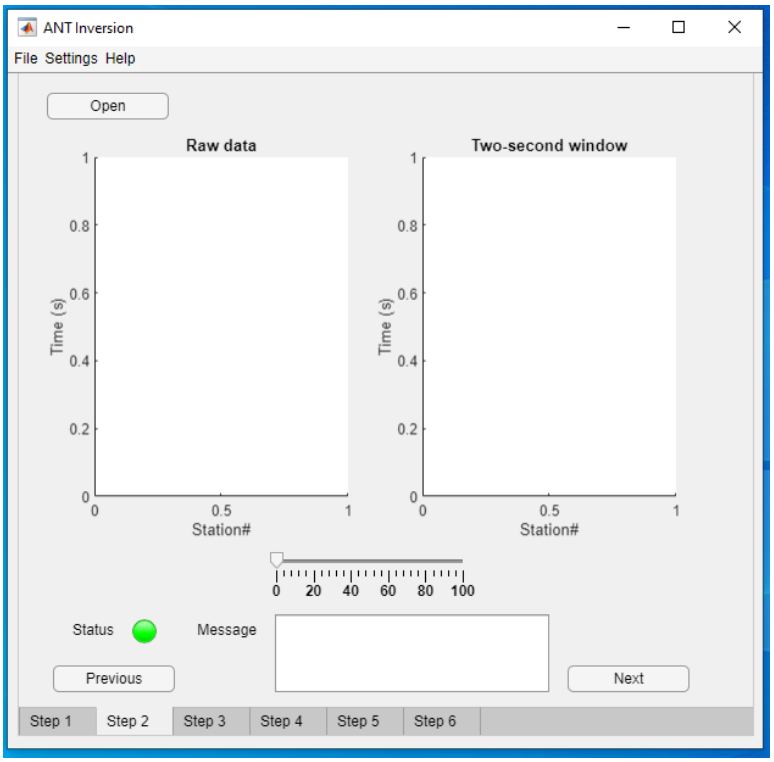

Figure 4. Open noise data

This action will open a window entitled “Select File to Open” (Figure 5). You can select one or multiple data files and click “Open”. The loaded data will be shown as seen in Figure 5. You can move the slider below the plots to display a close-up window (2 seconds) of the data. Once importing the data successfully, the status lamp will display green, and you can move to the next step.

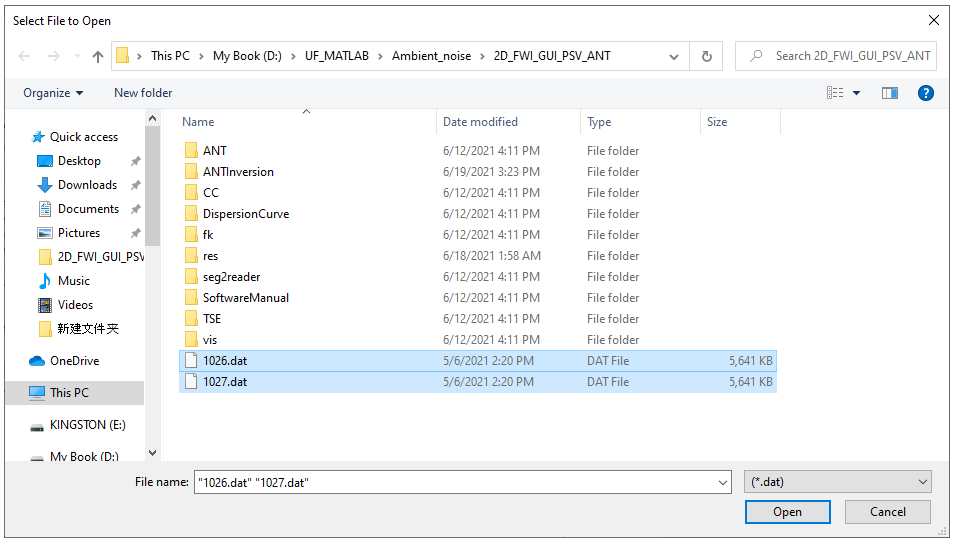

Figure 5. Data selection

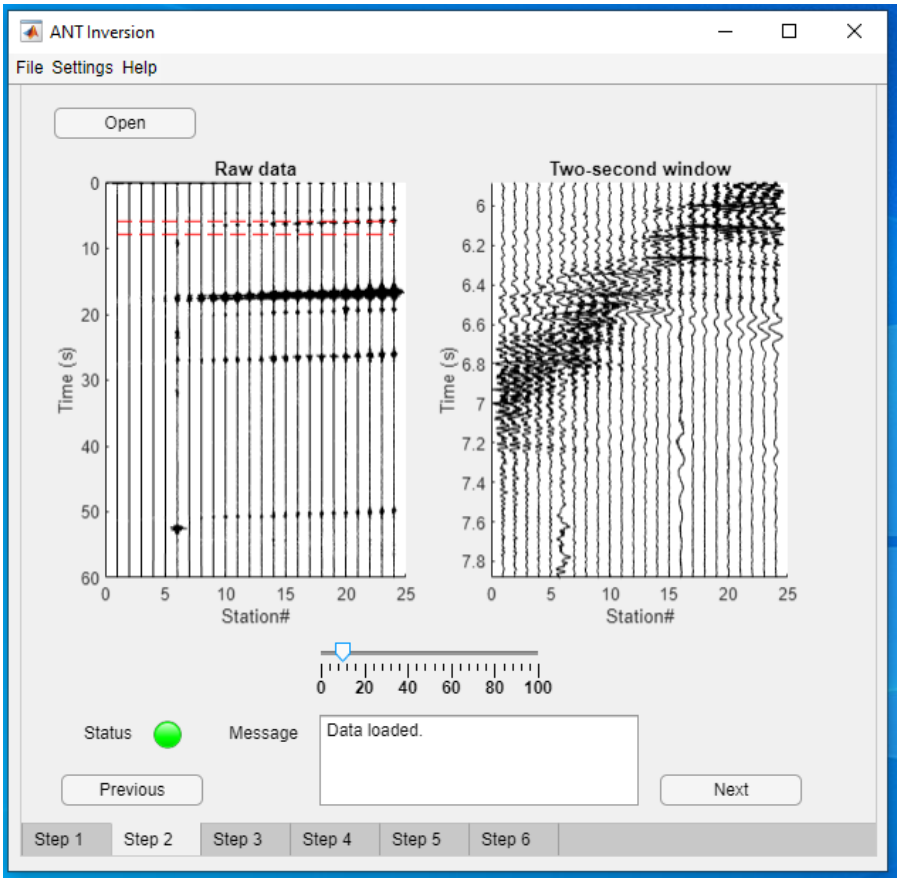

Figure 6. Display of loaded data

5. Cross Correlation

Step 3 of the ANT analysis is to compute the cross-correlation of the imported data. This needs to be done carefully. Choose either:

1. Settings > Cross Correlation
2. Click the “Next” button in the “Step 2” tab

to open the corresponding window as seen in Figure 7.

Figure 7. Cross correlation page

The following values are required:

- Time seg (sec) and Time max (sec) are the segment length and the max time for computing the cross-correlation function (CCF), respectively.

- Vs max is the estimated maximum Vs value used for CCF computing to avoid correlating signals from multiple wave sources (source-correlation issue). The default value of 500 m/s works for most cases.
- Filtering frequencies: f1, f2, f3, and f4 (Hz) as shown in Figure 8.

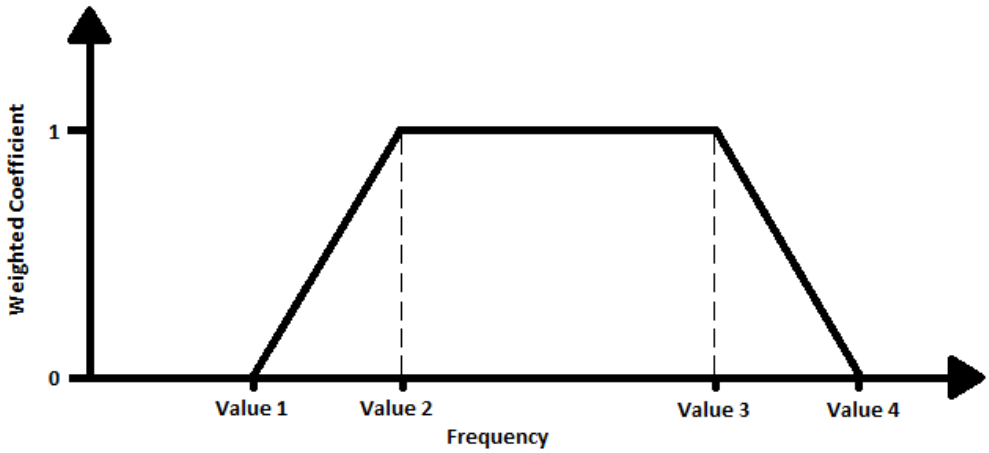

Figure 8. Filtering bandwidth

You do the following steps:

1. Enter values for all the inputs: Time seg, Time max, and filters (f1, f2, f3, and f4).
2. Flip a segment of the cross-correlation function (channels in reverse order), using the box “Flip CCF”. You can skip this step if the channels are in correct order.
3. Select “Calculate CCF” to compute the cross-correlation function. This may take several seconds to several minutes, depending on the computer specs and size of imported data. The status lamp will display yellow while calculating and turn green when completed (Figure 9).
4. Click on “Gain Balance” to inspect to CCF (Figure 10, left).
5. Click on “Spectrum” button to check the frequency spectrum (Figure 10, right).

6. Remove bad traces in the calculated CCF by click on “Kill Trace” button (Figure 11). After removing, click on “Kill Trace” button again to exit the kill-trace mode. The original CCF can be restored by clicking the “Restore plot” button.

7. Select “Save” to save the conditioned CCF as shown Figure 11.

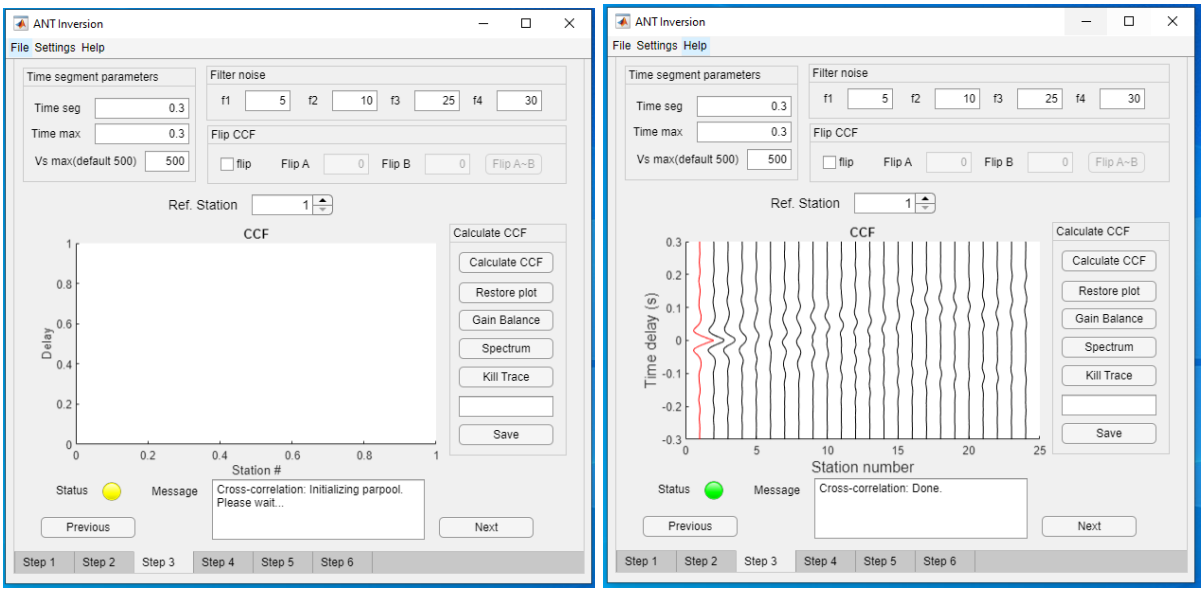

Figure 9. Calculating the cross-correlation

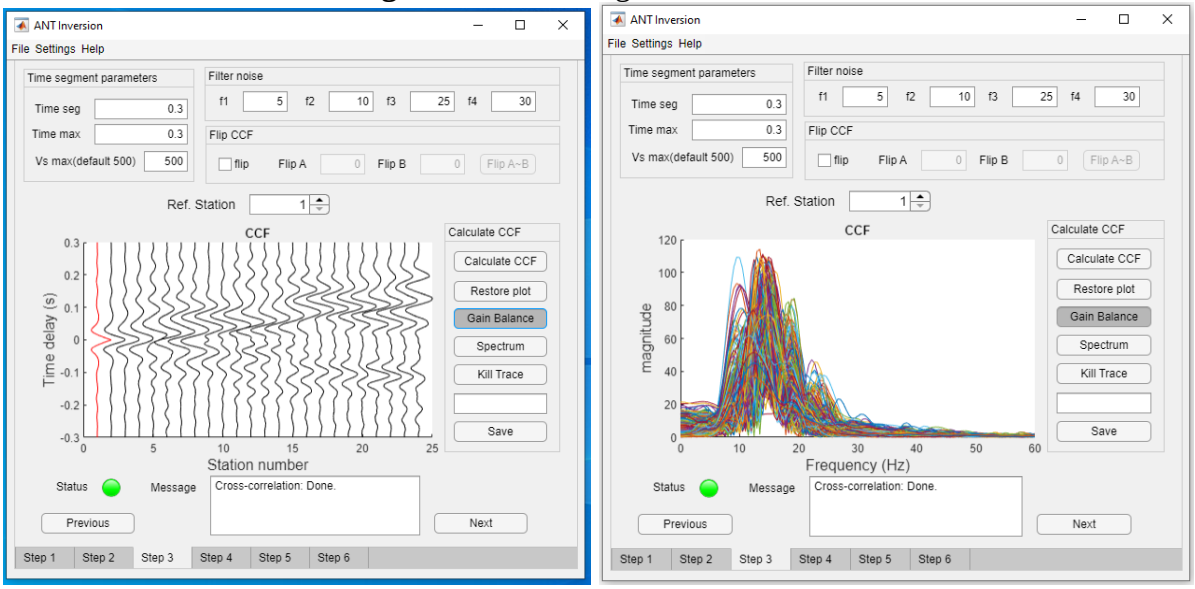

Figure 10. Apply gain balance (left) and check the spectrum (right)

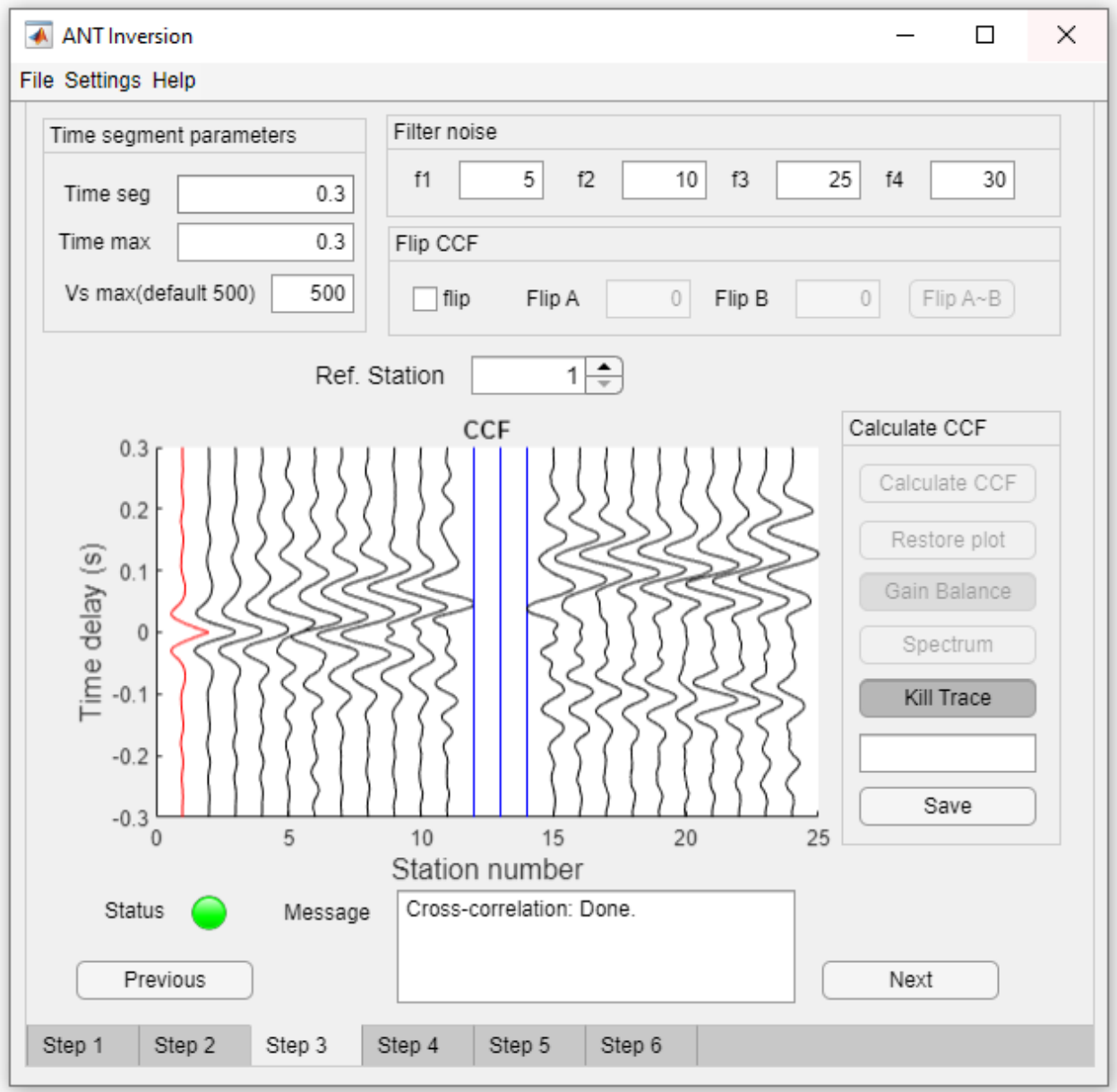

Figure 11. The "Kill Trace" mode and save CCF

6. Spectral Analysis

Step 4 of the ANT analysis is to do the spectral analysis. It is optional and can be skipped if the initial model is already known (e.g., reprocessing). This step is to determine the range of S-wave velocity used in the initial model. To do this, choose either:

1. Settings > Spec Analys
2. Click the "Next" button in the "Step 3" tab

This action will bring up a tab as shown in Figure 12 (left) and contains a “Dispersion image” blank plot and a “Analyze” button. To do this analysis, follow below steps:

1) Enter values for “Velocity max” and “Frequency max” parameters (for analyzing and plotting), where “Velocity max” and “Frequency max” are the maximum velocity and frequency, respectively.
2) Click “Analyze” to generate the dispersion curve and the status bar changes to “Running Spectral Analysis”. The status lamp will display yellow, and the gauge will show the calculation progress (Figure 12, right).

An example of the generated spectral image is shown in Figure 13. The S-wave velocity range of 275 m/s to 500 m/s (at 20 to 5 Hz) is used for the initial model in the next step.

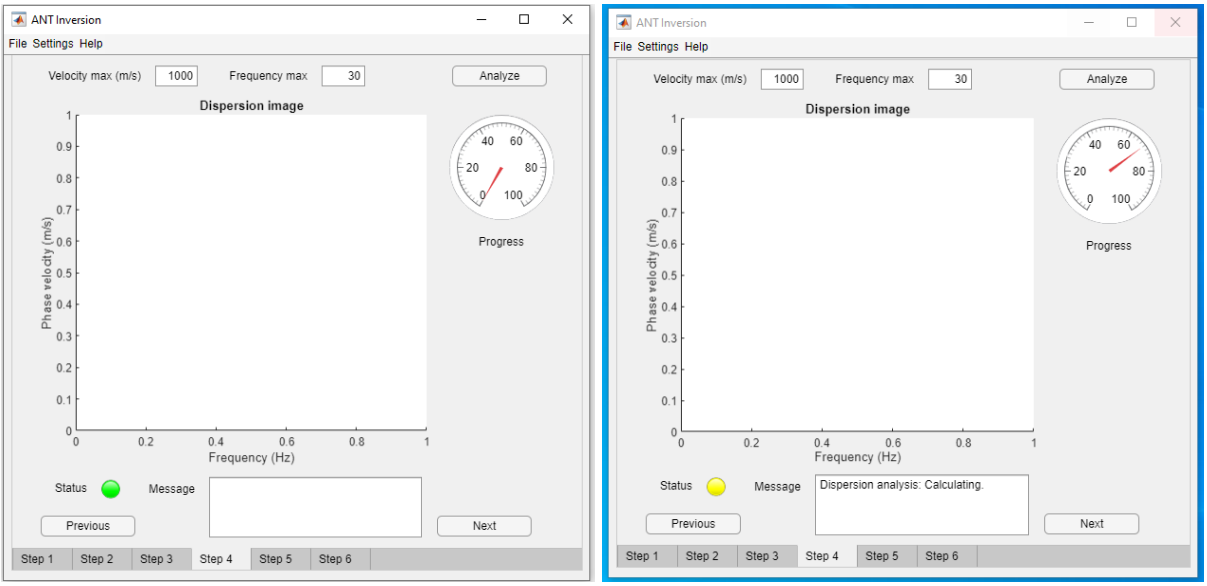

Figure 12. Calculating the dispersion image.

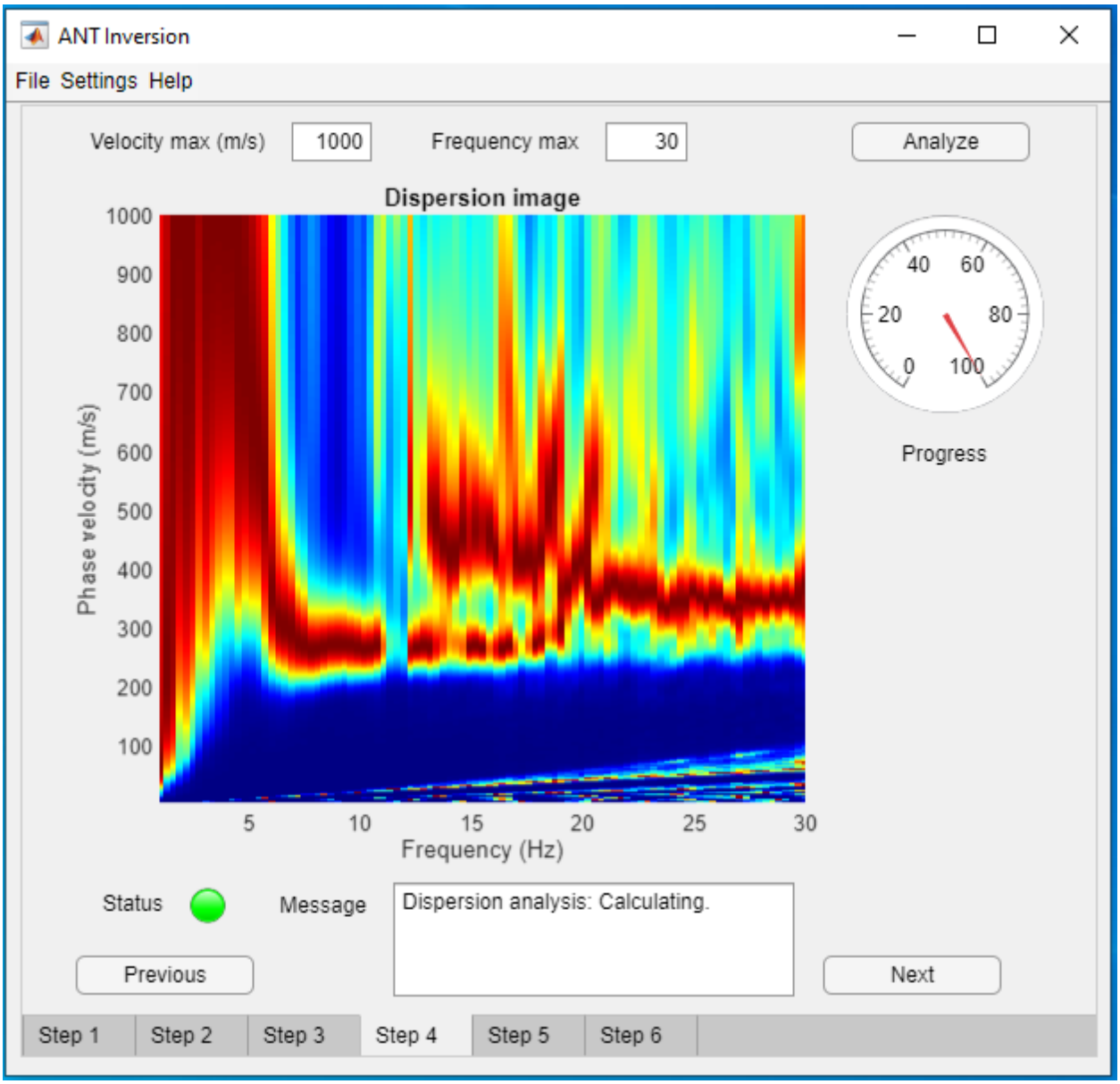

Figure 13. Calculated dispersion image.

7. Initial model

Step 5 of the ANT analysis is to generate the initial model. To do this, choose either:

1. Settings > Initial Model
2. Click the “Next” button in the “Step 4” tab

Then:

a) Input S-wave velocity at the surface (Vs top) and the bottom (Vs btm). Vs at the bottom must be larger or equal Vs top.

b) Click “Generate” button to generate the initial model (Figure 14).

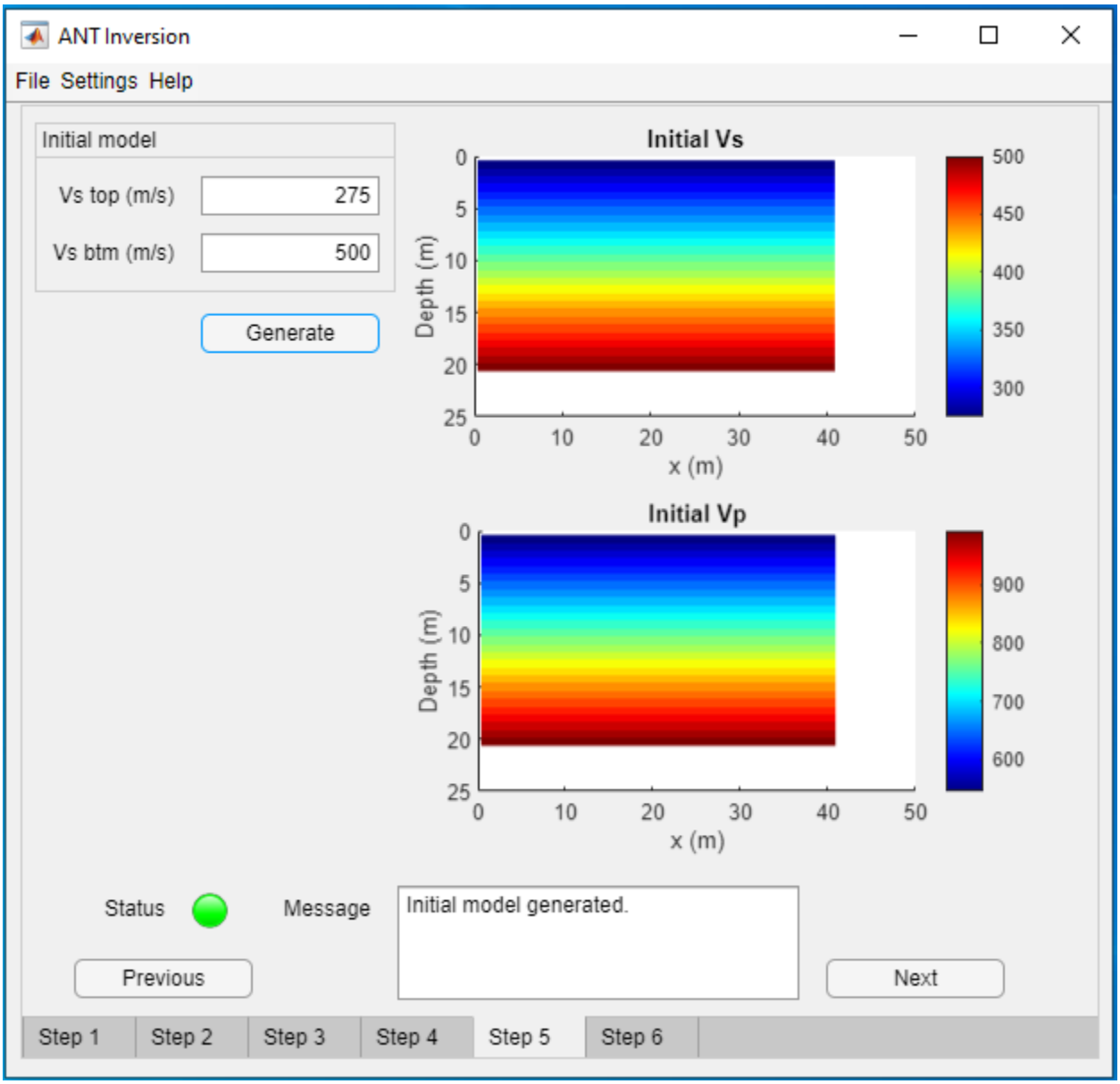

Figure 14. Initial model for S- and P-wave velocities.

8. Inversion

The final step (Step 6) of the ANT analysis is to invert data for Vs profiles. The inversion process combines all previous aspects of the user interface including the parameters, imported data, and initial model. Vs model is updated iteratively by matching the synthetic data with the field data, and the final Vs model is created when the inversion is complete.

To do this step, choose either:

1. Settings > Inversion
2. Click the “Next” button in the “Step 5” tab

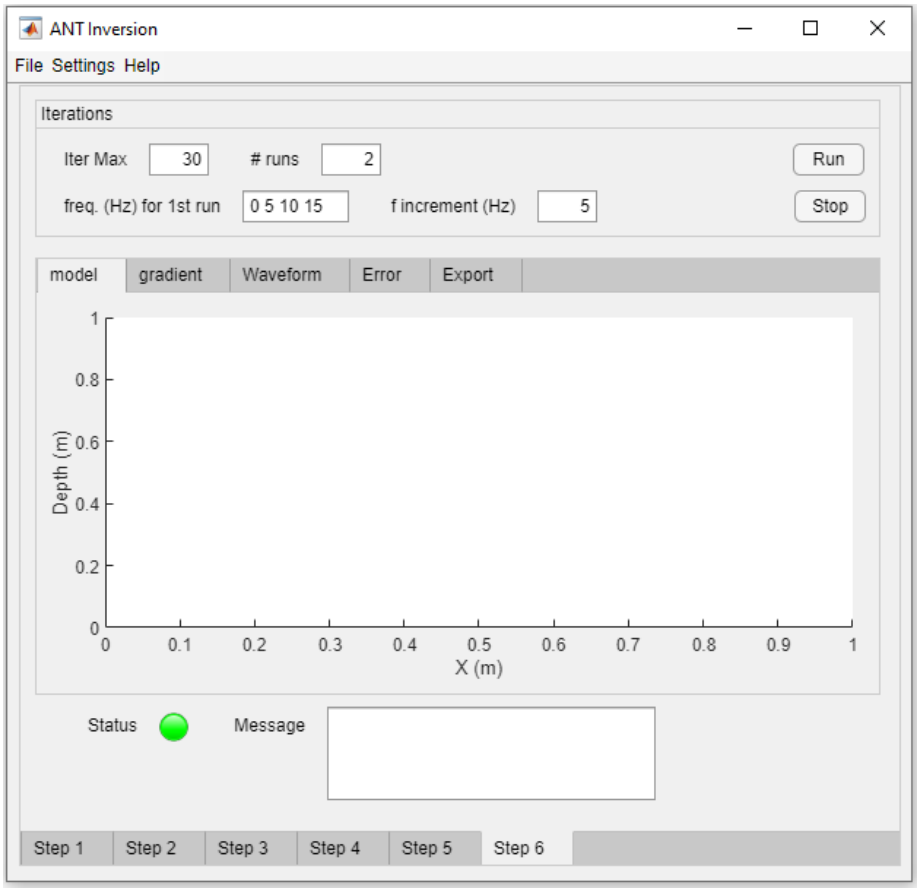

Figure 15. Inversion page

As shown in Figure 15, you do the follows:

1) In the “Iterations” box: Enter the maximum number of iterations (Iter max) and the number of runs. The total number of iterations will be divided evenly into the number of runs. For example, if the user enters “30” for “Iter Max” and “2” for “# runs”, then inversion includes two runs, and each run has 15 iterations.
2) In the “Filter” box: Enter four values of filtering frequencies (see step 3: Cross-Correlation for explanation of the frequencies). You can insert the desired values in the editable box (using space between the numbers) or use the forward and backward buttons, which allow to change the frequency values. These values must be in ascending order from the left to right. Shown in the example (Figure 15), the filtering frequencies are 0, 5, 10, and 15 Hz for the first run. With a frequency increment of 5 Hz, the filtering frequencies of the second run will be increased by 5 Hz. Namely, they become 5, 10, 15, and 20 Hz, respectively.
3) To do the inversion analysis, click “Run”.

   Inverted Vs, gradient, waveform comparison, and error value for each iteration will be displayed during inversion and at the end (Figure 16). Inverted Vs are saved for all individual iterations. You can also check the waveform comparison of CCF and least-squares error (Figure 17).

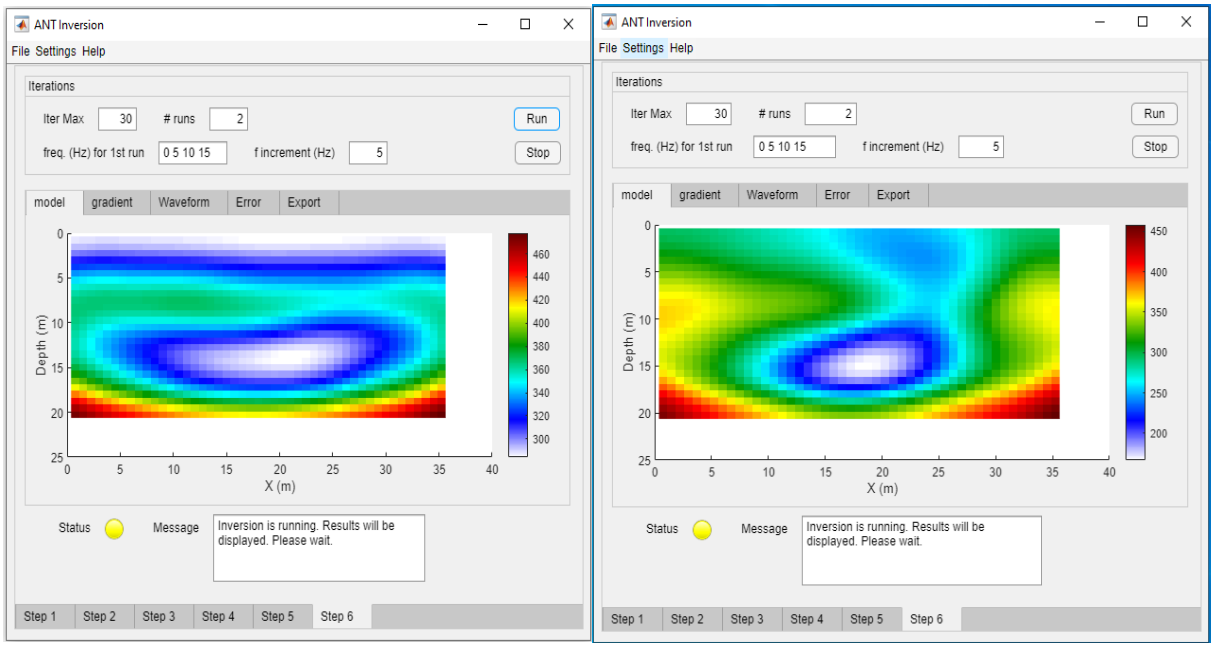

Figure 16. Inverted S-wave velocity during inversion (left) and at the end (right)

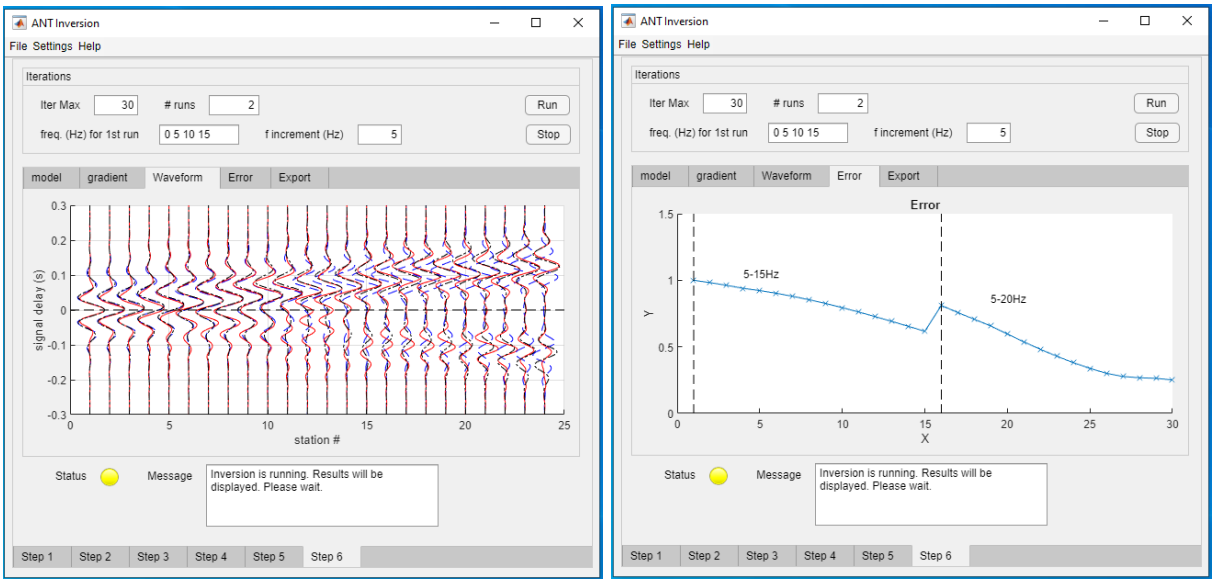

Figure 17. Waveform comparison (left) and least-squares error (right)

When the inversion is finished, you can export the inverted Vs profiles to pictures, PDF, or Excel files. To do this, go to the “Export” in “Step 6” and click on “Refresh” button. This action will bring up Figure 18. Select the file to export in the list, and then click “Export” to save the selected result.

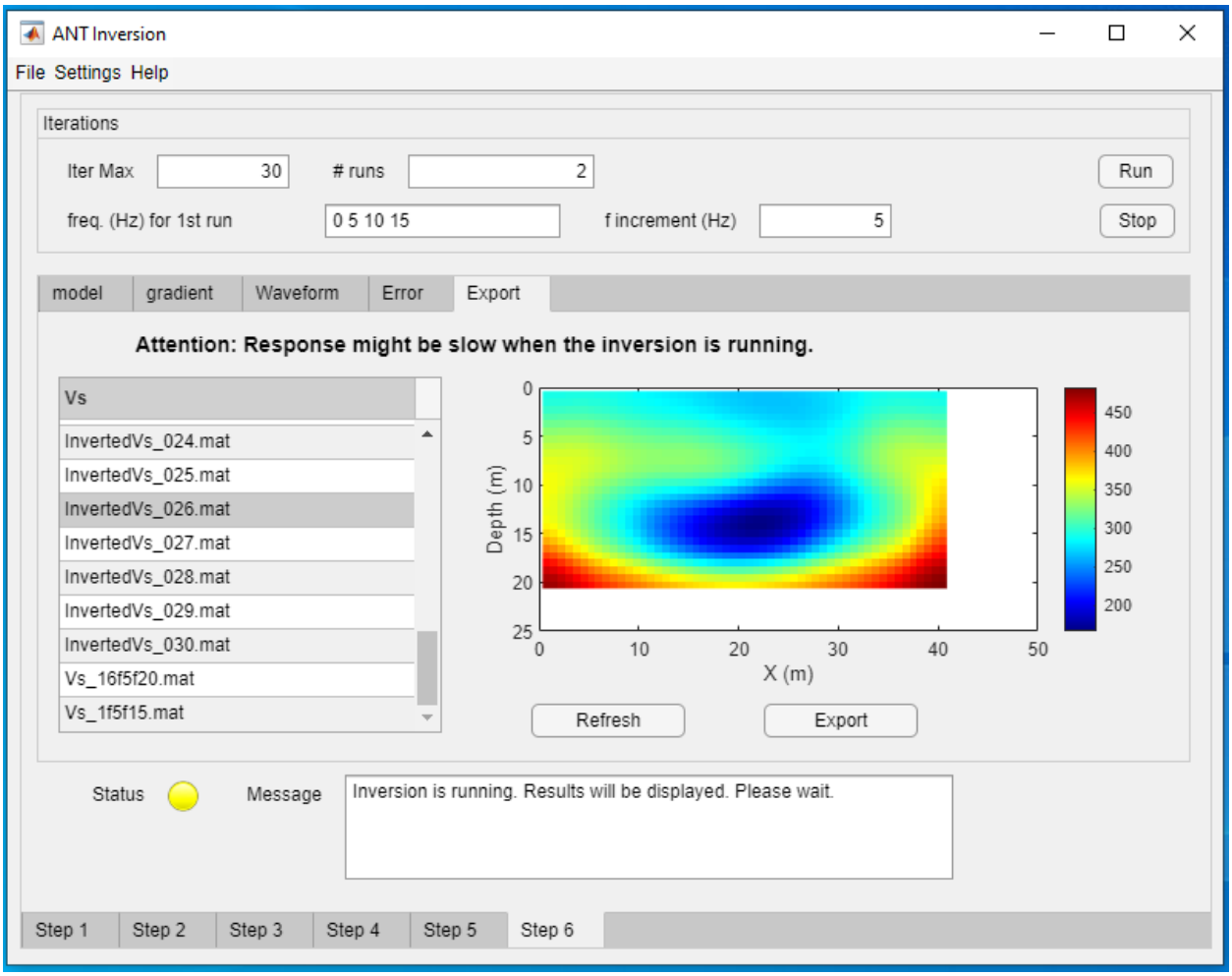

Figure 18. Export the inverted S-wave velocity.

9. Save and Open Inversion Projects

a) Save

The entered parameters, calculated CCF, and the initial model can be saved as an ambient noise inversion project file (.ant). Before saving the working space as a project, you must input a set of

valid parameters (Step 1), calculate the CCF of imported noise data (Step 2 and 3), and define the initial model (Step 4). After these actions, you can choose

File > Save, or File > Save as

to save the current working space. Choosing "Save" will bring up Figure 19. In this way, the project file name will be automatically generated in the format "yyyy-mm-dd_hh-mm-ss.ant" (Figure 20). Choosing "Save as" will bring up Figure 21. In this way, you can input the name of project file in the pop-up window. For example, entering a filename, "NEW_ANT_PROJECT.ant", and then click the "Save" button to save the current workspace to a file with this filename (Figure 22).

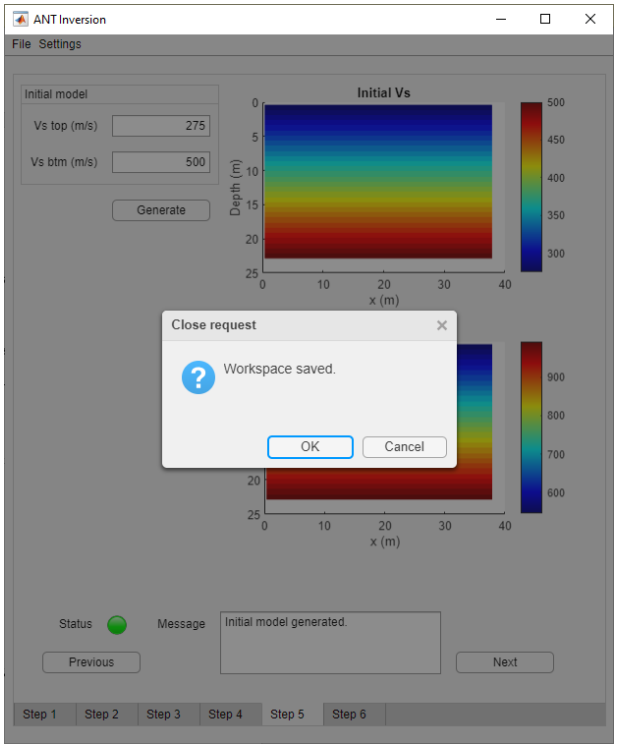

Figure 19. Save the workspace via "Save" menu

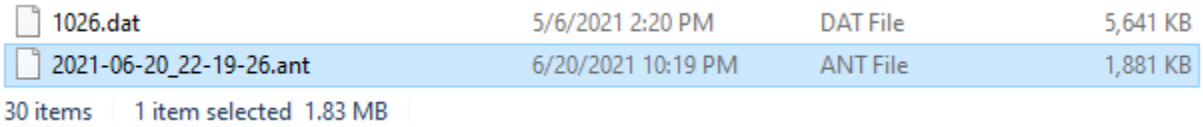

Figure 20. The project file automatically generated by pressing the "Save" menu.

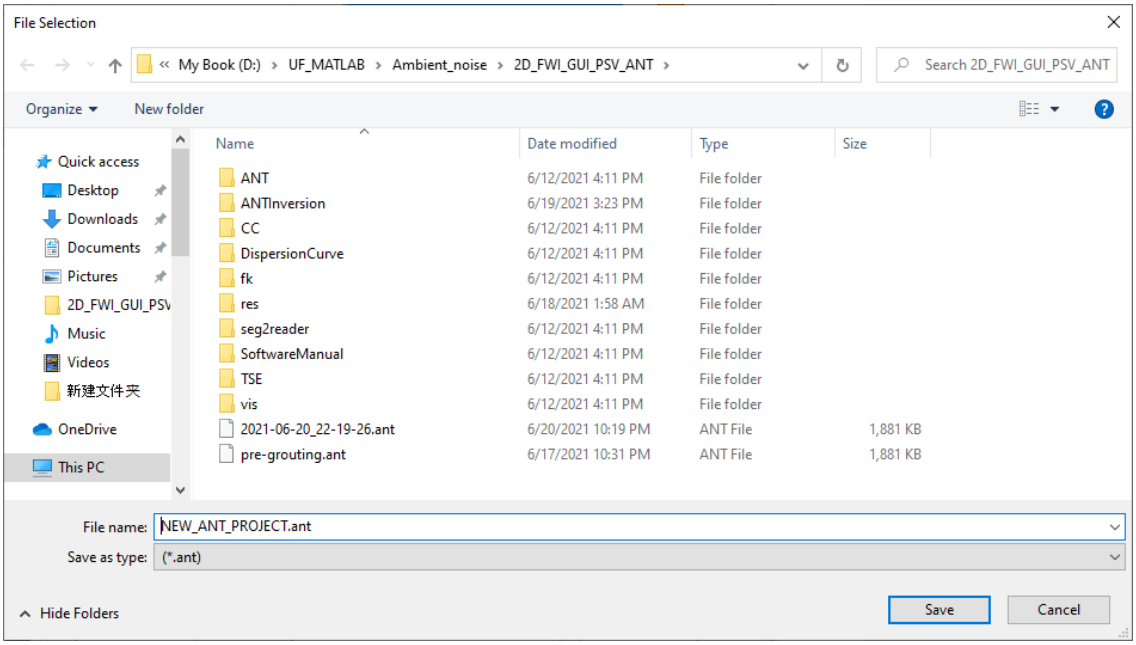

Figure 21. Save the workspace via "Save as"

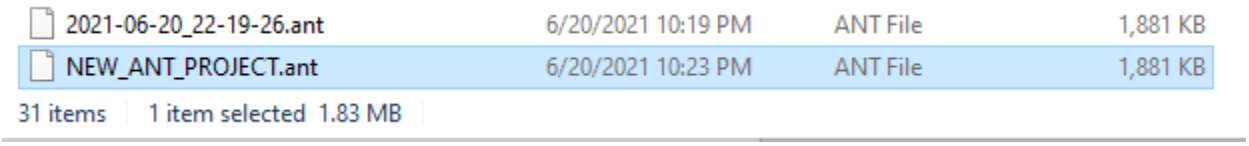

Figure 22. The project file generated by "Save as"

b) Open

To open a saved project file, press the "Open" menu. This action will bring up a new window (Figure 23). You can select the project file in this pop-up window to load a saved workspace. For example, you can open the saved "NEW_ANT_PROJECT.ant" project to bring up Figure 24. This saved project already has everything ready for inversion, therefore the GUI will lead to the step of "Inversion" (Step 6). You can change parameters (frequencies, number of iterations, number of runs), and click on "Run" button to re-run the analysis. If using another dataset or doing additional processes in the opened project, you must perform Steps 2 and 3 to import data, calculate the CCF, and process the CCF.

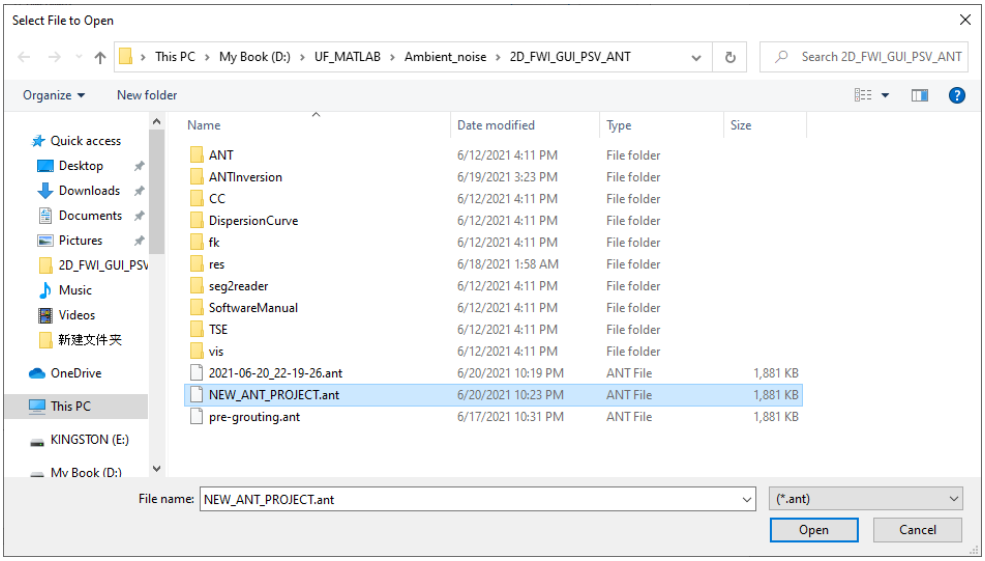

Figure 23. Open a saved project

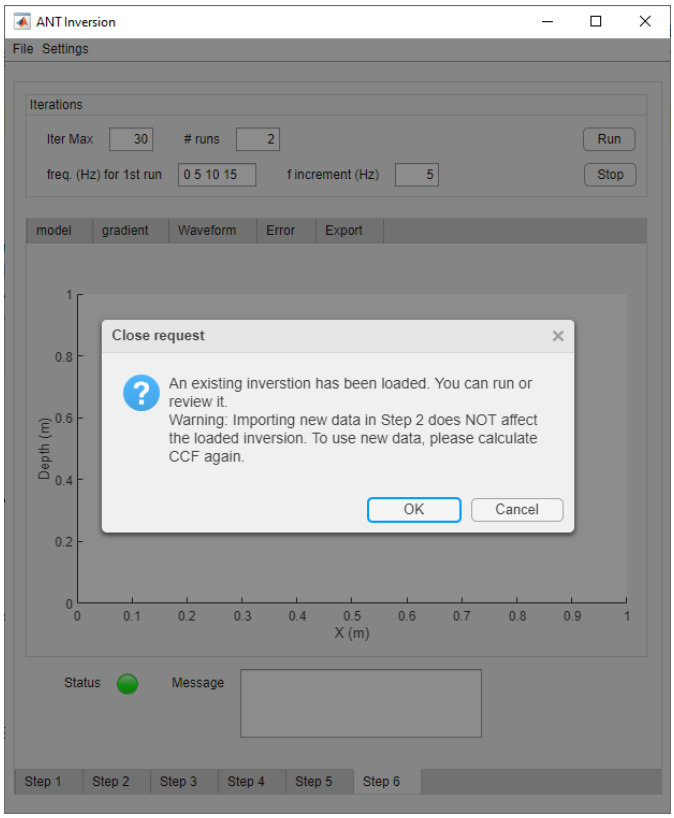

Figure 24. A project file is opened.

10. Help

The help menu is created to access the software manual as seen in Figure 25. You can click on "Help" to bring up the manual.

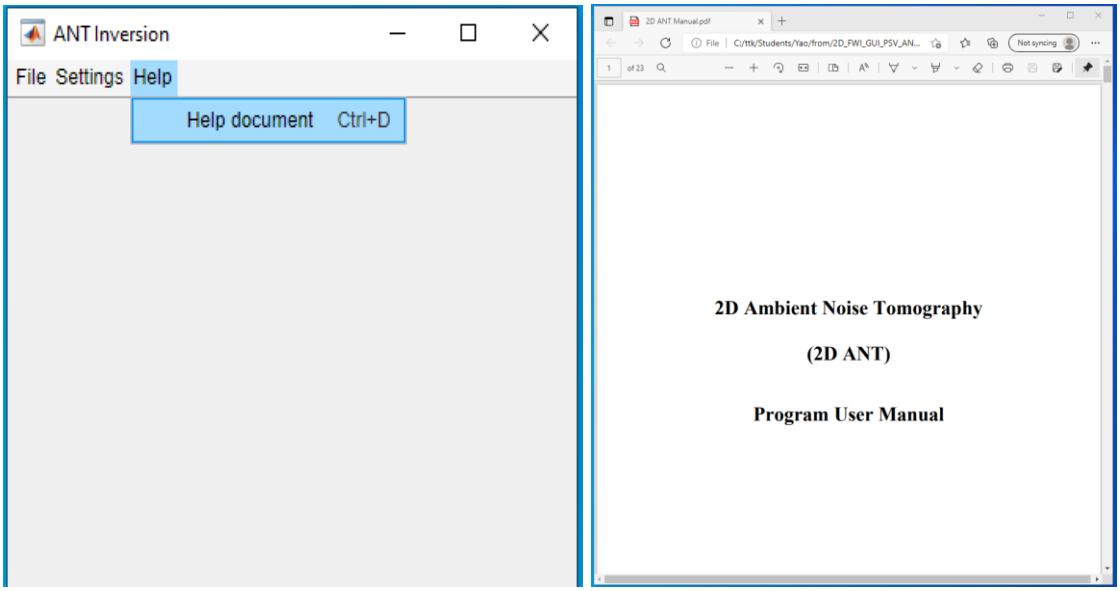

Figure 25. Help menu to access to the software manual